Near-infrared photodetection in nanocarbon materials

TECHNISCHE
UNIVERSITÄT
DARMSTADT

Vom Fachbereich Material und Geowissenschaften
der Technischen Universität Darmstadt
zur Erlangung des akademischen Grades
DOKTOR DER NATURWISSENSCHAFTEN

genehmigte DISSERTATION

von
Naga Anirudh Peyyety
aus India

Referrant:	Prof. Dr. Ralph Krupke
Koreferrant:	Prof. Dr. Robert Stark
Prüfer:	Prof. Dr. Jörg Schneider
Prüfer:	Prof. Dr. Jan Philipp Hofmann

Tag der Einreichung: 22.09.2022
Tag der muendlichen Pruefung: 16.11.2022

Darmstadt, November 2022

Peyyety, Naga Anirudh : Near-infrared photodetection in nanocarbon materials
Darmstadt, Technische Universität Darmstadt
Year thesis published in Tuprints 2023
Date of viva voce 16.11.2022

Published under CC BY-SA 4.0 International
https://creativecommons.org/licenses/

DECLARATION

I, hereby declare that, this thesis is an outcome of my work. Contents from collaborations are acknowledged. I certify that this thesis has not been submitted elsewhere. Additionally, care has been taken to ensure that the work is original and material included in the thesis previously published is cited congruously.

Date

Signature

Table of Contents

ABSTRACT--- 1

CHAPTER 1 INTRODUCTION-- 3

CHAPTER 2 OPTOELECTRONIC PROPERTIES OF NANOCARBON MATERIALS -------------------------- 9

2.1 Graphene--- 9

2.2 Graphite --11

2.3 Nanocrystalline graphite (NCG)--13

2.4 Carbon nanotubes ---15

2.5 Raman fingerprint of nanocarbon materials ---19

2.6 Synthesis methods for nanocrystalline graphite --24

2.7 Photoresponse of nanocarbon materials ---26

2.8 Plasmonic nanostructures ---41

CHAPTER 3 EXPERIMENTAL TECHNIQUES---43

3.1 NCG synthesis method--43

3.2 Atomic force microscopy--44

3.3 Scanning electron microscopy --44

3.4 Raman spectroscopy ---44

3.5 Device fabrication--45

3.6 Electrical characterization--46

3.7 Simulations --46

3.8 Photocurrent setup description-- 48

CHAPTER 4 NIR PHOTODETECTION WITH NANOCRYSTALLINE GRAPHITE ---------------------------- 63

4.1 NCG thickness optimization and transfer matrix simulation --------------------------------------- 67

4.2 Synthesis of thickness optimized NCG films -- 68

4.3 Raman spectroscopy of NCG films -- 69

4.4 Device fabrication and electrical characterization -- 71

4.5 Scanning photocurrent spectroscopy -- 74

4.6 Discussion -- 81

4.7 Conclusion-- 83

CHAPTER 5 NIR PHOTODETECTION WITH CARBON NANOTUBE FILMS-------------------------------- 85

5.1 Raman spectroscopy of carbon nanotube films and device fabrication -------------------------- 86

5.2 Electrical characterization-- 90

5.3 Scanning photocurrent measurements -- 91

5.4 Measurements under a source-drain bias-- 97

5.5 Measurements under a gate voltage in short-circuit condition------------------------------------- 98

5.6 Photogating in Silicon substrates --103

CHAPTER 6 PLAMONIC-PHOTONIC (PPHC) STRUCTURES FOR LIGHT-MATTER ENHANCEMENT IN NANOCARBON MATERIALS---107

6.1 Fabrication and design overview of PPhC structures ---108

6.2 Description of PPhC resonances ---110

6.3 Raman measurements --111

6.4 Simulations of PPhC --- 116

CHAPTER 7 SUMMARY --- 121

BIBLIOGRAPHY --- 125

APPENDIX --- 135

LIST OF FIGURES --- 151

LIST OF TABLES --- 159

ACKNOWLEDGEMENTS --- 163

LIST OF PUBLICATIONS --- 165

Abstract

The conversion of light into electricity is at the heart of solar cells and photodetectors and in other optoelectronic devices used in telecommunication systems. In particular, near-infrared (NIR) photodetection is very relevant for applications in night vision, remote sensing, food inspection, and surveillance. Novel materials that enable broadband NIR photodetection are sought, and the emerging class of nanocarbon and other 2D materials hold promise for large device photoresponsivities, high-speed detection, spectral control of the photoresponse, ease of integration, and waferscale fabrication.

In this thesis, two types of nanocarbon materials have been explored for broadband NIR photodetection: nanocrystalline graphene (NCG) and single-walled carbon nanotubes (SWCNTs) networks. Graphene is a gapless 2D semi-metal with wavelength-independent light absorption with only 2.3% of the incident photons in a wide wavelength range. The growth of multi-layer graphene with predefined thickness for increased absorption has not yet been realized. To this end, nanocrystalline graphite (NCG), synthesized with a defined thickness on a silicon wafer, is introduced as a material for near-infrared to short-wavelength infrared (SWIR) photodetection. A broadband spectrally flat photoresponse was obtained in the NIR-SWIR spectral region, and the detected photocurrents were attributed to a temperature-induced bolometric effect.

The SWCNT networks with a diameter distribution tailored for the near-infrared photodetection are grown using chemical vapor deposition (CVD) process on SiO_2/p-Si substrates. The SWCNT networks are complementarily characterized using multi-wavelength resonant Raman spectroscopy and scanning photocurrent spectroscopy. The photocurrent data confirms a broadband optical response to the near-infrared light indicating a large diameter distribution in the CNT network. Devices are fabricated in a transistor geometry to study the spatial photoresponse distribution under different biasing schemes in the 1100 nm – 1800 nm spectral region, and the resulting photoresponse is discussed in terms of the photodetection mechanisms. During the course of this thesis, the photocurrent data were obtained with an in-house developed aberration-corrected scanning photocurrent setup. In order to enhance light-matter interaction in nanocarbon materials, the so-called plasmonic-photonic (PPhC) structures with optical resonances in visible-nIR spectrum were fabricated and characterized to investigate Raman enhancement in graphene. The local enhancements in the PPhCs were understood from the complementary near-field and far-field simulations optical simulations.

Chapter 1 Introduction

At the American Physical Society annual conference in 1959, Richard P. Feynmann delivered his lecture entitled *There is plenty of room at the bottom* where he hypothesized the possibility of controlling and manipulating matter at the atomic or molecular scale.[1] The idea of designing materials at the nanoscale has since inspired great interest in the scientific community leading to the development of transformative technological applications over the following decades, including solar cells, electronic chips, high-speed detectors, and diagnostic biosensing. In this context, carbon-based nanomaterials or so-called nanocarbon materials have attracted attention in almost every conceivable branch of science and engineering. Of main interest here are their optical and electrical properties, which through a rational design, has shown promise for the next generation of electronic and photonic circuitry.[2–4] However, some fundamental constraints like low light absorption (e.g., in single-layer graphene) and control of the electronic purity and alignment (e.g., in carbon nanotubes) limit their full potential for optoelectronic applications.

Nanocarbon materials

The nanoscale allotropes of carbon such as fullerenes, nanotubes, graphene, and nanocrystalline graphite are part of the nanocarbon family. In addition to the bulk-scale carbon allotropes like diamond and graphite, the nanocarbons have immensely changed the carbon materials landscape in the past two decades and now find applicability in many disciplines from biology to physics.

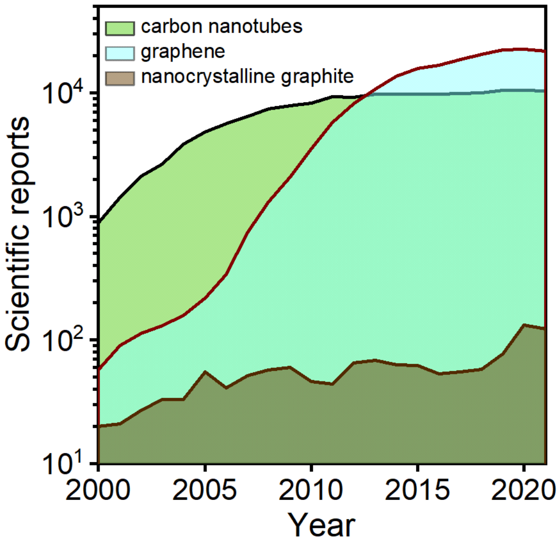

Figure 1.1: Scientific publications from the year 2000 of different nanocarbon materials. The information was obtained by a keyword search using SCOPUS citation database.

The utility of the nanocarbon materials lies in their unique structure-dependent properties, and extensive research efforts have been made since the isolation of a single layer of graphene from graphite in 2004.[5] **Figure 1.1** shows the published scientific reports since 2000 for the three nanocarbon materials discussed in this thesis. The different dimensionalities including the three-dimensional (3D) fullerenes and one-dimensional (1D) carbon nanotubes in the nanocarbon family can be described by their "parent" two-dimensional (2D) structure of graphene. From a structural point of view, graphene forms the basis for understanding the properties of nanocarbon materials. Interestingly, however, graphene has been discovered only in the early 2000s after the discovery of fullerene C_{60} by Kroto et al. in 1985,[6] and single- and multi-walled nanotubes in early nineties by Sumio Iijima.[7] The carbon atoms in graphene have sp^2 hybridization, where each carbon atom forms strong covalent bonds with the neighboring three other atoms to form a planar structure. The in-plane covalent bonds in graphene and carbon nanotubes give rise to the large tensile strength and high thermal conductivity.[8,9] On the other hand, the delocalized electrons in the weak pi bonds between the neighboring carbon atoms give rise to the large carrier mobility and unique electrical transport properties.[10]

Nanocarbon materials for optoelectronics

The prospects of nanocarbon materials for optoelectronic applications have become very evident in the recent years. The devices based on graphene and carbon nanotubes for optoelectronics have been demonstrated in the past, including quantum light emitters, photodetectors, transistors and optical modulators.[11–14] Light emission and detection using CNTs and graphene, in particular have gained prominence as exemplified by the number of review publications.[15–18] The active research on these topics is guided by the performance advantages that include wide-band wavelength tunability, high speed of operation, and large-scale device integration.

Graphene has no bandgap and can be used for broadband photodetection. However, the optical absorption of single-layer graphene is only 2.3 %, therefore, the corresponding photoresponsivity is also weak.[19] The integration of graphene with plasmonic or photonic structures has been shown to result in enhanced light absorption.[20–22] However, the absorption is modified only in a narrow spectral region and is dependent on the geometry and the optical properties of the plasmonic or photonic structure. Therefore, a wavelength-dependency in the absorption spectrum of graphene is inevitably introduced, which ideally is suitable for narrowband applications. Alternatively, a spectrally flat response could be tailored by having a predetermined number of graphene layers (graphite). However, despite the maturity in the waferscale growth of graphene by the chemical vapor deposition (CVD) process, the controlled growth of graphene layers remains elusive.

On the other hand, nanocrystalline graphite (NCG) can instead be grown with a predefined thickness directly on dielectric substrates and involves no post-synthesis transfer processes. Therefore, NCG could be substituted for multilayer graphene for photodetection applications to maximize light absorption. The light absorption in NCG in a targeted spectral region could be maximized by choosing the appropriate layer thicknesses of the substrate. In Chapter 4, the optimum layer thicknesses of the substrate and NCG required to maximize absorption in near- to the short-wavelength infrared spectral region were computed using transfer matrix simulations. The photodetection mechanism in the devices fabricated from the thickness-optimized NCG was understood from the electronic system driving the photocurrents under different voltage biasing conditions.

The semiconducting-type single-walled carbon nanotubes (sc-SWCNTs) have a direct bandgap and can be employed for both narrowband and broadband photodetection from visible to near-infrared spectral regions. The optical transition energies in SWCNTs have approximately an inverse relationship with the nanotube diameter.[23] The absorption spectrum of sc-SWCNTs consists of the characteristic narrow excitonic transitions, with the exciton binding energies on the order of several hundred meV.[24] On the other hand, the absorption spectrum of conventional semiconductors consists of absorption band edges. The SWCNTs, therefore, can selectively absorb light from the visible to the near-infrared depending on their diameter. Since the SWCNTs are quasi-1D materials, the interaction with the incident light is polarization-dependent, with the maximum light absorption in the direction parallel to the axis of the CNT.[25] Further, when integrated as a channel material for an optoelectronic device, the same CNT device can be operated as a light emitter, a light detector, and a transistor by modifying the applied bias and gate voltage.[12] The light-matter interaction in individual CNTs depends on their absolute absorption or absorption cross-section and is extremely low for single-tube devices, making them inefficient photodetectors for practical applications.[26] Therefore, devices with nanotube thin films or networks become important and should be explored from an application standpoint. The electrical transport, however, in single-tube devices and random networks can be very different due to the domination of the tube-tube junctions in the latter. In the former, the electrical transport is dominated by ballistic transport for channel lengths shorter than the carrier mean free path. In Chapter 5, the near-infrared photodetection in SWCNT networks that are grown directly on the silicon substrates is described.

The general goal of the thesis is to study the near-infrared photodetection in nanocarbon materials, specifically NCG and large-diameter distribution (1 nm - 2 nm) SWCNT networks. The near-infrared spatial photocurrent distribution in the device was investigated using scanning photocurrent spectroscopy, and the generated photocurrents are discussed in terms of the dominant photodetection mechanisms. The mechanisms responsible for the photocurrent generation originate either in the excess heat or the excess carriers generated due to the light absorption in the photoactive area of the device. The scanning photocurrent setup was redesigned and compensated for chromatic aberration for acquiring diffraction-limited spatial photocurrent maps in the near-infrared to short-wavelength infrared spectral region (setup description in Chapter 3).

The plasmonic or photonic structures, referenced earlier, give rise to the local field enhancements. In this thesis, in Chapter 6, so-called plasmonic-photonic (PPhC) structures are described which have optical resonances resulting in field enhancements in visible and near-infrared spectral region. The light-matter interaction in graphene integrated with PPhC structures is probed via., Raman spectroscopy. The enhancements in the Raman signal could be observed when the incoming or the outgoing wavelengths exhibit a spectral matching with the PPhC resonances. By adjusting the structural parameters like air-hole diameter and lattice parameters, the PPhC resonances can be selectively tuned in the visible/near-infrared spectral region.

Thesis overview

This thesis is organized into the following chapters:

- **Chapter 2** gives the overview of the electrical and optical properties of nanocarbon material materials. In the latter half of this chapter, discussion is dedicated to the concepts of photodetection and a review of different photocurrent generation mechanisms in nanocarbon materials.

- **Chapter 3** describes the experimental techniques employed for fabrication and characterization of the nanocarbon devices. In the second half of this chapter, the in-house scanning photocurrent setup is described that includes the setup design, supercontinuum light source calibration and chromatic aberration correction.

- **Chapter 4** describes the near-infrared photodetection in the thickness optimized nanocrystalline graphite (NCG). The thickness optimization in NCG is discussed in the context of simulations. The dominant photodetection mechanisms under the zero bias condition and an applied bias are discussed.

- **Chapter 5** describes the near-infrared photodetection in large-diameter single-walled carbon nanotube networks (LD-SWCNTs). The SWCNT network was characterized using Raman spectroscopy. The wavelength-dependent scanning photocurrent imaging data is discussed for different biasing conditions.

- **Chapter 6** describes the light-matter enhancement in nanocarbon materials using plasmonic-photonic (PPhC) structures. The Raman enhancement studies of the graphene transferred onto the PPhC structure are reported.

- In the summary, the main results from this thesis are highlighted followed by the discussion on outlook and future work on nanocarbon materials for optoelectronic applications.

Chapter 2 Optoelectronic properties of nanocarbon materials

2.1 Graphene

Diamond and graphite are well-known allotropes of carbon. Diamond is a three-dimensional (3D) insulator with an indirect bandgap of 5.5 eV and has optical gap excitations in the ultraviolet spectral range. In contrast, graphite is a quasi two-dimensional (2D) material, a semi-metal with no bandgap. The graphite structure consists of individual layers of carbon atoms with pi and sigma bonding. Carbon has a valency of four, and each carbon atom forms three sigma bonds (sp^2) with the three nearest neighbours and the fourth bond is a pi bond oriented perpendicular to the plane of graphite layers. The motion of the delocalized pi electrons in the carbon lattice gives rise to the graphite's electrical conductivity. The individual layers of graphite or a single layer of carbon atoms are called graphene. A single layer of graphene was isolated in 2004, and since then, there has been an ever-growing interest, especially in its optoelectronic properties.[27] The carbon atoms in graphene have a hexagonal arrangement as shown in **Figure 2.1a**.

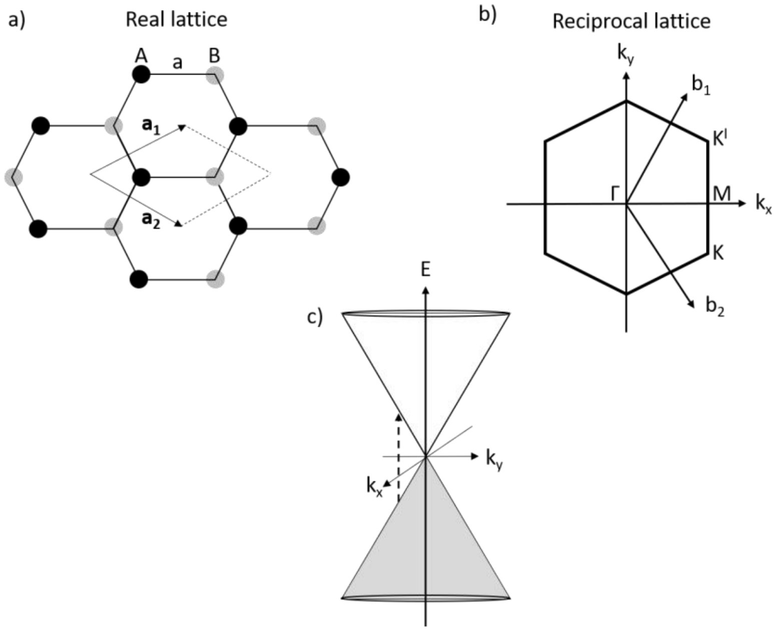

Figure 2.1: (a) Real lattice representation of graphene with the lattice vectors a1 and a2 spanning the unit cell. The atoms from different sublattices are represented in different colors. (b) Reciprocal lattice notation with high symmetry points (Γ, K, and M). (c) Enlarged Brillouin zone near the K-point or the Dirac point. The full band structure is shown in **Figure 2.2**.

The unit cell of graphene consists of two non-equivalent atoms in the real space and is spanned by the lattice vectors $\mathbf{a_1}$ and $\mathbf{a_2}$. The carbon atoms in the hexagonal lattice are separated by an interatomic distance of $a_{c\text{-}c}$ = 0.142 nm.[28] The reciprocal lattice consists of three high symmetry points of the Brillouin zone (Γ, K and M).[29] The Brillouin zone is constructed from the hexagonal reciprocal lattice of graphene, and it is the area enclosed by the bisectors to the line joining the nearest neighbours. The full electronic band structure of graphene is shown in **Figure 2.2.** At the K point, the peak of the valence band (π) intersects with the conduction band dip (π*), resulting in the absence of an energy gap to the states in the conduction band. Further, the bands are linear at the K point. The Fermi level energy is indicated as E_F and represented by a dashed line. The linear bands of graphene at the K point result in many note-worthy properties. For instance, independent of their energy, the conduction electrons have the same velocity (≈ c/300).[30] Due to this relativistic nature of the conduction electrons, the K point is also called the Dirac point (indicated by an arrow in **Figure 2.2**). As the energy gap at the Dirac point is zero, optical transitions are independent of the photon frequency. Further, the absorption in graphene is wavelength-independent at optical frequencies and has a constant value of 2.3 %.[19]

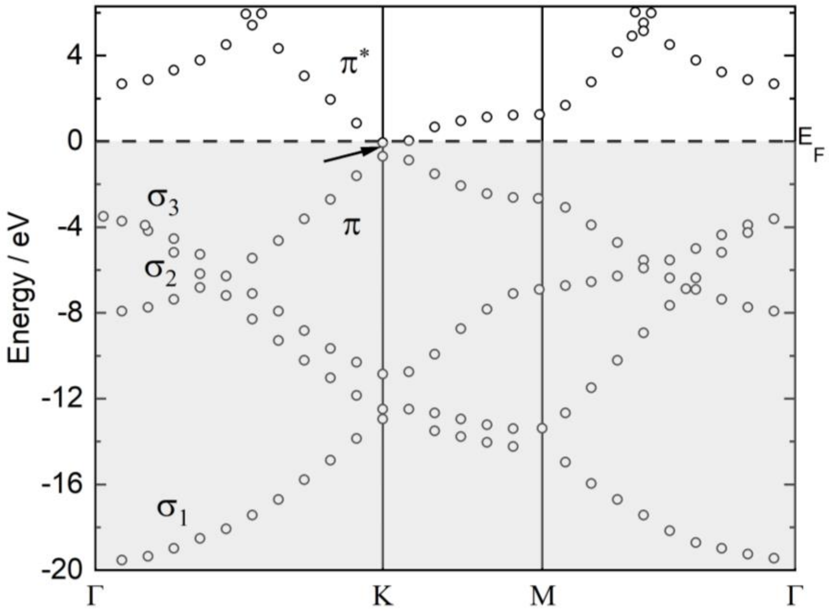

Figure 2.2:Full band structure of graphene. Adapted from [[31]]

2.2 Graphite

The optical transparency of graphene is governed by the fine structure constant α ($\alpha = e^2/\hbar c = 1/137$), that dictates the strength of light coupling with the relativistic electrons in graphene. A single layer graphene absorbs about 2.3% (πα) of incident photons in a wide wavelength range from visible to infrared, and its transmittance was first measured by Nair. et al.[19] (**Figure 2.3a**).

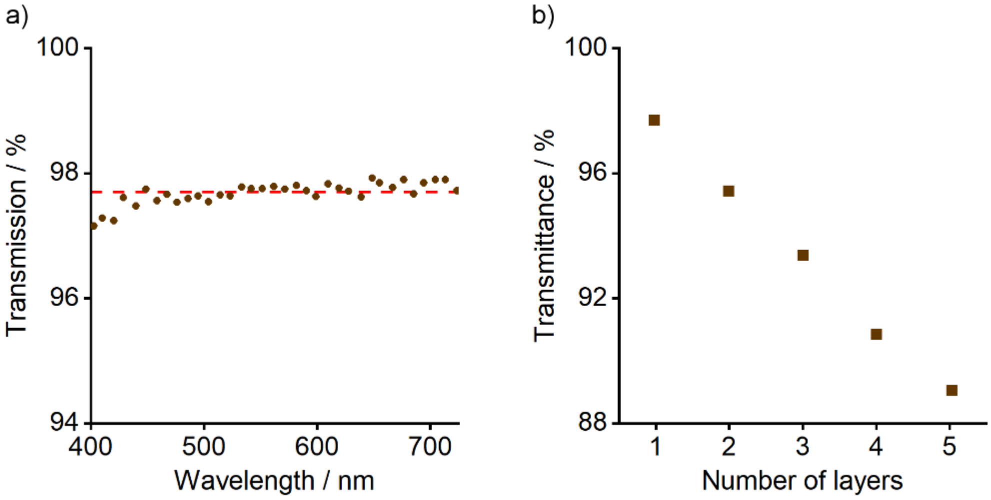

Figure 2.3:(a) Measured transmittance of single layer graphene and the dashed red line represents the expected transmittance for the theoretical absorptance of πα. (b) Transmittance as a function of number of graphene layers. Adapted from reference [19]

It was predicted that the transmittance of multilayer graphene will be then equal to $1 - \pi\alpha N$ where N is the number of graphene layers.[19] The measured transmittance as a function of a few graphene layers is shown in **Figure 2.3b.** Interestingly, however as will see below the simple relation for transmittance will not hold when the reflectance from the graphene layers is no longer negligible, which is the case for large N (N > 20). The increasing reflectivity with the layer number also explains why the natural graphite gleams.

Sasaki et al. recently calculated using the transfer matrix methods the absorptance in graphite as a function of layer number, considering the reflectivity.[32] The transfer matrix methods are described in the **Appendix A1**. **Figure 2.4a** shows the calculated absorptance as a function of layer number (N) at three different wavelengths. The plot in open circles (in orange) corresponds to the absorptance for the simpler model where the reflectivity is neglected. For the values of N up to ~20, the calculated absorptance is identical in both cases (with and without reflectivity), beyond which there is a significant deviation. However, at N ~ 87, the absorptance is independent of the wavelength (lump-like behaviour) and is about 50 %. The identical absorption at different wavelengths corresponds to a universal number of layers in graphite for light absorption. The meaning of the universal layer number can be understood from the **Figure 2.4b**, where the calculated reflectance, absorptance, and transmittance are plotted as a function of layer number for the 1550 nm wavelength. As a function of the layer number, the reflectance (R_N) increases, and simultaneously, the transmission (T_N) decreases. The R_N+T_N takes a minimum value corresponding to the cross-over point where the condition $R_N = T_N$ is satisfied. The cross-over point is precisely given by the universal layer number, N = 2/πα (or 87) where each layer efficiently absorbs the same amount of light independent of the wavelength since there is no decay in the electric field.[32]

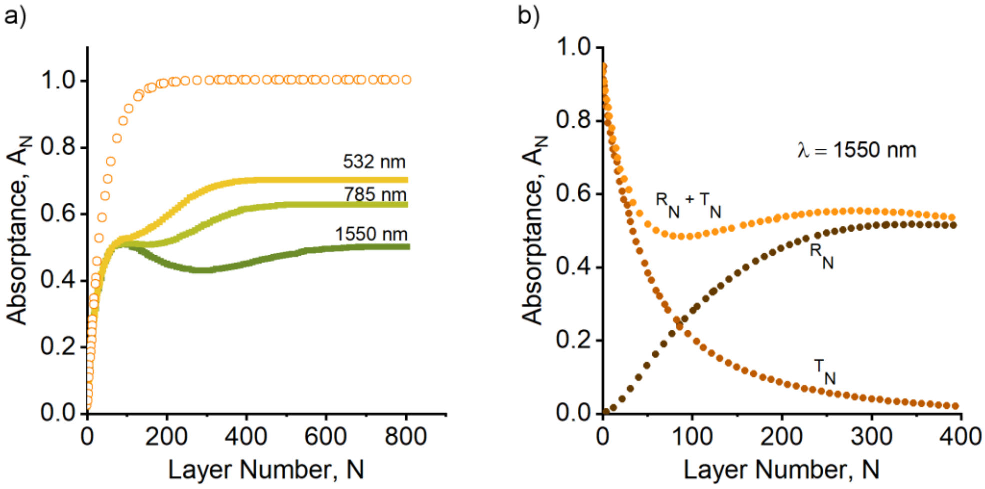

Figure 2.4: (a) Calculated absorptance from the transfer matrix method as a function of layer number at three different wavelengths (532 nm, 785 nm and 1550 nm) and the plot in open circles represents the expected absorptance without taking reflectivity into account. (b) Reflectance R_N and transmittance T_N for 1550 nm as a function of layer number. Adapted from reference [[32]]

The theoretical reflectivity of graphite can be estimated using the relation 2.1 when the dynamical conductivity of graphite is known.[33]

$$(n + i\kappa)^2 = 1 + \frac{i\sigma_{\text{graphite}}}{\epsilon_0 \omega} \qquad (2.1)$$

$$R_{\text{graphite}} = \frac{(n-1)^2 + (\kappa)^2}{(n+1)^2 + (\kappa)^2} \qquad (2.2)$$

Further, the reflectivity of graphite can be reliably reproduced for the condition of very large N using the TMM. This then leads to the analytical expression for the optical constants (n, k) of graphite in terms of the fundamental constant (α), interlayer spacing (d) and, frequency (ω).[32]

$$\sigma_{\text{graphite}} = \frac{\sigma_{\text{graphene}}}{d} \tag{2.3}$$

$$\mathrm{n}(\omega) = \sqrt{\left\{\frac{1 + \sqrt{\left\{1 + \left\{\left(\frac{\pi\alpha c}{\omega d}\right)\right\}^2\right\}}}{2}\right\}}, \kappa(\omega) = \frac{1}{2\mathrm{n}(\omega)}\frac{\pi\alpha c}{\omega d} \tag{2.4}$$

2.3 Nanocrystalline graphite (NCG)

The domain or crystallite size is typically several micrometers in exfoliated graphene or the graphene synthesized by chemical vapor deposition (CVD).[34] Reducing the domain size to the nanometer regime would result in so-called nanocrystalline graphite (NCG).[35] In this thesis in Chapter 4, the near-infrared photoresponse of thickness optimized NCG as an alternative to multilayer graphene is investigated. The various bottom-up chemical routes for synthesizing NCG are presented in Chapter 2, Section 2.8. Due to the ease of waferscale fabrication and low-cost synthesis, NCG was shown to be a suitable candidate to substitute graphene for some optoelectronic applications.[36],[37] A nanometer-thick NCG has similar optical transparency as single-layer graphene. However, the electrical transport characteristics in NCG are significantly different compared to graphene due to nanometer-scale grain-grain boundary effects.[38] The following section discusses the grain size effects on the electrical properties of polycrystalline graphite. The global transport in polycrystalline graphitic sample is dependent on the grain and grain boundary resistance. The overall electrical resistance is the sum of these two contributions.[38]

$$R_{total} = R_{grains} + R_{gb} \tag{2.5}$$

The resistance of the grain-boundary R_{gb} is given by $R_{gb} = \frac{\rho_{gb}}{W}$, where ρ_{gb} is grain boundary resistivity and W is the width of the device or the equivalent length of the grain boundary.[39] The averaged sheet resistance of a polycrystalline sample as function of grain size using the scaling law, $R_s = R_s^0 + \frac{\rho_{gb}}{l_g}$.[40] In the relation, R_s is the sheet resistance of the polycrystalline sample with the contribution from grain and grain boundaries. R_s^0 is the sheet resistance in the grain interior, and l_g is the grain size. The charge transport in polycrystalline sample is dictated by two factors; scattering due to grain boundaries and scattering within the grain interior. The relative contributions to the overall resistance is given by the above described scaling law. For large grain size (> 10 µm), the contribution from the R_s^0 is dominating the overall resistance R_s, and R_s is independent of the grain size. For grain size less than ≈ 0.1 µm, the grain boundary resistivity ρ_{gb}, dominates the overall resistance, and R_s scales inversely as a function grain size. The transition from the grain- to grain boundary dominated behavior occurs at $l_g \approx \frac{\rho_{gb}}{R_s^0}$.

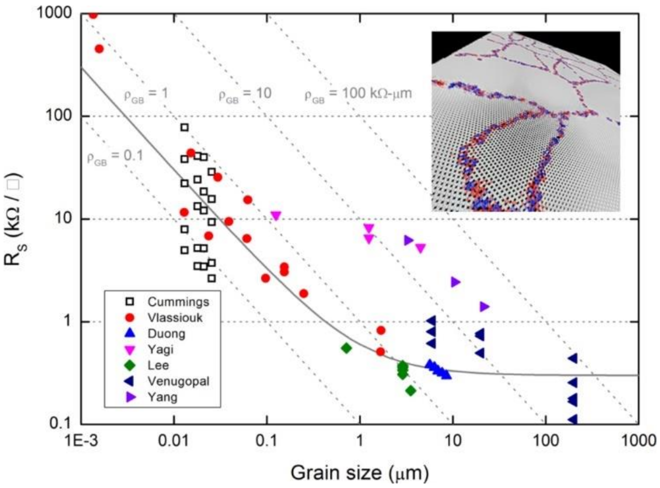

Figure 2.5: Dependence of sheet resistance as a function of grain size in polycrystalline graphene. The solid colored and open symbols correspond to the measured and the calculated values, and the solid line is according to the scaling law behavior described in the text. The parameters used in the scaling law are: $\boldsymbol{R_s^0}$ = 300 Ohm/Sq. and $\boldsymbol{\rho_{gb} = 0.3}$ kOhm µm. Reproduced from [[38]].

In the region where the grain size is in the nanometre-range, the electrical transport is governed by the thermally activated variable range hoping (VRH) model. In nanograined systems, the electrical transport is governed by ratio of the tunnelling conductance between the adjoining grains σ_t and quantum conductance, $\sigma_q = e^2/h$. When $\frac{\sigma_t}{\sigma_q} < 1$, the charge carriers are strongly localized within the grain and the electrical transport follows the thermally activated VRH process.[41] For systems with negligible Coulomb interactions between the carriers in the adjoining grains, the temperature dependent electrical conductivity, $\sigma(T)$ is described by the Mott law.[42] In the 2D case, it is given by the relation

$$\sigma(T) = \sigma_0 exp\left[\left(-\frac{T_1}{T}\right)^{1/3}\right] \qquad (2.6)$$

Where the parameter T_1 depends on the localized density of states at the Fermi level, spatial extent of the wavefunctions spread determined by the tunnelling conductance between the adjoining grains.

2.4 Carbon nanotubes

Carbon nanotubes can be visualized as a rolled-up graphene sheet. As there are numerous ways of rolling-up a graphene sheet into a nanotube, a vast number of single-walled carbon nanotubes (SWCNTs) can be realized with varying diameters and electronic properties.[23] In SWCNTs, the delocalized pi electrons can now propagate along the length of the tube, but have their motion constrained in the direction perpendicular to the nanotube axis due to the tube diameter. Nanotubes are hence regarded as one-dimensional (1D) materials.

The graphene honeycomb lattice is shown in the **Figure 2.3**. Indicated in the lattice are the fundamental translation vectors $\mathbf{a_1}$ and $\mathbf{a_2}$. The rolling-up of the graphene sheet results in the conversion of one of the translation lattice vectors into the nanotube circumference. The circumferential vector is given by the relation[23]

$$C_h = n\boldsymbol{a_1} + m\boldsymbol{a_2} \tag{2.7}$$

In the above relation, n and m are integers with the axis of the tube perpendicular to C_h. The circumferential vector is also called as the chiral vector.

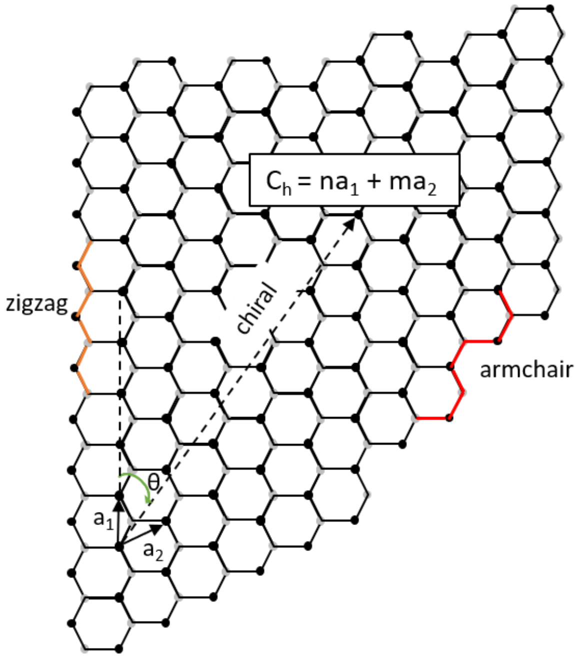

Figure 2.6: Sheet of graphene with lattice vectors $\mathbf{a_1}$ and $\mathbf{a_2}$. The chiral vector and chiral angle for a nanotube are also indicated.

The nanotube diameter can be described using the chiral indices (n, m) as following.[28]

$$d = \sqrt{n^2 + m^2 + n \cdot m} \cdot a_{C-C} \cdot \frac{\sqrt{3}}{\pi} \qquad (2.8)$$

The circumferential vectors can be classified into three types, those with m = 0, m = n and m ≠ n. These classifications of nanotubes are known as 'zigzag', 'armchair' and 'chiral', respectively. The chiral angle is defined as the angle between **a₁** (zigzag direction) and the chiral vector.

$$\theta = \tan^{-1} \frac{\sqrt{3}m}{2n + m} \qquad (2.9)$$

Due to the zero gap at the K point in the Brillouin zone, graphene is a semimetal. On the other hand, the CNTs can be either metallic or semiconducting. The condition for metallic CNTs is:

$$\mathrm{n - m = 3p} \qquad (2.10)$$

where p is an integer and can be either negative, zero or positive. Outside of this condition, the nanotubes are semiconducting with a finite energy gap. In the above relation, for the condition n = m (armchair), the SWCNTs are metallic type. Further, zigzag tubes are also metallic when m = 0 and n is multiples of 3. For 1D system like nanotubes, the energy levels around the circumference are quantized,[23] and the energy levels are given by the relation below.[43]

$$E_q = \frac{2q}{d_t} \cdot a_{C-C} \cdot \gamma_0 \qquad (2.11)$$

In the equation 2.11, the index *q* denotes the transition number. For instance, the first transition (S_{11}) is represented by the index *q* = 1. The second transition (S_{22}) has an index value of 2 and so on. In the equation 2.11, γ_0 represents a value that takes curvature effects into account.[43],[44]

The density of states (D.O.S) defined as the available energy states per unit length for a given band, and has an inverse square root dependence in energy $\frac{|E|}{\sqrt{E^2 - E_q^2}}$ for the condition $|E| > |E_q|$, and zero for $|E| < |E_q|$.[23] Here, E_q is the quantized energy as defined in the equation 2.5. At $|E| = |E_q|$, there is an extremely large density of states and this manifests as spikes in the E versus D.O.S plot. These spikes are known as van Hove singularities.[45] **Figure 2.4** shows the band structure and density of states scheme for metallic and semiconducting carbon nanotubes. Semiconducting tubes have a distinct gap between the top of the valence band and the bottom of the conduction band, on the other hand, metallic tubes have a zero gap as there is an additional linear band passing through the origin. The density of states is non-zero around the Fermi energy level, E_F for the metallic tubes. However, for semiconducting tubes it is zero.

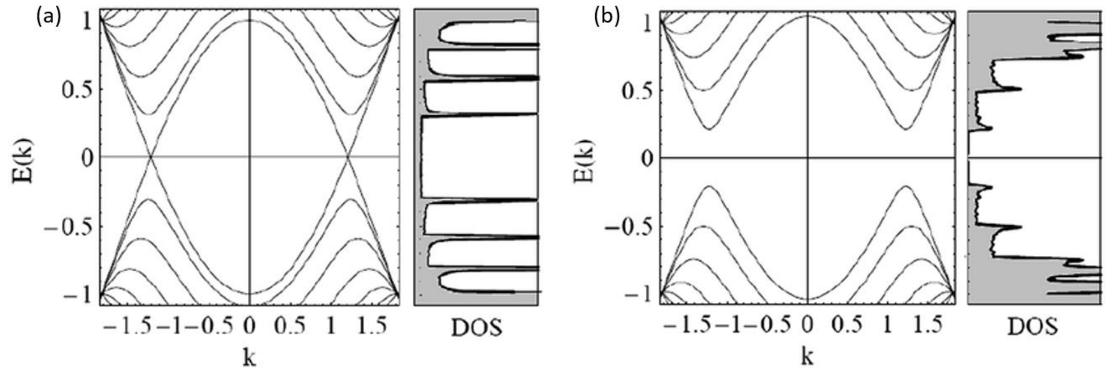

Figure 2.7: Energy band scheme and density of states dependence for (a) (10, 10) metallic type (b) (20, 0) semiconducting type. The Fermi level E_F is located at zero energy. The sharp transition energies indicate the van Hove singularities. Reproduced from [[46]]

Electrical transport in carbon nanotubes

The electrical resistance in the single-walled CNTs is governed by the scattering mechanisms involved in the carrier transport. The ballistic transport in CNT field effect transistors (CNTFETs) becomes important when the device channel length is smaller than the mean free path of the carriers. The mean free path length is determined by the inelastic carrier scattering that occurs with the acoustic phonons in the lattice and is of the order 0.5 µm in semiconducting SWCNTs operating at room temperature and at low energies. In addition, the nature of the contact the CNT makes with electrodes also influences the charge transport where the contact can be either ohmic or Schottky type. The Landauer formalism can be used to estimate the conductance in the one-dimensional CNT channel when bridged between source and drain electrodes. The conductance G, is given by $G = (\frac{2e^2}{h}) \cdot M \cdot T$ with $G_0 = \frac{2e^2}{h}$ = $(12.9\ \mathrm{k\Omega})^{-1}$ being the quantized conductance, M is the number of available modes for the charge transport and T being the transmission probability. The transmission probability, T is equal to 1 for the case of ballistic transport (no back scattering in the channel). For SWCNTs, two conducting channels participate in the electrical transport and therefore conductance is given by $G = 2G_0 = (6.45\ \mathrm{k\Omega})^{-1}$. The above discussion is valid for the case of an ideal SWCNT short-channel device ($L_{ch} \approx 50$ nm) where the scattering effects are negligible. On the other hand, when the channel length is larger than the mean free path of carriers, the carriers undergo collisions in the conduction path, and the transport is no longer ballistic and is instead described by a diffusive mechanism. Furthermore, in a random network of nanotubes, as will be described in Chapter 5, the electrical transport is more complicated and is dependent on several factors: intra and inter-tube transport, bandgap differences in the nanotubes, bundling, intentional and unintentional introduction of defects, and dielectric environment around the nanotubes. The charge transport in dense networks is not only governed by the individual tube segments but also depends on nanotube-nanotube junctions where the charge carriers have to hop over. The junction resistances are on the order of 100 kOhm and depend on the electronic type of the nanotubes, further, the likelihood of hopping or tunneling is greater for nanotubes with a large diameter. The relative orientation between the nanotubes at the junction is also an important factor dictating the overall resistance. The variable range hopping (VRH) model for SWCNT networks is described in the work of Rother et al. and Schießl at al.[47,48] A comprehensive review of electrical transport in SWCNT networks can be found in the work of Zorn et al. [49]

Optical properties of carbon nanotubes

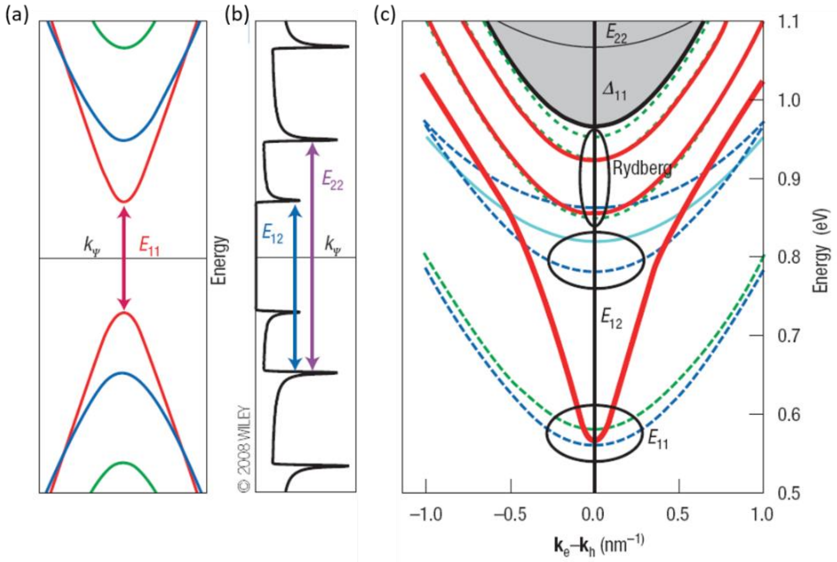

Figure 2.8: Single-particle and excitonic states. (a) Band structure of (19,0) semiconducting SWCNT for the single particle picture. (b) the corresponding density of states. (c) The simulated excitonic picture to describe the optical properties considering the many-body effects. Reproduced from [[11]]

Due their 1D nature, carbon nanotubes have an anisotropic optical response. The light-matter interaction is strongly suppressed when the excitation light is polarized perpendicular to the nanotube axis. The condition for light absorption or emission in CNTs would require the change in quasi-angular momentum to be zero, therefore, the optical transitions between the states in CNTs is possible only for the subbands that obey this selection rule. The optical properties in SWCNT depend sensitively on its band structure. In the one-particle picture, the excitations from interband transitions result in free carriers. However, the interaction of electrons and holes would result in a bound state electron-hole pairs. These bound states are referred to as excitons and exist below the one particle band-to-band transitions. The excitonic transition energies are on the order of several hundred meV, and have an inverse relationship with the nanotube diameter. The electrical and optical properties in nanotubes are described by their respective energy gaps. The electrical bandgap ($E_{eg} \approx E_g + E_{ee}$) and the optical band gap ($E_{eg} \approx E_g + E_{ee} - E_{eh}$) are treated separately, and they are related to the one-particle bandgap, E_g. The E_{ee} and E_{eh} give the interaction energies for electron-electron and electron-hole interactions, respectively. The optical absorption spectra of the nanotubes can be reliably calculated by considering the many body effects involving the e-e and e-h interaction energies. The dielectric environment can strongly modify the electron-electron and electron-hole interactions and result in the red or blue shifts in the excitonic energies.

2.5 Raman fingerprint of nanocarbon materials

2.5.1 Raman spectroscopy of graphene and graphite

Raman spectroscopy is a particularly advantageous non-destructive technique to probe the characteristics of graphene/graphite, carbon nanotubes, and 2D materials. The Raman spectrum of a graphitic material is a rich source of information about the number of layers, defect density, intrinsic doping, and strain. The principle of Raman scattering involves the inelastic scattering of light with the optical phonons in the material; Tuinstra & Koening identified the Raman signature of single-crystal graphite with the G peak at 1575 cm^{-1} (due to the in-plane motion of the carbon atoms in the infinite crystal, E_{2g} mode).[50] In the other forms of graphite like stress-annealed pyrolytic graphite, activated charcoal, lampblack and, commercial graphite an additional peak at 1355 cm^{-1} appears due to the polycrystallinity in the material and the related particle size effects.[50] The intensity of this band is inversely related to the crystallite size (L_a) in the graphitic plane. The A_{1g} mode (active in small crystals or at the boundaries of large crystals) that is otherwise absent in the single crystal graphite becomes Raman active in the polycrystalline sample and is responsible for the origin of the D peak. The Raman spectra of a single layer of graphene has three distinct peaks located at 1350 cm^{-1} (D peak), 1580 cm^{-1} (G peak), and 2700 cm^{-1} (2D peak).[51] The D peak appears due to the presence of structural defects, and is absent in defect-free graphene lattice. The 2D peak arises out of the double phonon scattering and unlike the D peak, the 2D peak is not sensitive to the defects and its intensity is dependent on the number of graphene layers.[52] The shape and intensity of the 2D peak can provide information about the number of layers. In this section, the discussion will be mainly limited to the evolution of Raman spectra of carbon films with a degree of disorder and amorphization.

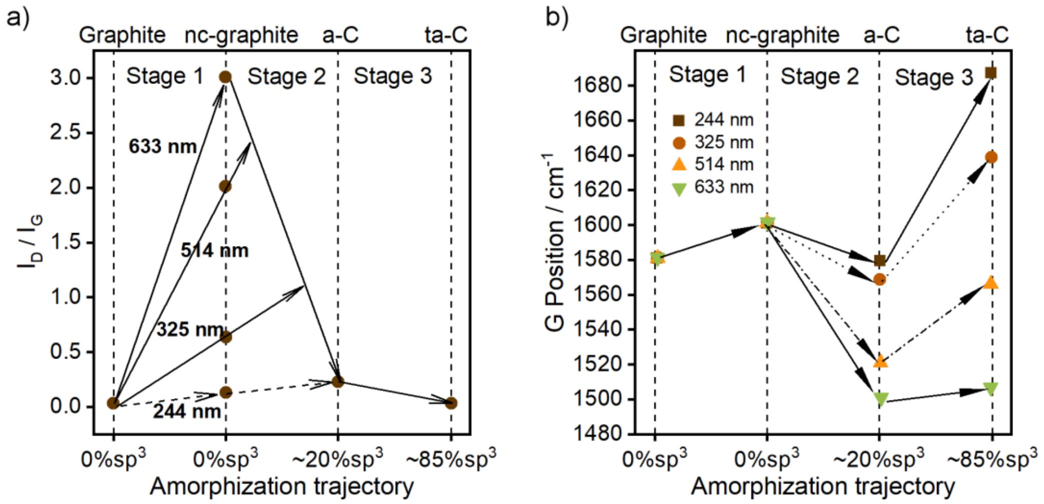

Figure 2.9: Multi-wavelength amorphization trajectory of carbon films for the variation of (a) I_D/I_G ratio and (b) G peak position. Adapted from reference [[53]]

The Raman spectra of carbon films with a varying degree of disorder can be summarized by a three-stage model as introduced by Ferrari and Robertson.[54] **Figure 2.9a** and **Figure 2.9b** show the D-peak to G-peak intensity ratio (I_D/I_G) and the position of the G-peak with the increasing disorder in the carbon films, respectively. Moving along the horizontal axis, starting from graphite to nanocrystalline graphite, to amorphous carbon and in the end to ta-C (tetrahedral amorphous carbon), the carbon film undergoes the following sequence of changes: first, reduction in the size sp^2 groups then followed by topological disorder, and lastly the transition from ring to chain configurations.

In stage 1, the transition from ordered graphite to nanocrystalline graphite results in the shift in G-peak position from 1580 cm^{-1} to 1600 cm^{-1} and a reduction in the in-plane crystallite size (L_a). Further, the D-peak appears, and its intensity increases according to the Tuinstra & Koening (T-K) relation given by $I_D/I_G \propto 1/L_a$. In stage 2, the transition from nc-graphite to a-C results in a G-peak position shift from 1600 cm^{-1} to 1510 cm^{-1} (for 514 nm laser line in **Figure 2.9b**). In the a-C phase, the bonding is predominantly sp^2 with up to a maximum of 20 % sp^3 bonds resulting in a completely disordered sp^2- bonded system. Therefore, as a consequence of large disordering and the decrease in L_a to well below 2 nm, the T-K relation is no longer valid at the end of stage 2. In addition, the I_D/I_G ratio reduces to zero due to the reduction in the number of ordered aromatic rings. In stage 3, the increase in the sp^3 content up to 85 % results from the conversion of sp^2 sites into sp^3 sites and consequently the sp^2 configuration changes from rings to chains. The G peak position now shifts to 1570 cm^{-1} and the $I_D/I_G \approx 0$ due to the absence of sp^2 rings. In **Figure 2.9a** the dispersion in the I_D/I_G ratio for nc-graphite is due to strong dispersion of the D peak which is largest for micro and nanocrystalline graphite[53],[55] ($I_D/I_G \propto 1/E^4$, where E is the laser energy), and the dispersionless G-peak for nc-graphite is due to the presence of only sp^2 rings and absence of disorder. The dispersion in G peak increases with increasing disorder and is evident for the case of a-C and ta-C.

2.5.2 Crystallite size determination in polycrystalline graphite

Cançado et al. proposed a relationship between the crystallite size and the full width at half maximum (FWHM) Γ by measuring the Raman peaks of the nanocrystalline graphite samples with crystallite sizes of 20 nm, 35 nm and 60 nm using five different laser wavelengths.[56],[57] The linear fits to the Γ versus $1/L_a$ plot for all the peaks found Γ to be proportional to $(1/L_a)$ and with a negligible dependence on the laser energy.

Table 2.1: Linear fit parameters obtained from the experimental FWHM of G and D peaks.[57]

FWHM	**A /cm^{-1}**	**B / cm^{-1}nm**
Γ_D	19	500
Γ_G	11	560

From the FWHM peak widths, using the relation $\Gamma = A + BL_a^{-1}$ with A and B as the linear fit parameters (**Table 2.1**) the crystallite size in an unknown nc-graphite sample can be hence determined.

2.5.3 Raman spectroscopy of carbon nanotubes

The Raman spectrum of carbon nanotubes provides information about the CNT diameter and chirality. Compared to graphene, the Raman signal of CNTs is stronger due to the resonant Raman scattering involved because the presence of a direct optical bandgap. The rolling up of graphene sheet into a nanotube modifies its phonon dispersion relation, the signature of which is evidenced in the Raman spectrum as a low energy phonon mode. The low-energy phonon mode or out-of-plane vibration that is absent in the graphene appears in the nanotube spectrum as a radial breathing mode (RBM).[58] The SWCNT diameter can be determined from the RBM mode frequency. In SWCNTs, the G-mode (high-energy phonon mode) splits into two peaks depending on the vibration mode, whether it is parallel or perpendicular to the nanotube axis.

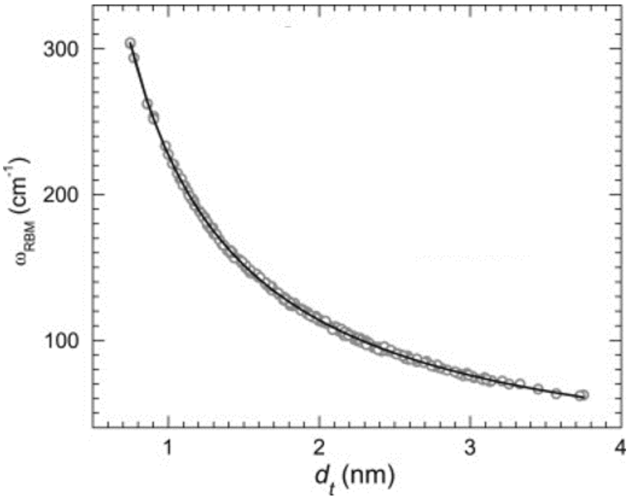

Figure 2.10: Measured radial breathing mode frequency (ω_{RBM}) as a function of the nanotube diameter. Open circles represent the data and the solid line is the fit to the data. Fitting parameters shown in the equation 2.12. Reproduced from [[59]]

The Raman active vibration mode in SWCNT has an inverse relationship to its diameter. The simple relation between the tube diameter and its frequency is given by the below relation where A and B are empirical constants and d_t being the CNT diameter. For a single isolated tube when the environmental effects are negligible, B is close to zero. In **Figure 2.10,** diameter range in 1 - 4 nm of isolated SWCNTs on silicon substrate were studied, and the experimental data was fitted with the eqn. 2.12 and the obtained values of the fitting parameters A and B are 227 cm^{-1} nm and 0.3 cm^{-1}, respectively.[60]

$$\omega_i(d_t) = \frac{A}{d_t} + B \tag{2.12}$$

Depending on the nanotube environment (substrate, solvent effects, bundling and preparation methods) the $\omega_i(d_t)$ relation varies. Araujo et al. summarized the literature reported values for A and B.[59]

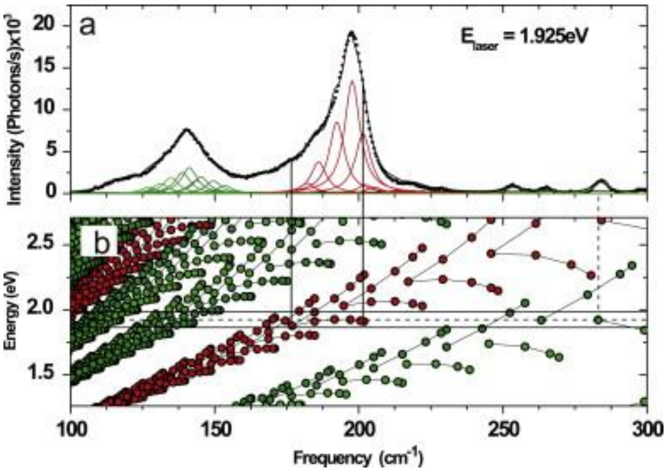

Figure 2.11: (a) Measured Raman spectrum (black bullets) at 644 nm laser line. The spectrum is fitted with individual Lorentizians (in color) and the global fit is shown in black solid line. (b) The dashed line on the Kataura plot indicates the laser excitation energy (1.925 eV) and the solid lines at (E_{laser} ± 0.06) eV indicate the resonance window. Reproduced from [[59]]

From Raman spectroscopy, the (n, m) indices to SWCNTs can be identified from the 2D plot of (exitonic transition energies) E_{ii} vs RBM frequency or diameter d_t, the so-called Kataura plot (see **Figure 2.11**). For assigning (n,m), one of the transition energies (van Hove singularities) must lie near the laser excitation energies. The transition energies were calculated empirically by A. Jorio et. al. Each filled circle in the plot represent the transition energy for either metallic or semiconducting nanotubes. Starting from the bottom, the first grouping (in green & olive) represents E_{22}^{S} (the E_{11}^{S} transitions are further below the E_{22}^{S}, and in the plot only one data point can be visible at the bottom right corner), the second grouping (in red) respresents the E_{11}^{M}. The light green and olive circles represent the semiconductig tube with type mod(2n+m, 3) = 1 and mod(2n+m, 3) = 2, respectively. The red circles represent the metallic type tubes with mod(2n+m, 3) = 0. Further, within each grouping, several branches or families can exist that satisfy the condition 2n+m=const.

In **Figure 2.11a**, the plot in black closed circle show the data, and the solid black line show the overall fit to the data obtained by fitting Lorentizians (individual green and red curves).These solid color lines represent tubes with a distribution of RBM frequencies, that is each nanotube is related to a specific RBM mode. The RBM in red and green correspond to metallic and semiconducting tubes, respectively. The excitation energy (1.925 eV) is shown as a dashed line, and the solid lines at E_{exc}±0.06 eV (resonance window width) give the approximate edge cases for the RBM profiles. Therefore, for fitting of the data in **Figure 2.11a**, the red circles in **Figure 2.11b** should fall within the boundary set by the solid lines of the laser excitation. In this case, the vertical lines connecting the two figures indicate the family of metallic tubes 2n+m=30 in resonance.

2.6 Synthesis methods for nanocrystalline graphite

Nanocrystalline graphene or graphite films could be synthesized by high temperature graphitization of a solid carbon source like photoresist film or self-assembled monolayers (SAMs). Turchanin et al. demonstrated that the conversion of aromatic self-assembled monolayers to single or a few-layer nanocrystalline graphene occurs when the SAM layer is irradiated with a high dose of electron beam.[35] The exposure to the electron beam transforms the SAM layer into supramolecular nanosheet due to the cross-linking of the aromatic molecules in the SAM layer. Subsequent thermal annealing transforms the molecular nanosheet into single to few-layer NCG. The resulting NCG films after annealing had a lateral domain size in the range 2-5 nm. In another report, Zhang and coworkers showed a catalyst free growth of NCG (few nm to tens of nm in thickness) by graphitizing positive photoresist films obtained via. spincoating.[61] The thickness of the NCG films was controlled by adjusting the photoresist layer thickness. Furthermore, it was shown that uniformly thick NCG films could be obtained on different substrates including SiO_2/Si, Cu, quartz, and Al_2O_3. The X-ray photon electron spectroscopy (XPS) peak of C(1s) at 284.8 eV and the G peak position (1600 cm^{-1}) from Raman spectroscopy confirmed that the synthesized films have graphene-like sp^2 hybridization, and the hexagonal crystallinity was identified from the selected area diffraction (SAED) pattern. Riaz et al.[37] and Yekani et al. have also similarly reported the NCG film synthesis by graphitizing a positive photoresist S1805. Yekani et al.[62] realized the partly suspended NCG films through graphitization of the photoresist layer on Germanium substrate. This was possible due to the formation of cavities in Ge when heated close its melting point (927^{o}C). Depending on the crystallographic orientation of the Ge substrate, either pits or trenches are formed on which the NCG is suspended.

Jerng et al.[63] reported the synthesis of NCG films on sapphire and magnesium oxide (MgO) substrates using molecular beam epitaxy (MBE) in ultra-high vacuum, where pyrolitic graphite was heated to a high temperature and the sublimated carbon was then used as the graphitic feed source. In another report, thickness controlled NCG films up to monolayers were deposited directly on the dielectric substrates at 1000^{o}C by catalyst-free chemical vapor deposition (CVD) process.[64] CH_4 or C_2H_2 was used as precursor gas in presence of reducing (H_2) and carrier (Ar) gases. Low temperature growth (substrate temperature at 600^{o}C) of NCG films was reported by Guerra et al.[65] using remote plasma-enhanced chemical vapor deposition (RPECVD) process in which the plasma formed at high temperature is separated from the substrate surface that is at a relatively low temperature. The different plasma and substrates temperature allow the applicability of RPECVD technique to a wide range of substrates. In a recent study, Zhao et al.[66] reported on the ultrafast growth of 1 nm thick NCG films by rapid quenching. Ethanol and Pt foil were used as a liquid carbon source and substrate. Room temperature quenching of high temperature Pt foil in ethanol resulted in NCG formation. Further, the grain size in NCG film was controlled by the onset temperature of the metal foil.

In this section a brief overview of some of the waferscale synthesis routes of NCG have been discussed but a detailed overview of various other nanocrystalline graphene synthesis routes is described in the review article by Simionescu et al.[67]

2.7 Photoresponse of nanocarbon materials

In photodetectors, the light absorbed in the optically active region is converted into electrical signals; the photodetection mechanisms responsible for the optoelectronic conversion can be broadly categorized into two types, depending on whether the absorbed energy is either used for generating excess carriers or in excess carrier heat. Excess carriers are generated by optical transitions across a semiconducting bandgap in the former, and in later, there is a rise in carrier temperature due to light absorption. The photoresponse in both scenarios is measured as either photocurrent or photovoltage. The following section describes the key photodetector figure of merits,[16] followed by the photodetection mechanisms.

2.7.1 Photodetection mechnaisms

Responsivity, R: The responsivity is the ratio of photocurrent/photovoltage generated to the incident optical power. S*pectral photoresponsivity* is defined as the responsivity as a function of incident wavelength/photon energy, and this quantity depends on the wavelength-dependent absorption of the photoactive material.

$$\mathrm{R} = \frac{\text{current or voltage generated}}{\text{incident optical power}} \tag{2.13}$$

External Quantum efficiency, EQE: ratio between the generated photo-induced carriers per one second to the incident photon flux per second.

$$\mathrm{EQE} = \frac{\text{photocurrent or photovoltage/elementary charge}}{\text{incident optical power/photon energy}} \tag{2.14}$$

Internal Quantum efficiency, IQE:

$$\mathrm{IQE} = \frac{\mathrm{EQE}}{\text{Photon flux absorbed}} \tag{2.15}$$

Noise-equivalent power, NEP: This corresponds to the smallest power that can be detected above the noise floor in a one Hz bandwidth. The main contributions to the noise spectrum of photodetectors arise from the shot noise and thermal noise. The origin of the shot noise (σ_{shot}) is the fluctuations in the background radiation which result in a variation of dark current in the photoactive material. The Johnson or thermal noise ($\sigma_{thermal}$) originates from the random motion of the charge carriers under thermal equilibrium. The noise-equivalent power is given by the following relation.

$$\mathrm{NEP} = \frac{\text{noise spectrum } (\sqrt{\sigma^2_{\text{shot}}+\sigma^2_{\text{thermal}}})}{\text{Responsivity of the photodetector}} \qquad (2.16)$$

Specific detectivity, D*: Another metric to determine the low-level signals is the specific detectivity, which is obtained when the NEP is normalized with the detector active area, and has units, $WHz^{-0.5}$.

$$D^* = \frac{\sqrt{\text{Area}}}{\text{NEP}} \qquad (2.17)$$

The different mechanisms responsible for the generation of photocurrent or photovoltage are first briefly introduced, followed by the discussion in the context of graphene, nanocrystalline graphene, and carbon nanotubes.

Photovoltaic effect

In the photovoltaic mode of operation, no external bias is applied to the device, and the separation of the photoexcited carriers occurs due to the built-in electric field already present in the photoactive area. The built-in fields, for instance, can be due to the Schottky barrier at the metal-semiconductor interface or the doping level difference within a semiconductor at the interface between p- and n- doping regions where the alignment of Fermi levels in the p- and n-regions result in a depletion zone, and thereby an electric field. In photovoltaic mode, either a photocurrent or a photovoltage is measured. In the photocurrent mode (or short-circuit current mode) under light absorption, a short-circuit current is measured due to the built-in field. On the other hand, in the photovoltage mode (or open-circuit mode), the photo-excited carriers with different polarities accumulate and compensate for the internal field, and thereby resulting in a photovoltage. The bias voltage necessary to nullify this photovoltage is called the open-circuit voltage,V_{OC}.

Photoconductive effect

The d.c current flowing in a semiconductor device under an external bias is modified due to the illumination induced conductance change in the material. The magnitude of this conductance change is proportional to the number of free carriers generated under illumination. The excess free carriers generated due to the interband transitions contribute to the increased conductance in the material. The disadvantage of these devices however, is a slow response time. Further, a higher dark current would mean a higher noise-equivalent power and low specific detectivity.[30]

Photo-thermoelectric effect

The previous sections described the generation of electron-hole pairs in photoactive material under light absorption and subsequent separation due to in-built or external electric fields. In addition to the electric-field assisted separation, the photoexcited carriers can undergo a temperature rise due to the carrier-carrier scattering where the carriers reach a thermalized state (or thermal equilibrium), resulting in the formation of hot-carrier distribution governed by Fermi-Dirac statistics.[68] The photoinduced carrier heating creates temperature gradients in the photoactive material, driving photo-thermoelectric (PTE) currents or voltages from the hot end to the cold end due to thermal diffusion of carriers. Further, in the temperature-driven photodetectors, both interband and intraband optical excitations can contribute to the photoresponse. The thermal voltage ΔV generated is proportional to the temperature gradient ΔT, and the proportionality constant is given by the Seebeck coefficient (S).

$$\Delta \mathrm{V} = \mathrm{S} \cdot \Delta \mathrm{T} \qquad (2.18)$$

In metals, the Seebeck coefficient is given by the relation from the Mott formula, where $\sigma(E)$ is the electrical conductivity as a function of energy:

$$S = \frac{\pi^2 k_b^2 T_e}{3q} \frac{1}{\sigma(E_F)} \frac{\partial \sigma(E)}{\partial E} \qquad (2.19)$$

q is the electronic charge, k_b is the Boltzmann constant.

The zero-bias photoesponse in various 2D materials has its origin predominantly in PTE mechanism. For instance, the PTE effects were observed in graphene, MoS_2,[69] at the interface of single-layer and bi-layer graphene,[70] graphene-metal interface,[71] and in suspended graphene devices.[72] Further, a pronounced photothermoelectric effect was also observed in the substrate supported and suspended nanotube films,[73] and within the doped regions in individual nanotube devices.[74]

Photobolometric effect

In the bolometric photodetection, the light absorption modifies the material's conductance due to the heating resulting from the absorption of incident photons, and the change in temperature induced by the light absorption can be hence directly detected. The difference between PV, PTE, and bolometric effect is that an external bias is necessary for bolometric detection. Further, a change in conductance is the measured quantity in a bolometric effect. An advantage of using bolometers for photodetection is that no p-n junctions or material interfaces are required, and they can be operated in a homogenous material. The temperature coefficient of resistance (TCR) is an important figure of merit for bolometers.

$$TCR = \frac{1}{R}\frac{dR}{dT} \tag{2.20}$$

The TCR of the commercially available uncooled vanadium oxide bolometer is about 3%/K.[75] In comparison, TCR of CNT films is less than 1%/K at 300 K.[76]

In the following sections, some of the background results of photodetection in graphene and carbon nanotube devices will be described. For a detailed overview, the reader is referred to the review articles.[16],[15]

2.7.2 Photoresponse in graphene

Photovoltaic effect in Graphene

In graphene, the photoexcited electron-hole pairs are separated by either built-in electric fields at the p-n junction or at the graphene-metal contacts where there is a built-in field due to work function differences between metal and graphene.[77],[78] A photoresponse can also be observed under an externally applied source-drain bias voltage, however, the bias voltage results in a large dark current in graphene and hence e-h separation under an external bias is usually avoided. The p-n junction in the graphene channel is realized by using a split gate geometry, in which the doping level is controlled by tuning the applied gate voltage.[79] The photocurrent direction depends on the electric field direction in the channel.

Photothermoelectric effect in graphene

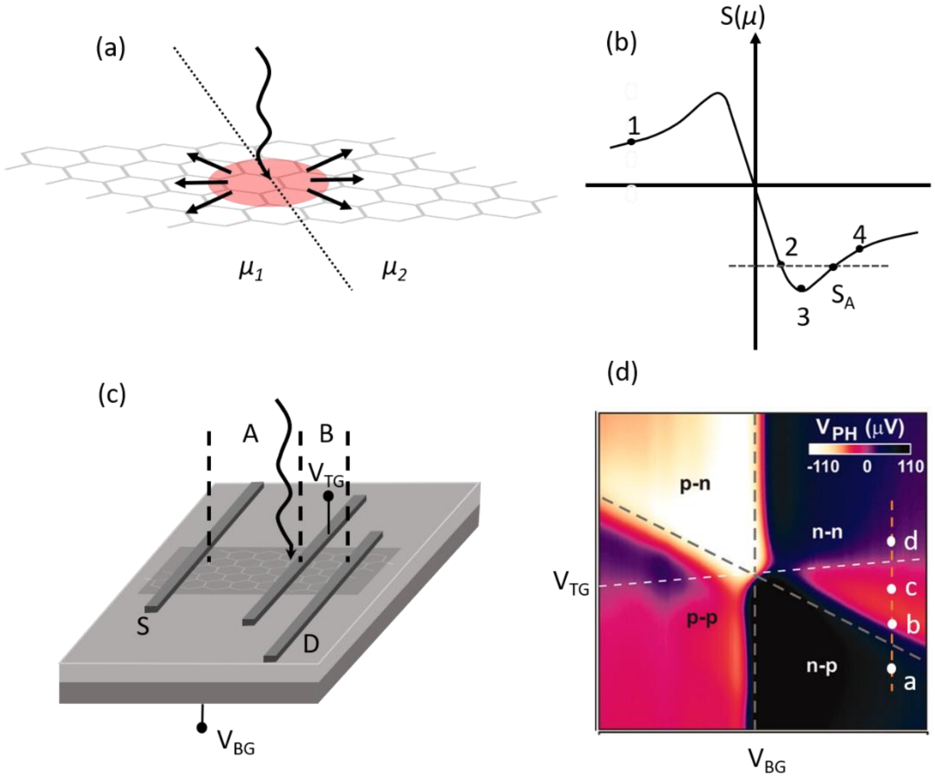

Figure 2.12: (a) Photothermoelectric (PTE) effect in single-layer graphene. Due to the regions with different chemical potentials (μ1 and μ2) there is a net PTE current. (b) Seebeck coefficient variation as a function of the chemical potential. (c) Graphene device with top and back gate configuration to result in a p-n junction in the channel. Region A is controlled by the back gate and the region B is controlled by both top and back gates. (d) Measured photovoltage as a function of different back and top gate voltages. (a), (b) and (c) adapted from [[80]]. (d) reproduced from [[81]].

In graphene, the hot electrons that are generated under illumination contribute to a photovoltage, V_{PTE}, by the photo-thermoelectric (PTE) effect as described in the **Section 2.7.1**. The general relation for the photovoltage generation can be described as below:

$$V_{PTE} = \int S \cdot \nabla T_e \, dx \tag{2.21}$$

In the equation 2.43, the photovoltage is calculated by the integration of local electric field generated due to the temperature gradient induced by the illumination, and a spatial variation in Seebeck coefficient. The induced temperature gradient is due to a difference in electron temperature in between the two regions. The photoexcited electrons in the conduction band rapidly reach thermal equilibrium due to the electron-electron scattering within a time scale of several tens of femtoseconds.[82],[83] This results in a thermal distribution with an electron temperature T_e that is different from the lattice temperature and the surrounding. The hot-carriers can relax through phonon coupling, but in graphene, the optical phonon energy is large (≈200 meV) and hence relaxation through optical phonon scattering is inefficient.[84],[85] Therefore, the elevated temperature of the hot electrons is maintained for several picoseconds without heat transfer to optical phonons. Eventually, the hot-carriers equilibrate and reach the lattice temperature through acoustic phonon scattering on the timescale of nanoseconds.[86]

Now, we will consider the second aspect in the PTE, that is the Seebeck coefficient variation. Gabor et al.[81] observed experimentally PTE effect in a graphene p-n junction where the graphene channel is controlled by tuning the top gate and back gate voltage. In **Figure 2.12a** the chemical potential μ_1 in the region A can be varied by the back gate voltage (V_{bg}), and chemical potential μ_2 in region B by both the top gate voltage (V_{tp}) and back gate voltage. The combination of back gate and top gate voltages can give rise to a six-fold configuration in the region A and region B and the junctions formed are: n-p, n^+-n, n-n^+, p-n, p^+-p and p-p^+. The chemical potential, for instance in the p-p^+ region would be $\mu_2 > \mu_1 > 0$. Using scanning photocurrent spectroscopy, the photovoltage was measured at the interface of region A and region B. From the **Figure 2.12d** it can observed that the photovoltage changes its sign six times as indicated in the map. The sign changes can be understood by considering the Seebeck coefficients in the region A and region B as a function of electrostatic doping in the respective regions. Here, we consider first the change in the Seebeck coefficient of the two regions along the black dashed arrow in the map. This dashed line represents: (i) fixed chemical potential (μ_1) at fixed back gate voltage (V_{bg}); the corresponding Seebeck coefficient (S_A) is indicated in **Figure 2.12b**, (ii) the chemical potential (μ_2) increases as the top gate voltage (V_{tg}) increases. Along the dashed line are marked four locations a, b, c and d that correspond to chemical potential (μ_2). Further, the Seebeck coefficients of the region B are indicated in the **Figure 2.12b**. From the **Figure 2.12d**, the locations at a, c, and d correspond to n-p, n^+-n, and n-n^+ regions and the respective Seebeck coefficients relation are: $S_A > S_B$, $S_A < S_B$, and $S_A < S_B$. and hence multiple sign reversals. However, in the case of location b, the Seebeck coefficient $S_A = S_B$, and due to this uniform Seebeck coefficient, the photovoltage is zero.

Photobolometric effect in graphene

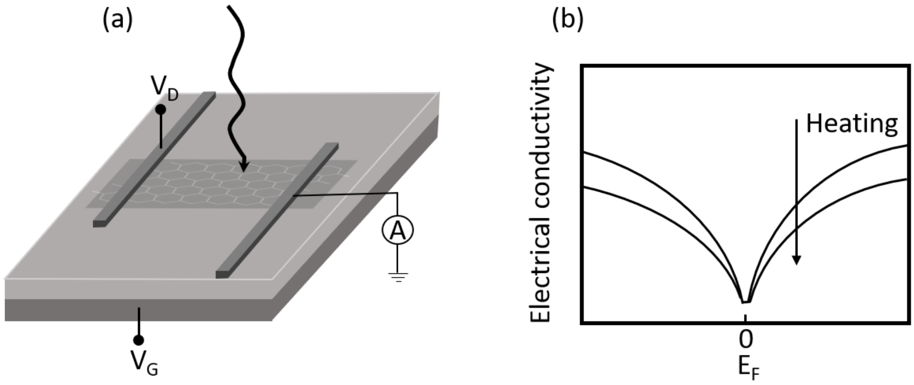

Figure 2.13: (a) Back-gated graphene transistor device geometry for bolometric photodetection. (b) The conductivity decreases due to the light-induced heating in graphene. Adapted from [[80]].

In graphene, with increasing temperature the scattering or collision rate increases, and therefore, there is a reduction in the mobility and consequently, the conductivity is reduced. As described earlier, bolometric photoresponse requires an application of external bias which results in a heating induced reduction in the electrical conductivity. **Figure 2.13a** shows the device structure with transistor configuration for bolometric photocurrent detection. A fixed d.c source-drain bias is applied on the drain electrode, and a variable gate voltage is also applied simultaneously. The total current is the sum of the d.c current (I_{dc}) in the device and the generated photocurrent (I_{ph}). The photocurrent in turn has contributions arising from photovoltaic (I_{pv}) and bolometric (I_{bol}) effects.[87] There is no contribution from the photothermoelectric effect because of the uniform carrier density in the graphene channel, as this gives rise to a uniform Seebeck coefficient. The photovoltaic current is in the direction of the d.c current and the bolometric current has a direction opposite to the d.c current.

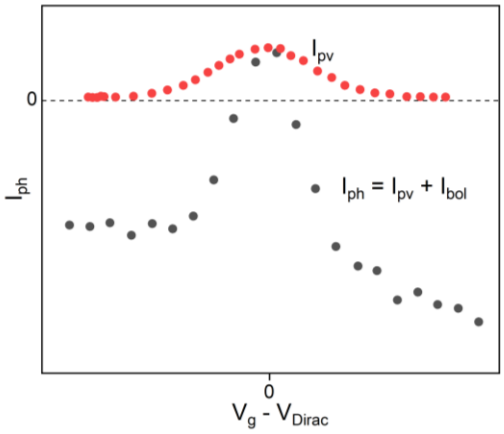

Figure 2.14: Experimentally measured photocurrent (in black) as function of $V_g - V_{Dirac}$. Red circles represent the modelled photovoltaic current Ipv contribution. Adapted and reproduced from [[80,87]].

At large gate voltages, the bolometric photocurrent is stronger due to the increased carrier density from the electrostatic doping. The magnitude of the bolometric current increases as a function of $\left|V_g - V_{Dirac}\right|$. The Dirac voltage, V_{Dirac} is defined as the required gate voltage to tune the Fermi level to the Dirac point. At $V_g = V_{Dirac}$, the photovoltaic current dominates and the photocurrent has a positive sign. However, increasing the gate voltage results in a diminishing contribution from photovoltaic current because of the reduction in nonequilibrium carrier temperature, as the density of photogenerated carriers depends on the nonequilibrium carrier temperature due to an increased collision rate.[87]

2.7.3 Photoresponse in carbon nanotubes

The photoresponse in carbon nanotube devices is influenced by the environment and type of the CNTs bridging the device. Broadly, the photoresponse mechanisms depend on whether the nanotubes are: supported or suspended, metallic or semiconducting, aligned or random orientation, single-tube or networks. Further, device response is also governed by the type of gating (split gates or a single gate), doping type, and doping density of the substrate. In the following, the single-tube photoresponse is described, followed by the photodetection in CNT networks.

Photoresponse in single-tube device

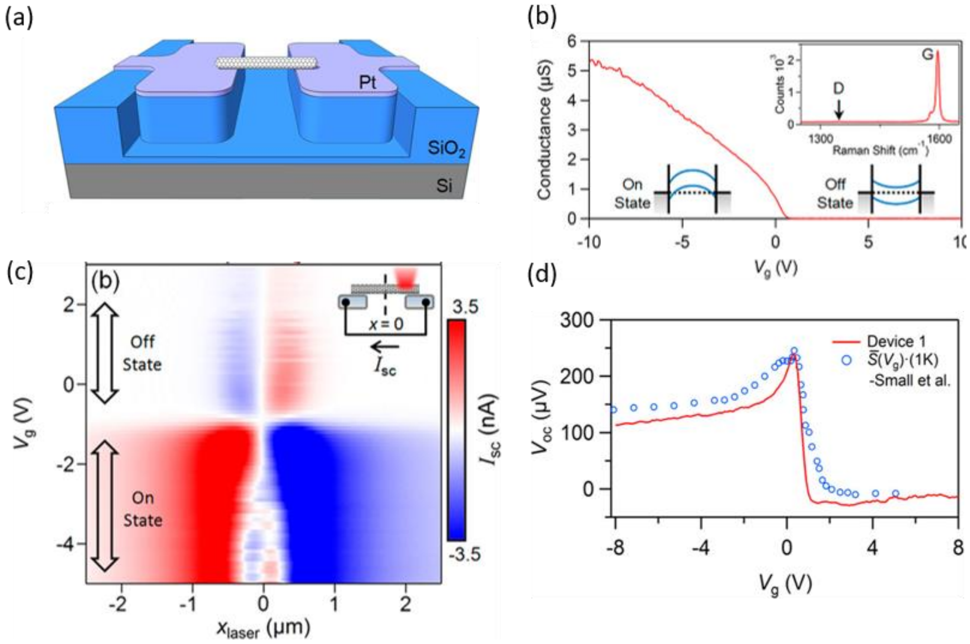

Figure 2.15: (a) suspended sc-SWCNT device (b) transconductance of the device (c) scanning photocurrent map of the device as a function of gate voltage (d) measured open-circuit voltage as a function of gate voltage at a position interior to the electrode away from the CNT-metal edge. Adapted with permission from from [[88]]. Copyright 2014 American Chemical Society.

To differentiate between the photovoltaic and photothermal effects in the semiconducting SWCNTs, T. deborde and co-workers[88] and M. Barkleid et al.[74] studied the photoresponse in suspended CNT devices. The photothermoelectric effects are stronger when the thermal coupling to the substrate is minimized. In the following, the photocurrent response in the suspended sc-SWCNT reported by T. deborde et al. is discussed. As a function of gate voltage, sweeping from the device on-state to off-state, the short-circuit photocurrent current distribution in the channel region undergoes multiple sign changes. Further, a strong spatial extent of the photocurrent was observed several microns into the contact region in the device on-state. The position of the laser spot in the center of the device in **Figure 2.15c** is indicated by $x_{laser} = 0$. Away from the electrode edge and into the contact region, the influence of the suspended part of CNT is negligible as the CNT is not directly illuminated, and hence, the observed photocurrent inside the metal contacts cannot be attributed to a photovoltaic effect. The open-circuit voltage as a function of gate voltage at a distance of x = 1.8 µm (x = 0 µm is the device center) is shown in **Figure 2.15d**, and the gate voltage dependence is identical to the Seebeck coefficient measurement of sc-SWCNT by Small et al. (blue open circles in **Figure 2.15d**).[89] The observed photovoltage corresponds to a temperature difference $\Delta T = 1$ K across the device and was also confirmed by G-mode Raman shift.

The photocurrent signal becomes stronger as the laser spot moves close to the metal-CNT contact. This is understood by the simultaneous light absorption in both the metal electrode and the CNT, and thus resulting in increased ΔT. The photocurrent contribution only from the CNT alone was obtained by recording the photocurrents in parallel and perpendicular directions, and subtracting one from each from each other. Here, parallel direction refers to the condition when polarization of light parallel to the CNT axis. **Figure 2.16a** shows the photocurrent in the parallel direction and in **Figure 2.16b** the difference in photocurrent polarizations, ΔI_{sc} is shown.

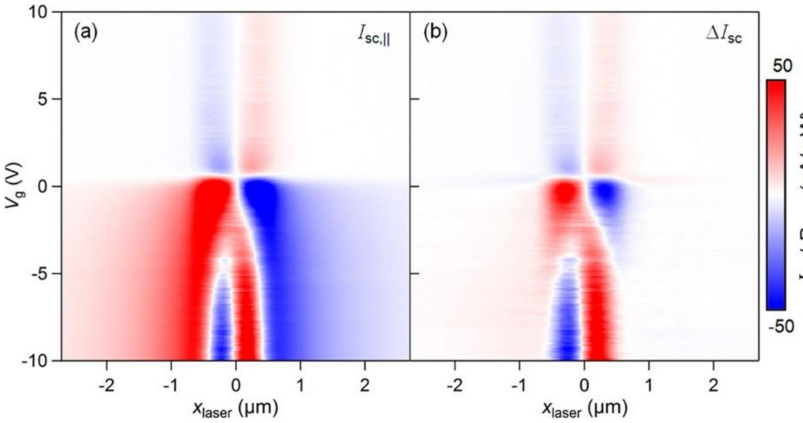

Figure 2.16: Short-circuit photocurrent responsivity maps. (a) scanning photocurrent map with the laser polarization parallel to the nanotube axis. (b) resulting photocurrent map obtained after subtracting the perpendicular polarization map from the parallel polarization map. Adapted with permission from [[88]]. Copyright 2014 American Chemical Society.

First, in the device off state from ΔI_{sc}, the measured photocurrent in the parallel polarization is greater than the perpendicular polarization by a factor 3.5 and secondly, heating of the metal does not contribute to a photocurrent in the off state. Therefore, the photovoltaic effect is the dominant mechanism in the off state. At the transition of on state and off state (at $V_g \approx 0$ V) there is a sudden sign change in the photocurrent and the signal magnitude increases. This sign flip can be understood from the band bending reversal (see **Figure 2.15b** inset cartoon). Further, there is no shift in the position of the peaks at the either side of the gate voltage transition region. The photocurrent peaks occur at $x_{laser} \approx \pm 0.3$ µm for both on and off states. Hence, the mechanism is still photovoltaic at the on/off transition. Now, further into the device on state ($V_g < -3$ V) there is a sign flip and the peaks start to appear at $x_{laser} \approx \pm 0.2$ µm. This sign flip and new peaks cannot be explained by a photovoltaic effect and the origin of these new peaks is attributed to photothermoeletric currents in the device that due to a gradient in hot-carrier temperature at higher negative gate voltages. Due to the bandbending, the Seebeck coefficient (Seebeck coefficient of a p-type CNT is positive) in the device is spatially inhomogeneous. It is larger in the lightly doped regions of the device (contact-CNT region) and is smaller in the highly doped regions (center of the channel) and the polarity of the Seebeck coefficient is consistent with the observed photocurrent ΔI_{sc} in the on state ($V_g < -3$ V).

Photoresponse in CNT networks and films

For photodetection applications, the single tube devices are not efficient due to the low absorption cross-section of the CNTs.[26] Large-area bulk CNT films are required to increase the photodetection efficiency; in particular, aligned films can result in an increase in the absorption efficiency and minimize the multitude of intertube junctions present in random networks. Further, the electronic purity of the network is a critical factor that influences the device performance. The metallic content in the network should be minimized or removed to avoid thermal effects that would dominate the photoresponse and result in a slow device response and low sensitivity.

In the following, the photocurrent mechanisms in random network of CNT films will be briefly reviewed. Zeng et al.[90] reported on the photovoltaic effect in random network of CNTs that are grown using chemical vapor deposition (CVD) on SiO_2/n-Si substrate. The channel region is defined by fabricating asymmetric contacts of scandium (Sc) and palladium (Pd) as source and drain electrodes, respectively. In this configuration, the Fermi level of scandium and the Fermi level of palladium are aligned with the conduction and the valence band of the CNT, respectively (see inset in **Figure 2.17a**). Due to this band alignment, there is a strong built-in electric field along the CNT channel, and since the channel length is comparable to the thickness of dielectric (≈ 500 nm) the built-in field extends throughout the channel region and result in a photovoltaic response under illumination.

In the CNT network, the metallic-CNTs can bridge the contacts directly and short-circuit the channel resulting in a high off state current and negligible gate dependence. The metallic tubes were therefore selectively removed by applying a large gate voltage in the off state and high source-drain bias. This biasing scheme resulted in a selective electrical breakdown of metallic CNTs while not affecting most of the semiconducting CNTs. The channel showed a p-type dependence after the electrical biasing treatment. However, the multiple CNT-CNT junctions between the contacts still result in a large contribution to the series resistance of the device. Additionally, the m-CNT and s-CNT junctions result in large Schottky barriers (junction resistance up to several hundred kΩ).

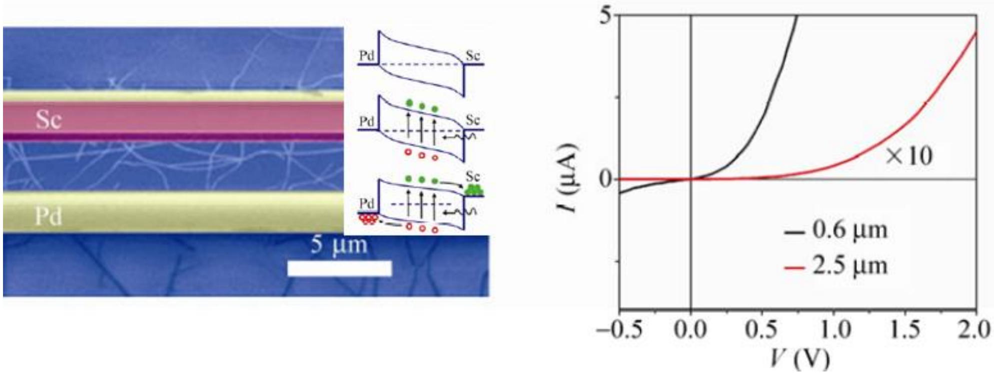

Figure 2.17: (a) SEM image of CNT network device with 2.5 µm channel length. (b) I-V characteristics of the devices with channel length 0.6 µm and 2.5 µm. Reproduced from [[90]].

The CNT-CNT junction density increases with the increase in channel length and result in an increased device resistance. In the channel with multiple junctions, the built-in electric field is much weakened in comparison to the device with aligned tubes or a short channel length (see **Figure 2.17b**). The photovoltaic efficiency of the device therefore decreases with increasing junction density as the band bending becomes less effective in separating the photogenerated carriers. The electrical transport in the devices with large channel length within the network is described by a percolation transport and on the other hand, a direct transport dictates the transport behavior in the short channel devices.

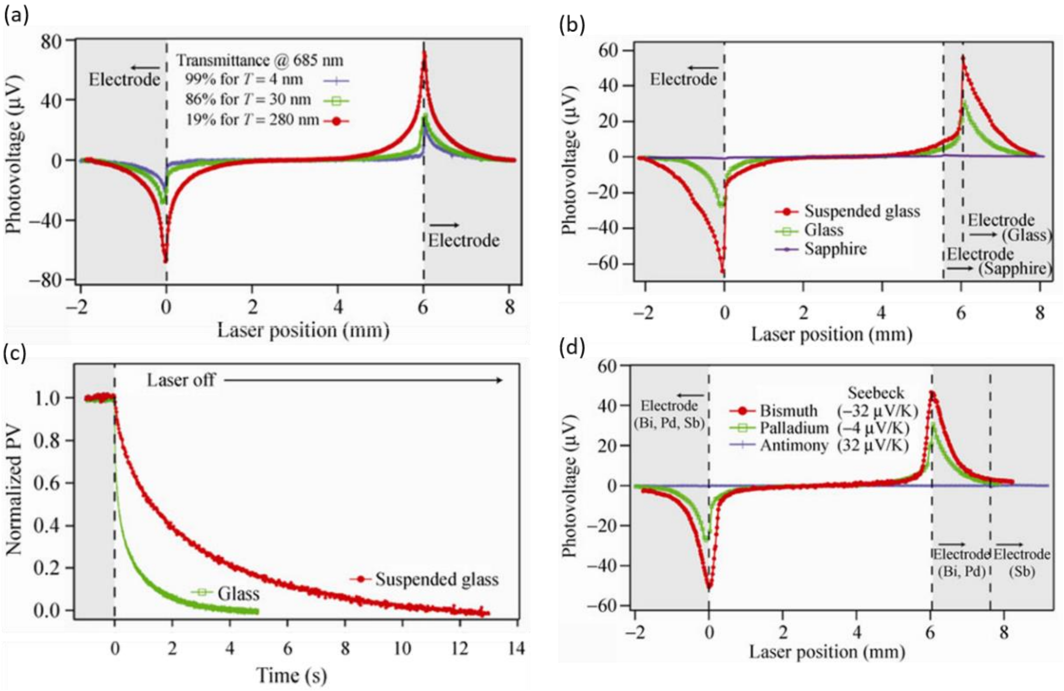

Figure 2.18: Scanning photovoltage profiles obtained with the laser being scanned across the length of the device for (a) Different thicknesses of the CNT film. (b) Different substrates. (c) Time-dependent behavior on different substrates. (d) Different contact metals. Reproduced from [[91]]

The Martel group investigated photothermoelectric effects in suspended and substate-supported bulk CNT films.[91] Symmetrical metal contacts were used in their scanning photovoltage measurements, and a sign change in the photoresponse was observed at the electrodes (**Figure 2.18a**). The sign change at the electrodes is similar to a photovoltaic response arising from the Schottky barrier at the metal-CNT contact in single-tube devices. However, here, the origin of the photoresponse was attributed to a photothermoelectric (PTE) effect arising from spatial variation in the Seebeck coefficient and a temperature difference between the illuminated and dark contacts as described in the case of single-tube device. The PTE effect is also dominant in the films that were substrate supported, as shown in **Figure 2.18b**.

The strength of the photovoltage depends on the thickness of the CNT film (**Figure 2.18a**). Thicker films have larger optical absorption and give rise to a strong response. However, the strength of the signal does not vary linearly with the film thickness, and the 4 nm thin film has only four times lower amplitude than the 280 nm thick film. One would have expected a much larger contrast in signal strength between the two films for a photovoltaic effect. Therefore, the nonlinear variation in the signal strength between the two film thicknesses indicates a thermal mechanism, and the critical factor influencing the response is the temperature rise at the contact. Additionally, the magnitude of the photovoltage generated at the metal contact-CNT interface depends sensitively on the thermal conductivity of the substrate. Using a substrate with high thermal conductivity (sapphire) strongly reduced the photovoltage signal, and on the other hand, a low thermal conductivity substrate like glass enhances the photoresponse. However, as shown in **Figure 2.18c**, the response time was much slower in the glass. A typical characteristic of photothermoelectric detectors is the relation between the speed and thermal conductivity of the substrate. The largest photoresponse is obtained for the devices with the largest difference in the Seebeck coefficient between the contact metal and the CNT film (**Figure 2.18d**). The largest difference in the Seebeck coefficient is for bismuth, and the smallest is for antimony. For p-type CNT films, the Seebeck coefficient is ≈ 30 μV/K.

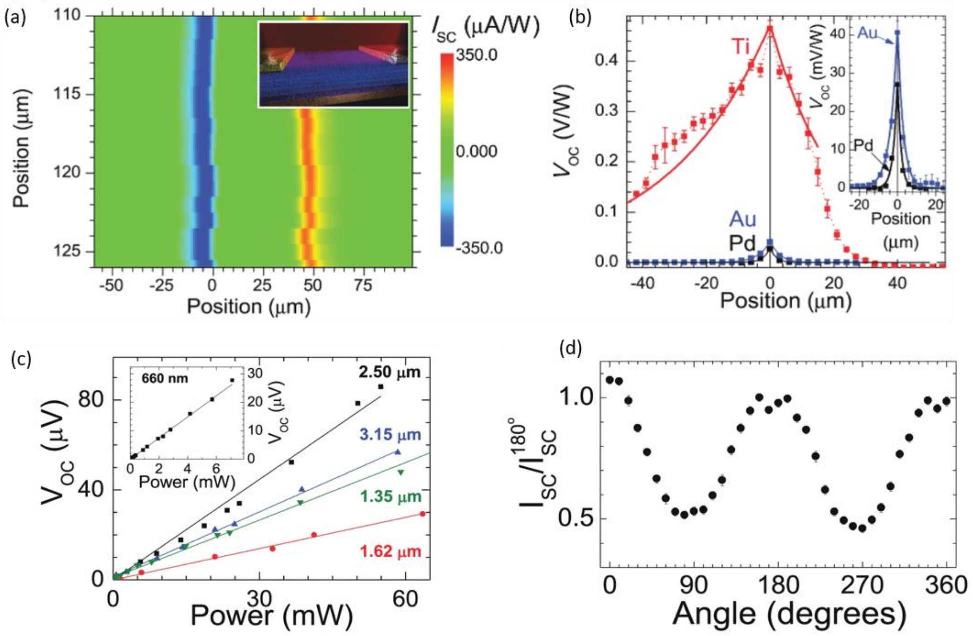

Figure 2.19: Photoresponse of the aligned CNT film (a) Short-circuit photocurrent map with the strongest signal at the electrodes. Inset shows the cartoon of the device with the aligned tubes. (b) Open-circuit voltage (VOC) with different electrode metals. (c) measured open-circuit voltage at various NIR wavelengths as a function of laser power. (d) Polarization dependence of the photocurrent. Reproduced from [[92]]

The above discussion on photoresponse in CNTs was based on random/disordered networks, and the photoresponse was polarization insensitive. In order to study the polarization sensitivity of the nanotube network, Nanot et al.[92] realized devices fabricated on SiO_2/Si out of aligned CNT films. These devices demonstrated a broad band response (**Figure 2.19c**) from visible to mid-infrared. The thickness of the transferred CNT film is 600 nm, and the device channel length is 50 μm. Symmetric contacts (**Figure 2.19b**) with various metals (Au, Pd, Ti) were studied using scanning photocurrent measurement, and the largest PTE effect was observed in the case of titanium-CNT interface due to a large temperature change compared to devices with other metal electrodes. Zero-bias photovoltage/photocurrent signals were observed at the metal-CNT contacts with sign changes at the electrodes, identical to the above discussed devices out of single-tube and random networks. The aligned films showed a polarization sensitive photoresponse with a polarization ratio of 0.5 between parallel and perpendicular polarization excitations.

2.7.4 Photoresponse in nanocrystalline graphene

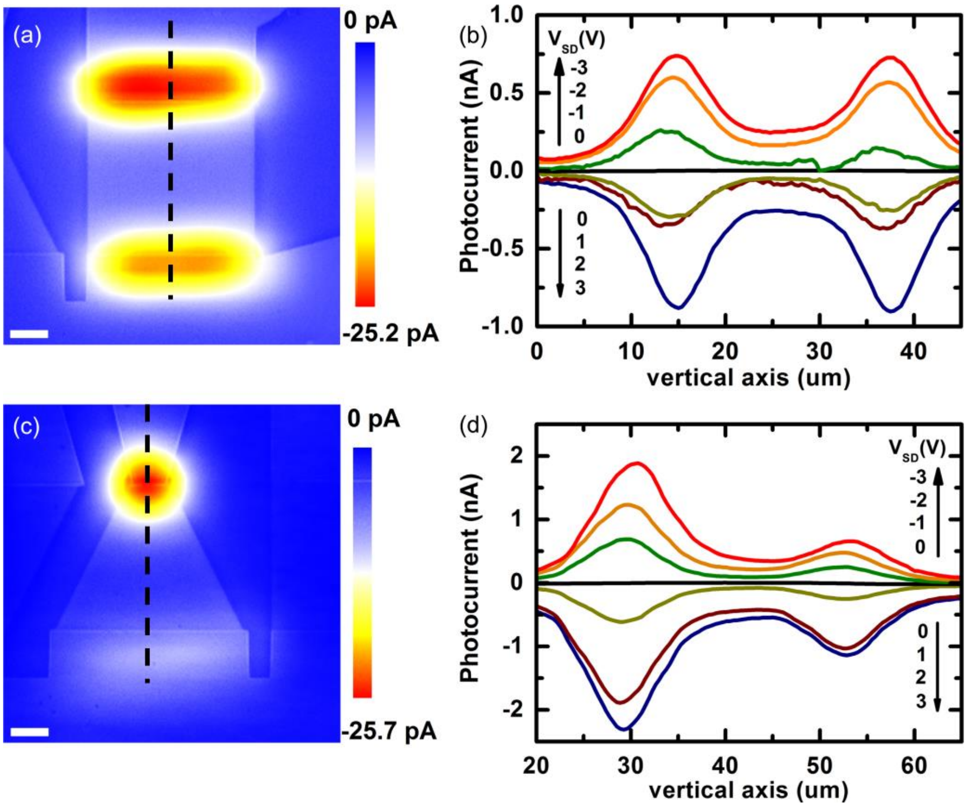

Figure 2.20: Photocurrent maps under a source-drain bias of 1 V at 1064 nm (a) Square shaped device. (b) Photocurrent profile obtained from the line-cut in (a) at different bias voltages. (c) Photocurrent from a triangular shaped device. (d) Photocurrent profile obtained from the line-cut in (d) Reproduced from [[37]]

In the earlier works on NCG for optoelectronic applications, NCG was used as a transparent electrode but not as a photoactive channel material.[36] Riaz et al.[37] have studied the photocurrent behavior in NCG (as a channel material) synthesized by photoresist graphitization on 800 nm-SiO_2/Si substrate. The source (S) and drain (D) contacts from tungsten were fabricated on 4 nm thick NCG film in two device designs - a square-shaped, and a triangular-shaped device (**Figure 2.20a, c**). The respective line cuts (dashed lines in **Figure 2.20b,d)** give the spatial variation in the photocurrent intensity. The photodetection mechanism in the NCG devices was attributed to a bolometric effect. The bolometric effect in NCG can be understood from the variable range hopping (VRH) mechanism described in **Section 2.3**. Under illumination, and applied S-D bias, the conductance in the NCG film increases due to the activation of the VRH process as a result of local rise in temperature in the film. This is in contrast to the earlier described bolometric photodetection in graphene, where the conductance decreases under illumination. On the other hand, in NCG, the grain-to-grain tunneling is responsible for the increased conductance. Further, the bolometric photocurrent is maximized at the metal-NCG interface due to a large device resistance at the contacts where the potential drop (electric field) is largest. Therefore, in the square-shaped device, the maximum photocurrent signal was observed at the metal – NCG interface (see **Figure 2.20a**). In order to maximize the potential drop within the channel, the NCG film was patterned into a triangular-shaped device (**Figure 2.20c**), resulting in the maximum photocurrent signal in the center of the channel. However, the photoresponsivity is only $1.7 \cdot 10^{-6}$ A W^{-1} at 1065 nm, which is two orders of magnitude lower than that reported for graphene.[87] The low bolometric responsivity is due to increased resistance due to the nanometre grain size and non-optimized thickness of NCG for maximum light absorption. In **Chapter 4,** the near-infrared photocurrent signal from the thickness-optimized NCG is discussed. Further, as shown, the light absorption in NCG also depends on the oxide thickness of the silicon substrate.

2.8 Plasmonic nanostructures

Plasmonics deals with the optical confinement and field enhancements at a sub-wavelength scale.[93] The sub-wavelength confinement for enhanced light-matter interaction has been exploited in optical device applications that include imaging, metamaterials, photodetectors, and light emission.[94–97] In addition, plasmonic platforms have been employed in biosensing for the detection of weak fluorescence signals in the pico- to femto-molar range.[98,99] Since their plasma frequency is in the visible spectral region, gold and silver are commonly used as plasmonic materials. The metallic plasmonic nanostructures such as dimers, trimers and split-ring resonators have shown to demonstrate a strong local field enhancement effect.[100–102] Depending on their size, structure and geometry, the optical resonances in the plasmonic nanostructures can be tuned to a narrow spectral region. These structures are advantageous for narrowband applications in the visible spectrum. On the other hand, by integrating plasmonic nanostructures with photonic crystals, a class of hybrid plasmonic-photonic structures could be realized with the optical resonances extending from the visible to near-infrared regions. The so-called stacked complementary plasmo-photonic structures have been demonstrated for the simultaneous enhancement of Raman and fluorescent signals in biomarker molecules.[103–105] The main advantage of the plasmonic-photonic structures, is that in plasmonic structures, the EM field distribution around the structure is often confined to air or transparent substrates with limited photonic density of states (DOS). On the other hand, by integrating with photonic structures such as silicon photonic crystals, the hybrid plasmonic-photonic systems with large DOS and high-quality factors can be accessed.

Chapter 3 Experimental techniques

The following section deals with the materials and experimental techniques involved in the fabrication, and characterization (structural, optical, and electrical) of NCG and CNT devices. The synthesis details and thickness optimization study of NCG films for near-infrared photodetection will be dealt with in **chapter 4**. The large-diameter CNT (LD-CNT) films were grown on SiO_2/Si substrates in the group of Prof. Chang Liu at the Institute of Metals Research, Shenyang. The synthesis details and the related photoresponse behavior of the LD-CNT film devices are presented in **chapter 5**.

3.1 NCG synthesis method

Thermally grown 300 nm-SiO_2 on p-Si (boron doped, $\rho < 0.005\ \Omega cm$, Active Business Company) wafers were cut into 10 mm x 10 mm size, sonicated in acetone, rinsed with isopropanol, and exposed to a mild oxygen plasma. A pre-baking step at 110 °C on a hot plate for 120 s removed physisorbed water. NCG films were grown on the soft-baked SiO_2/Si substrates using S1805 photoresist (Microposit) as carbon source. The photoresist was diluted using Propylene Glycol Monomethyl Ether Acetate (PGMEA), and 35 µl of the prepared resist solution was spin-coated at a set rotation speed for 30 s to achieve the targeted thickness. The process flow of the NCG preparation is shown in **Figure 3.1.**

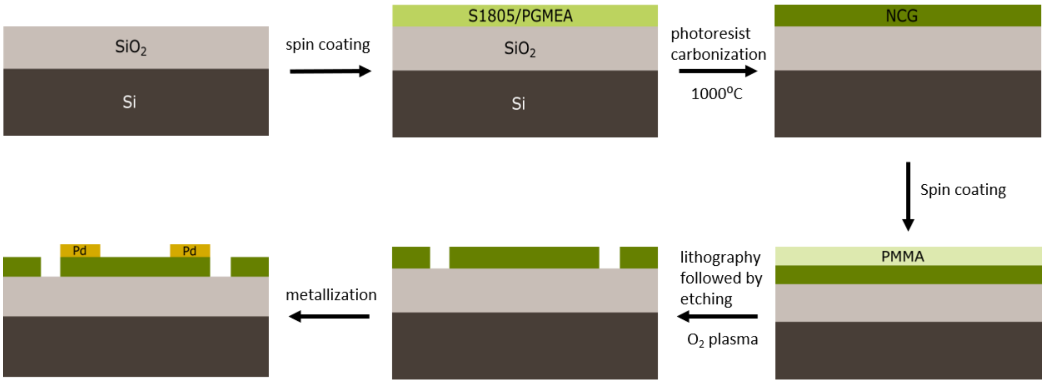

Figure 3.1: Process flow of NCG synthesis and device fabrication

The spin-coated substrates were baked at 110 °C for 60 s on a hot plate to allow outgassing of the solvent. After the post-baking step, the substrates were loaded into the vacuum furnace (Gero Sr-A 70-500/11) equipped with quartz glass tube, turbo pump and controller module for graphitization of the photoresist film at 1000 °C at 10^{-6} mbar pressure. The temperature was increased to 1000 °C at a rate of 10 °C per minute and a holding time of 10 hours.

3.2 Atomic force microscopy

The thickness of the synthesized NCG films was characterized by an atomic force microscope (Bruker Dimension Icon) in tapping mode; the AFM scanner head is attached to the Nanoscope V controller and controlled through the NanoScope software (version 9.7). Images of 5 µm x 5 µm scan area were acquired at 0.5 Hz scan rate in ambient conditions with Tap300-AlG silicon probe (fundamental resonance frequency 300 kHz). The amplitude setpoint, feedback controls and scan rate were adjusted in the control software before each scan to optimize the image quality. The visualization and analysis of the acquired AFM images was done using the Gwyddion 2.58 software.

3.3 Scanning electron microscopy

The scanning electron microscopy (SEM) images of the fabricated CNT and NCG devices were acquired with a Zeiss Ultra Plus field emission microscope at a 1 kV electron high-tension voltage (EHT) using an immersion lens (in-lens) secondary electron detector at a working distance of 2.3 mm with a 20 µm aperture.

3.4 Raman spectroscopy

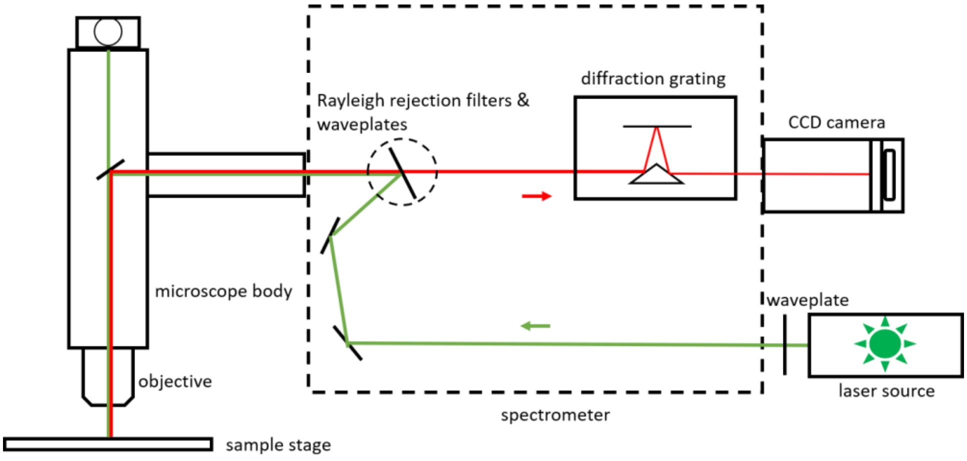

Figure 3.2: Raman microscopy setup (Renishaw inVia)

The Raman measurements were conducted at room temperature in ambient conditions using a Renishaw inVia microscope at 532 nm and 785 nm laser excitation wavelengths with either 20x (NA = 0.4) or 100x (NA = 0.85) magnifications. The Raman system consists of a microscopy body and an attached spectrometer unit. The schematic of the setup in the back scattering configuration is shown in **Figure 3.2**. The Rayleigh rejection filters prevent the detection of the back reflected light at the incident wavelength. Only the inelastically scattered light with lower energy such as photoluminescence and Raman signals are detected by the charge coupled device

(CCD) detector. The rejection filters are hence specific to the excitation wavelength. The scattered light is focused on the diffraction grating (1200 and 2400 lines/mm) and is dispersed onto a silicon CCD for recording the Raman spectrum. The half waveplates together with the analyzer allows for the polarization-dependent measurement of the scattered light. The incident laser source, excitation power, exposure time, grating type are set through the Wire software before acquiring each spectrum.

3.5 Device fabrication

The devices were fabricated in a dedicated e-beam lithography system using a scanning electron microscope (Zeiss LEO 1530 Gemini) with Raith Elphy Plus pattern generator and CAD Elphy-32 design software. The device fabrication on the substrates with NCG and CNT film was realized in three steps. In the first step, tungsten alignment markers were defined by lithography and sputter deposition. In the case of CNT films, the surface of the as-grown CNT films is hydrophobic, and therefore, spin coating PMMA stored at room temperature resulted in very poor adhesion. On the other hand, spin coating repeatedly with cold PMMA (8 °C) improved the adhesion and resulted in a homogenous coverage. In the second step, areas of interest in the NCG/CNT film were patterned using the position of tungsten alignment markers defined in the first step. For patterning, poly(methyl methacrylate) (PMMA 950 k, 8 % in Anisol) was spin-coated to result in a 700 nm (for NCG film) and 250 nm (for CNT film) thick layer, which also acted as an etch mask (see **Table 3.1**). The exposed PMMA after e-beam patterning was developed in a solution of methyl isobutyl ketone (MIBK) and isopropanol (1:3 ratio) for 30 s at room temperature and baked on a hot plate for 60 s at 90 °C. The patterned NCG/CNT film, unprotected by the PMMA was etched using an O_2 plasma in a reactive ion etching system (Oxford Plasmalab 80 Plus) at 15 sccm O_2, 30 W, and 60 mTorr. The remaining protective PMMA layer after the etching step was removed using acetone. In the final lithography step, the electrode area was defined using e-beam patterning with conditions identical to the first and second lithography steps. The 45 nm-thick Pd/Cr metal was then sputtered as electrode material for source and drain contacts. The fabricated devices were vacuum annealed at 430 °C for 60 min to remove PMMA residues. The devices were then wire bonded onto a ceramic chip carrier for the photocurrent measurements.

Table 3.1: Device fabrication parameters of NCG and CNT films.

property/parameter	NCG films	CNT films
Doping in Si substrate	p-type	p-type
Resistivity of Si substrate	0.005 Ωcm	0.05 – 0.2 Ωcm
PMMA resist	A4.5 (25 °C)	A8.0 (8 °C)
Etch mask thickness	~ 700 nm	~ 250 nm
Etching time	4 min 15 s	1 min 45 s
Development	cold	cold
Device channel length	1 – 10 µm	1 – 10 µm
Device channel width	10 µm	10 µm

3.6 Electrical characterization

The electrical characterization of CNT and NCG film devices was conducted using an Agilent 4155C semiconductor parameter analyzer system and a probe station with TRIAX probes with a detection limit of 30 fA. The devices were characterized for the dark current-voltage and transconductance characterstics. In the transconductance measurements, the back gate (silicon as a back gate electrode) was swept between -5V and +5V with a step size of 200 mV. The NCG devices (NCG films grown on 300 nm SiO_2/Si) showed a negligible back gate dependence of the source-drain current. The I-V device characteristics of the NCG films in the dark were measured in the photocurrent set-up. A dc bias in steps of 50 mV from -0.25 V to 0.25 V was applied to the drain electrode via the Aux-out of the lock-in amplifier with the source electrode connected to the current preamplifier. The dc voltage signal from the current preamplifier was read out via the Aux-in of the lock-in amplifier. For the photocurrent measurements, the devices were wire-bonded (Universal Wedge Bonder - Model 4123) onto a ceramic chip carrier using Al - 1%Si wires. To house the chip carrier, an Aluminum box-type sample holder was prepared with 16 switches that can access the corresponding individual 16 device connections of the chip carrier. The electrical signals from and to the individual devices are transmitted through the coaxial BNC cables.

3.7 Simulations

Transfer-matrix method (TMM) simulations were conducted for s-polarized light at normal incidence using a python code available at github.com/krupke-group based on the TMM code of Steve Byrnes (arXiv:1603.02720;github.com/sbyrnes321/tmm). The theoretical basis of transfer matrix simulations is presented in **Appendix A1**. The complex refractive index of NCG was approximated by the optical constants of graphite, calculated from an analytical expression based on the dynamical conductivity of graphite.[33] The optical constants for Si and SiO_2 were taken from the refractiveindex.info database (SiO_2: Lemarchand 2013, Si: Aspnes and Studna 1983), extended with NIR data for Si from the filmetrics.de database. Finite element method (FEM) simulations of the bolometric photocurrent were performed with the commercial software package FlexPDE 6.5. A squared 2-D simulation space was confined by two Dirichlet boundaries, defining the potential difference from the applied bias voltage, and by Neumann boundaries for the two non-contacted sides. Inside the boundaries, the material was defined by its resistivity in the dark ρ_{dark} and under illumination ρ_{light}. The scanning photocurrent measurement was mimicked by defining an illuminated square with ρ_{light}, surrounded by the remaining area with ρ_{dark}. The current was simulated for each position of the illumination square within the simulation space and the bolometric current was determined by subtraction with the current without illumination. Simulations were performed for raster scans between 2x2 and 50x50 (yielding similar results), and for resistivity ratios $\rho_{\text{light}} / \rho_{\text{dark}}$ between 0.001 and 0.99. The FlexPDE script for simulating the scanning photocurrent imaging and the python code for the analysis is available at github.com/krupke-group

3.8 Photocurrent setup description

The following section describes the details of the experimental setup used in this work to measure the photocurrent from carbon nanotube films and nanocrystalline graphite. Briefly, the photocurrent experiment consisted of a broadband wavelength-tunable supercontinuum light source when used in conjunction with the lock-in technique, allowed for sensitive detection of the wavelength-dependent electrical signals. The lock-in technique is particularly useful to detect and isolate the weak photocurrent signals induced by the modulated incoming laser from the noise background and dark current in the device.

Supercontinuum light source

Acousto-optic tunable filter (AOTF) SuperK Select box

Acousto-optic tunable filter (AOTF) crystal with parabolic mirrors

NKT Photonics
SuperK EXTREME
SuperK SELECT
NKT Photonics

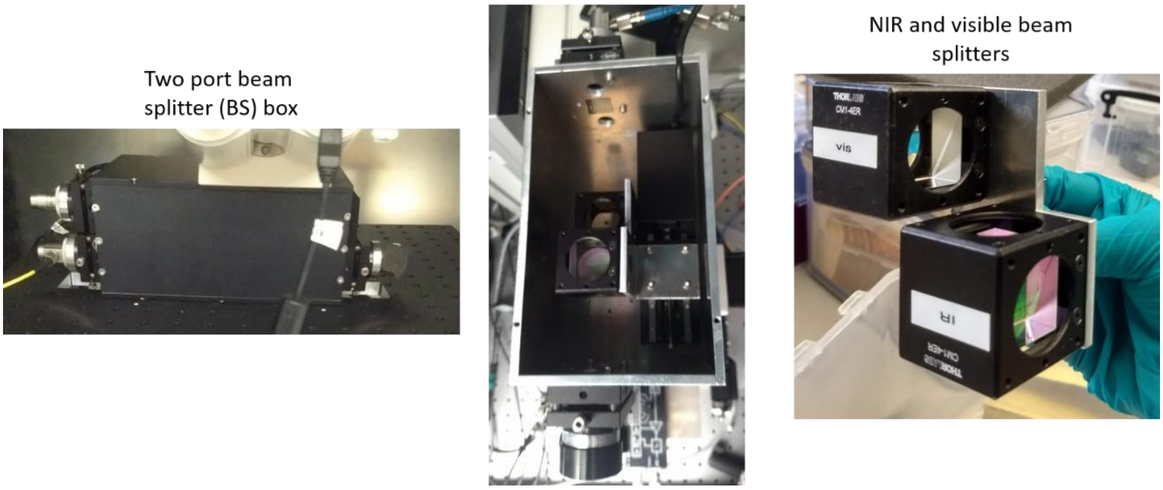
Two port beam splitter (BS) box

BS box top view

NIR and visible beam splitters

Figure 3.3: Photocurrent setup components that include supercontinuum light source, acousto-optic tunable filter, beamsplitters. AOTF photograph by P. B. Selvasundaram.

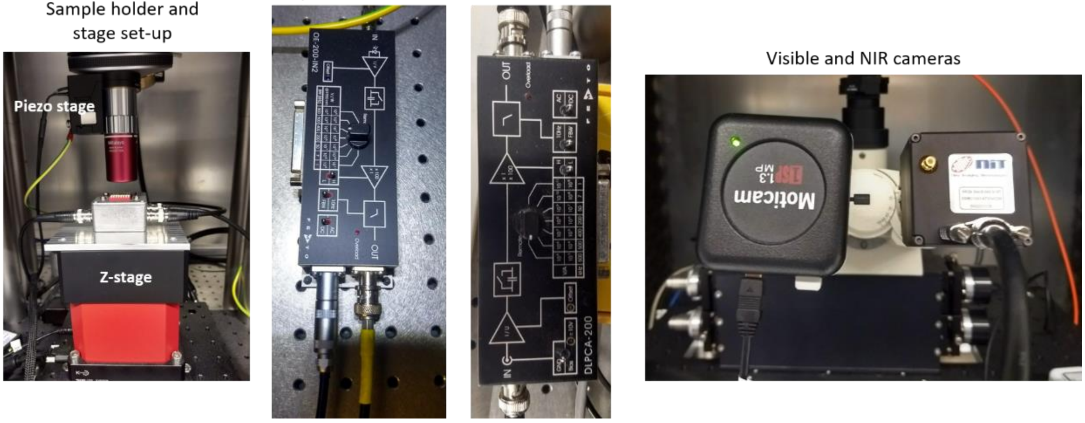

Sample holder and stage set-up

Variable gain photoreceiver

Current preamplifier

Visible and NIR cameras

Piezo stage
Z-stage
Moticam
DLPCA-200

Electronics read out and control

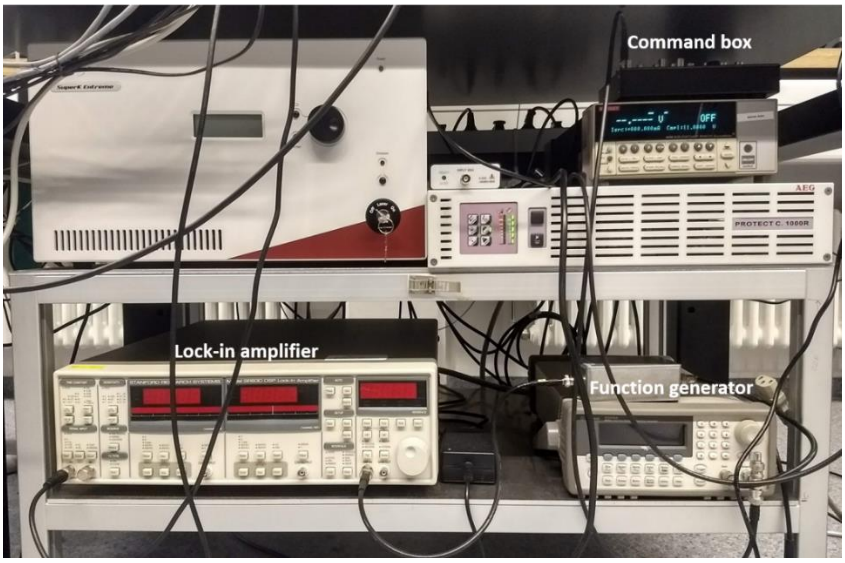

Command box
Lock-in amplifier
Function generator

Figure 3.3b: Photocurrent setup components that include, sample holder stage, cameras, and electronics for signal control and readout.

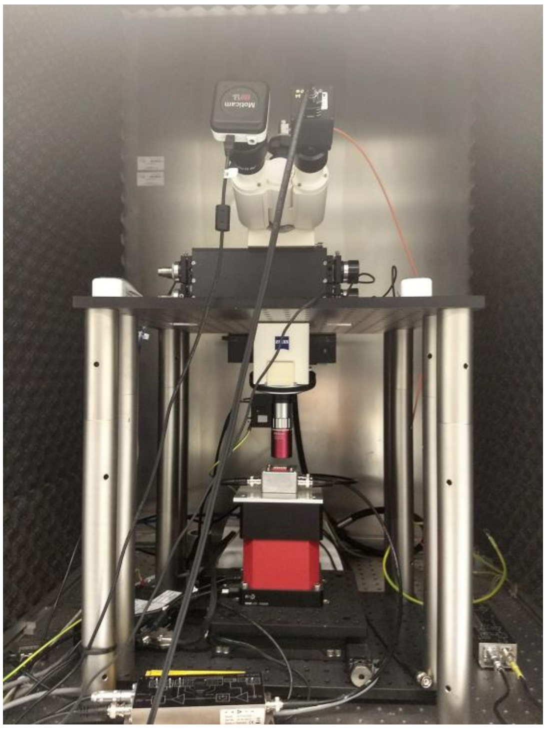

Figure 3.5: Photocurrent measurement setup

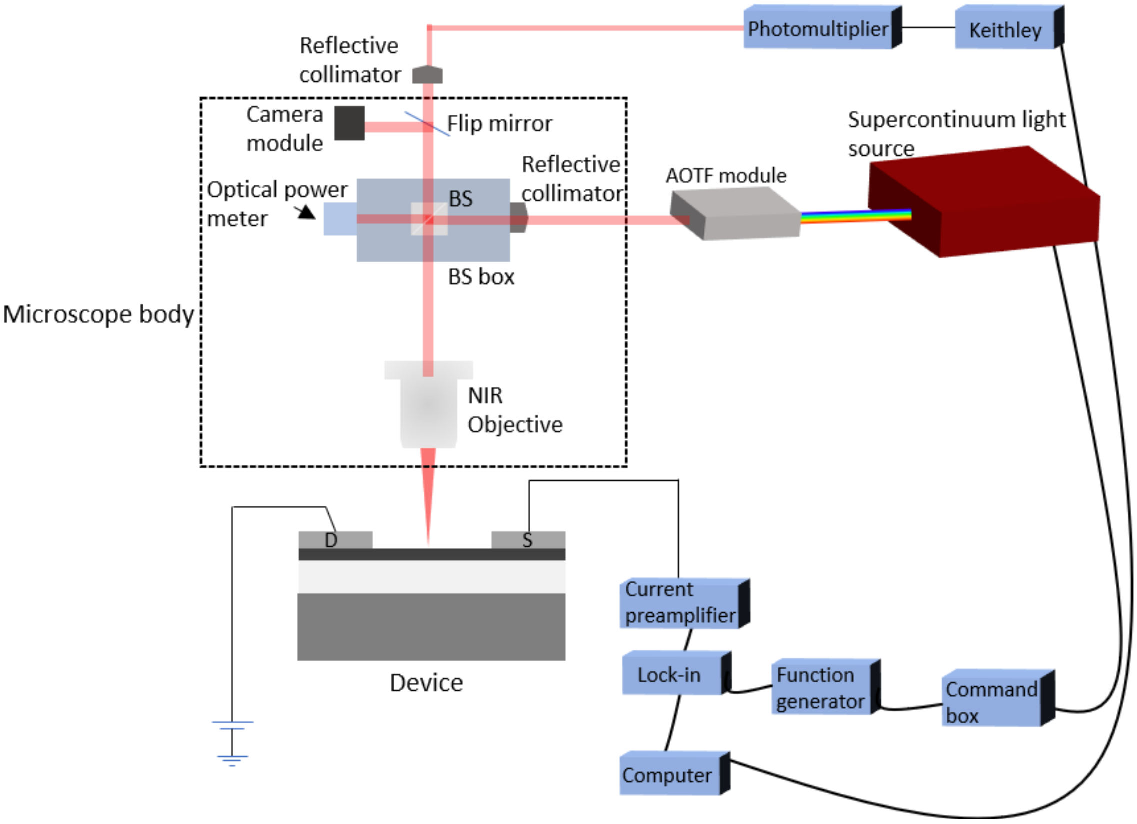
Photomultiplier
Keithley
Reflective collimator
Camera module
Flip mirror
Supercontinuum light source
Reflective collimator
AOTF module
Optical power meter
BS
BS box
Microscope body
NIR Objective
D
S
Device
Current preamplifier
Lock-in
Function generator
Command box
Computer

Figure 3.4: Schematic of the photocurrent measurement setup

Figure 3.3 shows the components of the custom-built computer-controlled photocurrent-spectroscopy (PC) and -imaging setup, consisting of an upright light microscope, motorized stages, supercontinuum (SC) laser source, lock-in amplifier, 2D SWIR camera, and NIR photoreceiver. In the following, the setup design and individual components will be first described. The PC setup **(Figure 3.4)** was concentrically designed to minimize thermal drifts that are induced due to changes in the ambient temperature. Earlier design of the photocurrent setup can be found in the Ph.D. thesis of P.B. Selvasundaram.[106] In the **Figure 3.4,** the microscope body (Axiotech varia 100) with the piezo-controlled long working distance NIR objective (Mitutoyo MPLAN APO, 0.50 NA) was rigidly mounted onto an anodized aluminum top plate supported by four low thermal expansion coefficient non-magnetic 303 stainless steel (SS) posts (diameter = 38 mm, Thorlabs). A dovetail joint (54 mm inner diameter) was used to mount the microscope body onto the top aluminum plate. The sample holder with the wire-bonded chip carrier was screwed to the motorized z-stage, and the xy-stage supporting the z-stage was mounted to the bottom anodized aluminum plate. Interior to the outer SS posts, the bottom aluminum plate was suspended by four additional SS posts from the top plate. Similar materials for the inner and outer posts minimize the thermal expansion in the z-direction.

The piezo stage (PIFOC P-712.CDQ, Physik Instrumente) was operated in a closed-loop operation with the E709 controller; the closed-loop operation compensates for any non-linearity and hysteresis in the nominal displacement in addition to the position shifts induced due to creep in the piezo ceramic for ambient temperature changes. The piezo stage has a 100 µm travel range and 0.7 nm closed-loop resolution with a ±5 nm repeatability. When the setup was not in operation, the piezo controller was left powered on but the closed-loop operation was set to OFF and the amplitude output voltage to 0V. These were the manufacturer recommended settings to avoid degradation in the lifetime of the piezo ceramic stack. The piezo stage was controlled through the PIMikroMove motion control software and the closed-loop operation was activated by setting the servo mode to ON in the software.

The servo-driven linear translation z-stage (KVS 30, Thorlabs) is controlled through the Kinesis motion control software (Thorlabs) and has a travel range of 30 mm and 0.1 µm resolution. The z-stage consists of a feedback loop (encoder) which does automatic compensation of any backlash present .The z-stage is supported by the stepper motor driven xy-stage (8MTF-102LS05, Standa) controlled via. the 8SMC5-USB-B9-2 controller. The xy- stage has a translation travel range of 102 mm in x and y directions with a full step resolution of 2.5 µm and nominally a ≈10 nm resolution in the 1/256 microstep mode. The higher repeatability (< 0.5 µm) in the linear motion was achieved by activating the backlash compensation of the xy- stage. The backlash compensation, motor acceleration, deceleration, nominal velocity, and the microstep mode were set in the motion control XILab software. The default engine settings of the 8MTF-102LS05 stage can be accessed by loading the parameter file into the software. The microscope body consists of a reflector slider (446342, Zeiss) with a 50:50 color-neutral beam splitter that is used while imaging the sample with the back illumination (CL 9000 LED, Zeiss) and is removed from the optical path during the PC measurements by moving the reflector slider.

Table 3.2: Broadband optical fiber characteristics.

Fiber model	Single mode cut-off λ /nm	Transmission	Typ. peak transmission
FD9	< 500	> 50 % (500-1300 nm)	60 % @ 900 nm
FD6-PM	1200±70	> 30 % (1200-1900 nm)	35 % @ 1700 nm

The customized two-port anodized beamsplitter housing (see **Figure 3.3**) was rigidly screwed into the anodized top aluminum plate. Two beam splitters are housed inside the BS box; 90:10 near-infrared (BS030, Thorlabs) and 90:10 visible (BS028, Thorlabs). The two beam splitters were vertically mounted onto a motorized linear translation stage (MTS50-Z8, Thorlabs) with 50 mm travel range using a custom designed anodized right-angle bracket. Either of the beam splitters can be positioned into the optical path of the objective lens by driving the translation stage to the set position. On one end of the BS box, two off-axis reflective collimators (RC02FC-P01, Thorlabs) generating a 2 mm collimated beam are mounted for the visible and NIR light coupling from the acousto-optic tunable filter (AOTF) units. The broadband optical fibers (see **Table 3.2**) used for the light coupling have a FC/PC termination and the light from the AOTF is coupled into the fiber through the SuperK CONNECT delivery system. The FD6 is a polarizing maintaining (PM) conventional step-index fiber operating with a few hundred nanometres wide transmission window. On the other hand, FD9 is an endlessly single-mode photonic crystal fiber (core diameter ≈ 10 µm). In principle, FD9 allows any wavelength, and the maximum transmission being in 500 nm – 1700 nm window. However, the chromatic effects in the collimator optics (lenses present inside the AOTF) at the fiber input act as the bottle-neck and limit the transmission range to ~ 500 nm - 1300 nm.

For in-situ monitoring of the laser power during the photocurrent measurement, two photodiode sensors for visible (PD300R, Ophir) and NIR (PD300-IR, Ophir) were mounted at the far end of the BS box in the optical path of the respective reflective collimator and beam splitter. To image the sample and the NIR laser spot, visible (Moticam 1.3MP) and Peltier cooled InGaAs NIR (WiDy Sens 640V-ST, new imaging technologies(niT)) cameras were mounted onto the microscope eyetube. Both the cameras are computer-controlled. A reflective collimator mounted onto the binocular phototube couples the reflected NIR light from the sample surface into the multimode fiber (FT200EMT, Thorlabs) connected to a variable gain femtowatt photoreceiver (OE-200-IN2, Femto).

3.8.1 Supercontinuum light source as a tunable laser

In supercontinuum generation, several non-linear effects lead to the spectral broadening of the narrow seed pulse. Since the non-linear optical effects are involved, the spectral broadening is a function of the input power of the seed pulse. The SuperK EXTREME EXW-12 (NKT photonics) is a white light laser system that generates a pulsed supercontinuum light using a seed laser pulse with 78 MHz repetition rate. The emitted spatially coherent white light beam has spectral coverage extending from 400 nm to 2400 nm. An acousto-optic tunable filter (SuperK SELECT AOTF attached to the fiber delivery system SuperK CONNECTOR) converts the supercontinuum white light source into a tunable laser source. The tunable specific wavelengths can be accessed using the SuperK CONTROL application. The details of the seed laser wavelength, pulse width before and after the AOTF can be found in the PhD thesis of P.B Selvasundaram.[106] The principle behind AOTF filtering involves that a piezoelectric transducer and absorber are bonded to an optically transparent birefringent crystal such as TeO_2. An acoustic wave is generated when the crystal is excited using an RF signal applied to the transducer. The generated acoustic wave modulates the refractive index of the birefringent crystal and creates a phase grating. When the period of the phase grating matches that of the incident light wavelength, then that particular wavelength is diffracted into the first order while the other wavelengths pass through (zeroth order) into the beam dump. The frequency and the amplitude of the acoustic wave dictate the wavelength and intensity of the diffracted light. Hence, as we will see below, the applied RF power is a critical factor influencing the intensity of the central peak in the diffracted wavelength. Each SuperK SELECT module can accommodate up to two AOTF crystals, and with the combination of suitable beamsplitters, spectral coverage extending from visible to NIR can be achieved. The following are the accessible wavelength ranges from the three AOTF crystals in the two SELECT units, visible (500 nm – 825 nm), NIR1 (825 nm – 1400 nm), and NIR2 regime (1100 nm to 2100 nm).

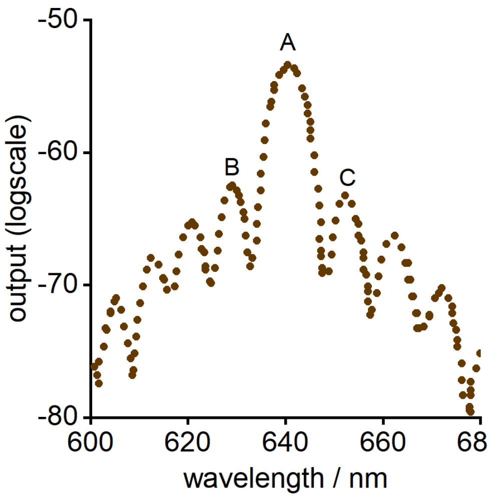

Figure 3.6: Output spectrum from AOTF when tuned to 640 nm (from SuperK SELECT manual, NKT)

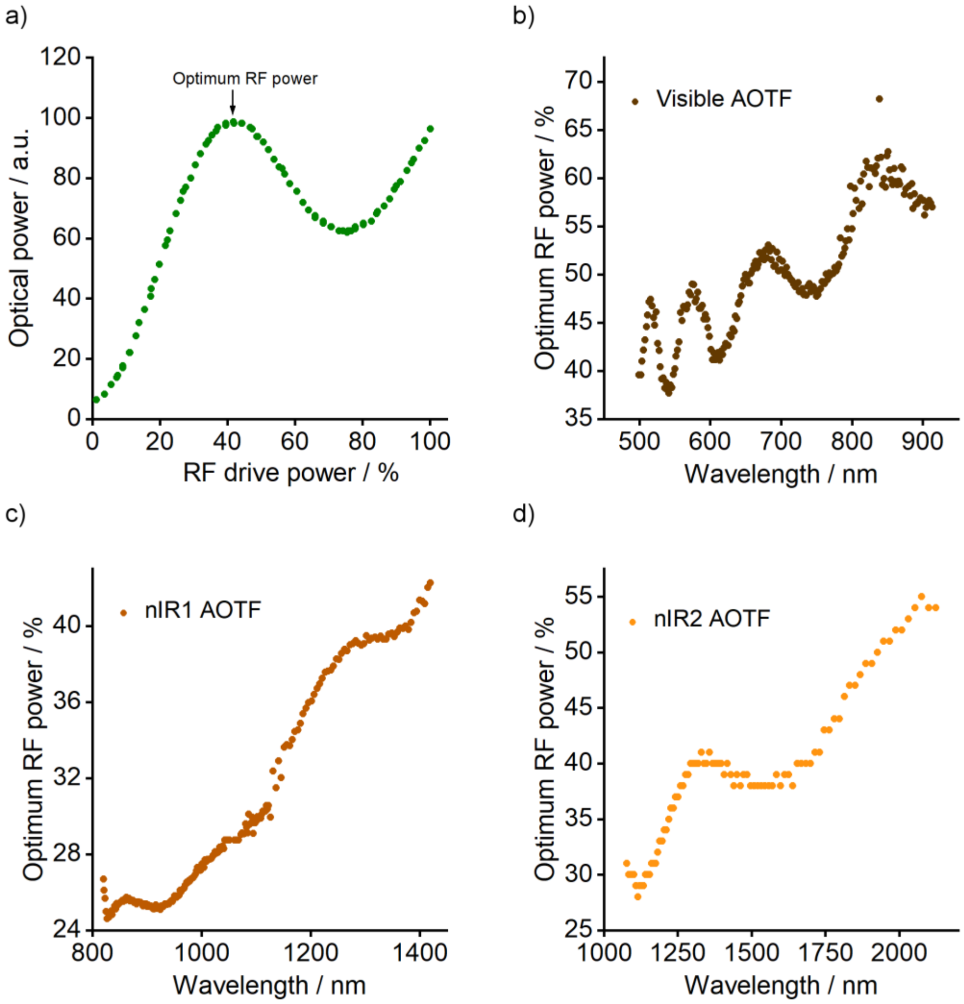

Figure 3.7: Output spectrum from AOTF when tuned to 640 nm (adapted from SuperK SELECT manual, NKT) (b) Visible (c) NIR1 (d) NIR2. Measurement data in (b), (c) and (d) are factory-calibrated.

The **Figure 3.6** shows the output spectrum in logarithmic scale when the AOTF is tuned to the central wavelength in this instance to 640 nm. The central peak is denoted as A and the stronger side lobes on either side of the central peak are denoted as B and C. The power in the side lobes decreases as one moves away from the central peak. The power in the central peak can be controlled using the two RF power configuration modes in the SuperK SELECT: “Normal” mode and “Overdrive” mode. In the “Normal” mode, the power in the central peak increases with increasing RF power. In the “Overdrive” mode, the central peak increases until a certain RF power level is reached. Beyond that, increasing RF power will only increase the side lobe power, and the power in the central peak decreases. As the side lobe power is relatively higher in the “Overdrive” mode, the fiber coupling is less efficient. On the other hand, the “Normal” mode ensures the optimal output power of the central peak for efficient fiber coupling. **Figure 3.7a** shows the coupled output power into the fiber as a function of RF power at a specific wavelength. The optimum RF is defined as the power where the coupling into the fiber is maximum. The procedure to obtain optimum RF power is repeated for each wavelength similarly. **Figure 3.7b-d** show the factory-calibrated optimum RF power for the entire spectral range (500 nm to 2100 nm) for the visible and NIR AOTF crystals. All the photocurrent measurements in this thesis were conducted in the “Normal” RF mode.

3.8.2 Shaping of the near-IR source spectrum

The SC spectrum measured after the AOTF is strongly wavelength-dependent with many fine structures (**Figure 3.8a**, black symbols). To minimize the impact of the wavelength-dependent intensity variations on the calculation of the NIR photocurrent responsivity spectrum, the source spectrum has been smoothened by applying wavelength-specific intensity modification to the acousto-optic tunable filter (AOTF). The targeted smooth spectrum is shown in **Figure 3.8a** as a red line and has been defined as a parabolic curve, fitted to the SC spectrum at 1150 nm, 1400 nm, and 2100 nm. The optical power delivered by the AOTF at a selected wavelength depends on the optimum RF power applied to the AOTF crystal. Adjusting the optimum RF power for each wavelength allows therefore to shape the spectrum. To convert the raw SC spectrum to the targeted smooth spectrum the following sequence has been used. The first set of optimum RF values was obtained by normalizing the fitted parabolic power spectrum with the broadband SC spectrum. With the resulting RF values, a second power spectrum was recorded. The parabolic fit was further normalized with the obtained spectrum to result in the second set of RF values and the process was iteratively repeated until the resulting power spectrum had a smooth dependence **(Figure 3.8b)**. The Origin 2019 software was used for the calculation of the optimized RF values.

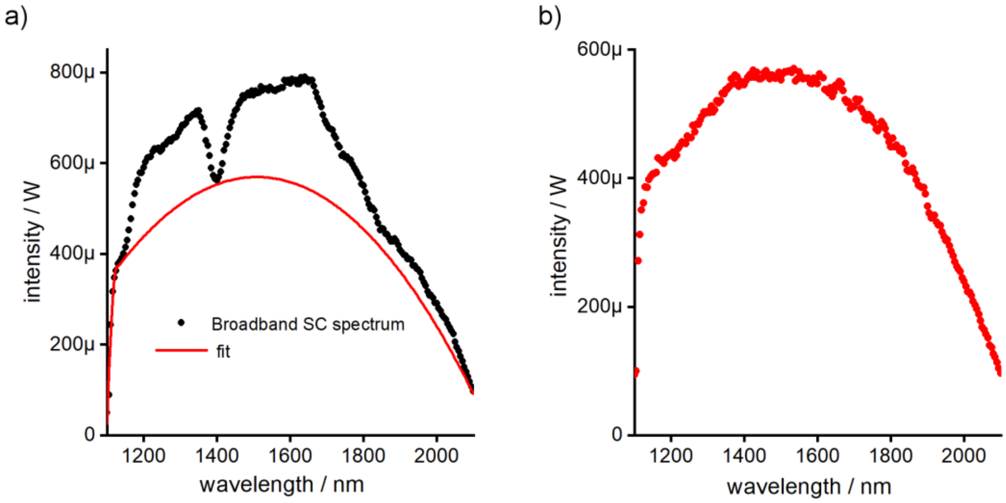

Figure 3.8: Converting the supercontinuum (SC) spectrum to a smooth power spectrum by a wavelength-specific intensity adjustment to the acousto-optic tunable filter (AOTF). (a) The raw SC spectrum is shown in black and targeted smooth spectrum is shown in red. (b) Obtained smooth spectrum after the intensity adjustment.

The source spectrum was recorded under the objective using a calibrated pyroelectric sensor (RM9, Ophir) with amplitude-modulated incident light at 18Hz. The RM9 sensor is sensitive to 18Hz frequency and has a response time of 3.5 seconds. The time step between each data point was 6 seconds. The amplitude modulation of the incident light is applied by the function generator (Agilent 33210A) to the AOTF through the SuperK COMMAND interface box. The maximum modulation frequency range of the AOTF is 50-100 kHz. A custom python program was used to record the intensity spectrum of the source. The power at the 10% side output was recorded using the PD300R/PD 300IR detectors with the incident light modulated at 1 kHz (or the frequent used for the photocurrent experiment).

3.8.3 Scanning photocurrent current measurement technique

The scanning photocurrent spectroscopy technique involves scanning a focused laser beam over the device area and measuring the resulting photocurrent (or photovoltage) as a function of the position of the laser spot. The photocurrent spatial maps can provide information on the optoelectronic properties of the photoresponsive material. For instance, the regions of maximum photoresponse can give insights into the dominant mechanism responsible for photocurrent generation. Examples of this include identifying the regions of maximum electric field in the device from the bolometric photocurrent mapping, detection of the variations in Seebeck coefficients across the photoactive material when the mechanism is photothermoelectric.

The photocurrent experiments reported in this thesis were performed using the setup shown in **Figure 3.4**. Before the PC measurements, the setup was optically aligned in the following way: A red laser was coupled into the setup from below the objective, the laser beam travels through the optical path of the setup and exits at the "side input" of the beamsplitter housing (BS box). The laser beam exiting the side input was centered by fine adjustment to the spatial position of the beamsplitter. After this alignment step, the NIR laser beam from the AOTF was coupled into the setup using a reflective collimator screwed to the BS box. Once the NIR beam is coupled, the fine adjustment to minimize the off-axis illumination was implemented in the following way: At a chosen NIR wavelength (say 1100 nm), the beam was focused on a reflecting surface and was imaged using the infrared camera. While defocusing, the laser spot must not move along diagonally, but rather move in and out of the sample plane. The diagonal movement arises due to the off-axis illumination and can be minimized by carefully adjusting the alignment screws at the reflective collimator input (BS box). This procedure was repeated for two different NIR wavelengths. Next, the fine adjustment in the steps of 0.5 mm to the beamsplitter position was implemented at different wavelengths to further center the NIR beam to the optic axis of the setup to ensure the lateral shift of beam on the sample in the x and y directions is minimized.

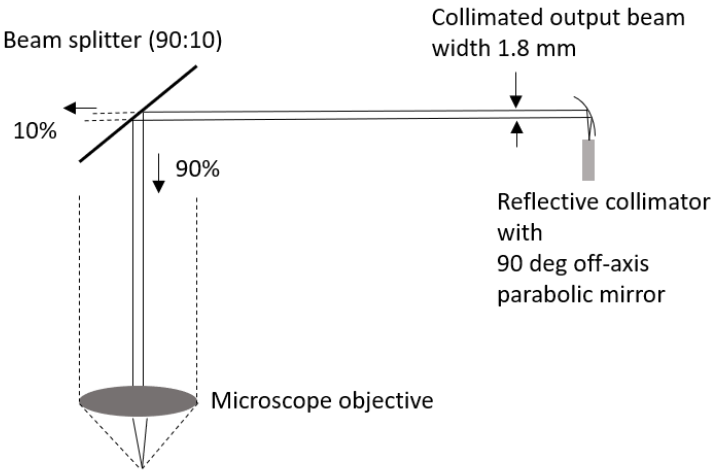
Beam splitter (90:10)
Collimated output beam width 1.8 mm
10%
90%
Reflective collimator with 90 deg off-axis parabolic mirror
Microscope objective

Figure 3.9: Optical beam path of the NIR beam after exiting the reflective collimator and into the microscope objective through the 90:10 beam splitter.

Now we discuss the chromatic aberration correction of the setup. Although a near-infrared objective is used, the setup exhibits significant chromatic aberration, resulting in an axial focus shift of 60 µm over the entire wavelength range, as shown in the wavelength dependent axial focus shift in **Figure 3.10**. The chromatic aberration correction made it necessary to perform the hyperspectral photocurrent imaging by sequentially scanning an area for each wavelength instead of scanning the wavelength at each position. Thus, the focus had to be adjusted for each wavelength to ensure diffraction-limited photocurrent imaging at every wavelength. To image the laser spot size, the 2D SWIR camera which is sensitive up to 1800 nm was used. Beyond 1800 nm, the chromatic focus shift was obtained by extrapolation. The calculated chromatic shift for the NIR objective was provided by Mitutoyo (**Table 3.3**).

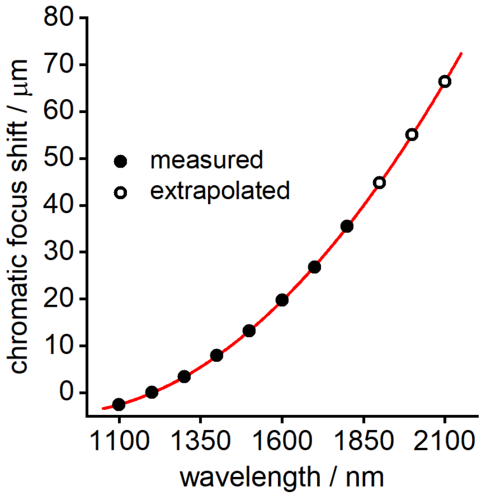

Figure 3.10: Measured axial chromatic shift of the 100x NIR objective. The data points in the open circles indicated are the extrapolated values.

Table 3.3: Calculated data for the axial chromatic shift of the 100x NIR objective used. The data from 1200 nm to 1800 nm with the reference wavelength as 587.5 nm was provided by Mitutoyo corp. The extrapolated values are indicated in bold.

Wavelength / nm	Chromatic focus shift / µm
587.5	0
1100	-0.85
1200	1.5
1300	4.9
1400	9.6
1500	15.3
1600	22.3
1700	30.3
1800	39.4
1900	**49.3**
2000	**60.1**
2100	**71.4**

The photocurrent maps were recorded in the NIR/SWIR spectral range from 1100 nm to 2100 nm using the supercontinuum white light source in combination with the acousto-optic tunable filter (SuperK SELECT-NIR2 AOTF attached to SuperK CONNECT with FD6-PM fiber) converts the supercontinuum white light source into a tunable NIR laser source as described earlier. The excitation laser line from the AOTF was then coupled into a reflective collimator (Thorlabs RC02FC-P01), and 90 % of the collimated light was guided through the 90:10 beam splitter (Thorlabs BS030) into the customized Zeiss Axiotech Vario microscope with NIR objective. The laser source intensity was continuously monitored during the photocurrent scan using the NIR photodiode sensor (PD300R-IR, Ophir) attached at the 10 % exit port. The photocurrent maps were recorded in 100 nm wavelength steps. The diffraction-limited laser spot was focused onto the sample using the infinity-corrected 100x NIR (Mitutoyo MPLAN APO, 0.50 NA) long working distance objective, and the laser spot was positioned across the scan area with the stepper motor-controlled X-Y translation stage in 1 µm steps. The laser spot reflected from the sample surface was imaged using the Peltier cooled InGaAs camera. The fine adjustment of the focus was precisely controlled using the piezo objective scanner. The chromatic aberration-induced shift of the axial focus of the NIR objectives was compensated for each wavelength before taking a photocurrent map.

A wavelength-specific intensity adjustment to the AOTF was implemented to obtain a smooth, intensity-calibrated source spectrum (**Figure 3.8**). The photocurrent of the NCG films was measured using the lock-in technique at room temperature. The incident light was modulated at 1214 Hz via the AOTF SuperK COMMAND interface box. The frequency was selected in a low noise region remote from multiple power line signals analyzed by a spectrum analyzer (Signal Hound USB-SA44B) at the lock-in monitor output. The modulated photocurrent was converted into a voltage signal using a low-noise current-preamplifier (DLPCA-200, Femto) and fed into the lock-in amplifier (SR830 Lock-in Amplifier, Stanford Research Systems) referenced to the modulation frequency. The photocurrent amplitude and phase were subsequently recovered from the lock-in amplifier. For the biased photocurrent measurements, a source-drain bias was applied via the auxiliary output of the lock-in. In sync with the photocurrent mapping, the back-reflected light from the sample was simultaneously recorded to map out the device area using an InGaAs photoreceiver (OE-200-IN2, Femto) connected to the source meter (Keithley 6430). The photocurrent and reflectance mapping were automated and controlled by a python code.

In the wiring scheme for the photocurrent measurements, the bias was applied to the drain electrode and the source electrode is connected to the current preamplifier. For the measurements in the short-circuit condition, the drain electrode was terminated with a 50 Ω resistor. The total time required to record a 20 µm x 20 µm area map per wavelength was 60 min and the entire hyperspectral imaging took about 12 hours. On average, the time required to record a photocurrent pixel was about ~9 seconds. This includes a signal stabilization time of 5 times the lock-in integration time (1 s), time for data acquisition, plotting and, backlash corrections to the xy-stage.

A few additional tests were carried out to determine any phase shifts induced due to the different setup components. (a) the phase shift due to AOTF modulation: reflected light from the metal electrode was coupled into the photoreceiver, and the output of the photoreceiver was connected to the lock-in input. (b) phase shift due to the current preamplifier: Here, the current preamplifier was replaced with a 1 MOhm resistor. The function generator output (5 mV peak-to-peak, 100 µV offset, 1214 Hz) was connected to the 1 MOhm resistor, and the output from the resistor was connected to the lock-in input. In both the cases, the measured phase shifts at the lock-in amplifier were less than 1.5°.

3.8.4 Noise measurement

Dark noise current (I_{noise}) from the NCG device was measured in the PC setup with the SR830 lock-in amplifier. Aux-out from the lock-in amplifier was used as a DC voltage source to bias the device, and the low-noise current amplifier to amplify the current. The output of the current amplifier was directly fed to the signal input of the lock-in amplifier for the noise measurements, where the internal reference frequency was set manually to the frequency that was used for the PC measurements.

Table 3.4: Frequency bandwidth and waiting time for different filter slopes (from SRS830 manual)

Filter slope	ENBW	Wait time
6 dB/oct	1/(4T)	5T
12 dB/oct	1/(8T)	7T
18 dB/oct	3/(32T)	9T
24 dB/oct	5/(64T)	10T

The frequency bandwidth determines the amount of the measured noise signal and is limited by the equivalent noise bandwidth (ENBW) of the low pass filter. The ENBW is dependent on the filter slope and time constant T (see **Table 3.4**). The measured noise from the lock-in is given in the units A/Hz$^{1/2}$ factoring into the account the ENBW of the selected time constant.

Chapter 4 NIR Photodetection with Nanocrystalline Graphite

Graphene, a zero-gap semiconductor, absorbs 2.3 % of incident photons in a wide wavelength range as a free-standing monolayer, whereas 50 % are expected for ~90 layers. Adjusting the layer number allows tailoring the photoresponse, however, controlling the thickness of multilayer graphene remains challenging on the wafer scale. Nanocrystalline graphene or graphite (NCG) can instead be grown with controlled thickness. In this chapter, photodetectors from NCG were fabricated that are spectrally flat in the near- to short-wavelength infrared by tailoring the layer thicknesses. Transfer matrix simulations were used to determine the NCG thickness for maximum light absorption in the NCG layer on a silicon substrate. The extrinsic and intrinsic photoresponse was determined from 1100 to 2100 nm by chromatic aberration corrected photocurrent spectroscopy. Diffraction-limited hyperspectral photocurrent imaging shows that the biased photoresponse is unipolar and homogeneous across the device area whereas the short-circuit photoresponse gives rise to positive and negative photocurrent at the electrodes. The intrinsic photoresponses are wavelength-independent, indicative of bolometric and electrothermal photodetection.

Contribution: I have fabricated the NCG devices, characterized the films, performed scanning photocurrent measurements, and simulated the absorptance of the Pd/NCG-SiO_2/Si stack.

This chapter is based on:

- N. A. Peyyety, S. Kumar, M-K. Li, S. Dehm, and R. Krupke. *Tailoring Spectrally Flat Infrared Photodetection with Thickness-Controlled Nanocrystalline Graphite.* ACS Appl. Mater. Interfaces 2022, 14, 7, 9525-9534

Introduction

Photodetection in the near-infrared to short-wavelength infrared electromagnetic spectrum has become very important for a wide range of applications in telecommunications, biomedical imaging, food inspection, night vision, environmental monitoring, and astronomy. Photodetectors used in this spectral range are commonly based on semiconductors like HgCdTe, InGaAs, and Si,[107] where the material's band-gap defines the spectral sensitivity. The more recently developed photosensitive semiconducting materials,[108] like metal dichalcogenides,[109–112] titanium oxide-organic layers,[113] black phosphorous,[114] or perovskites[115,116] have a similar operating principle. On the other hand, graphene is a photosensitive semimetal and an ideal wavelength-independent photoabsorber for the visible- to infrared wavelength range due to its linear band structure and the absence of a gap.[27] It is commercially available and CMOS-compatible, and wired into a transistor configuration, graphene gives rise to photovoltaic, electrothermal, or bolometric photocurrents, depending on the operating conditions.[117–119] The bolometric photoresponse under voltage bias has the advantage that the entire graphene channel becomes photosensitive and responsivities comparable to p-n junctions have been demonstrated with visible light ($2.5\text{x}10^{-4}$ A/W at 1 V bias and 690 nm).[119]

Photodetection with single-layer graphene is limited by the low intrinsic light absorption of 2.3 %, and can only be enhanced by integrating graphene into optical cavities, and plasmonic or photonic structures,[120–123] or combining with quantum dots,[124–128] or layered materials from the transition metal dichalcogenide family.[15,129] However, using optically engineered structures and materials with wavelength-dependent light absorption inevitably induce a wavelength dependence in the responsivity,[122,130,131] which is not an obstacle unless spectral flatness is beneficial. In principle, the intrinsically flat optical broadband absorption of graphene could be improved simply by using several layers, and recently, the optical absorption was calculated for multilayer graphene taking into account the reflectance of each layer.[32] (See also **Chapter 2, section 2.1** for a more detailed discussion on the absorptance in multilayer graphene). Interestingly, almost wavelength-independent light absorption of 50 % was projected for graphite with 87 graphene layers, which promises an improvement in responsivity by an order of magnitude when used as a photodetector material. Unfortunately, it remains challenging to grow multilayer graphene with a predefined thickness. On the other hand, nanocrystalline graphene or graphite can be grown directly on dielectric surfaces with a controllable thickness by graphitization of polymeric films,[37,61,132] and have been employed as transparent electrodes for graphene glass and silicon-based Schottky photodetectors.[36,133] Therefore, increasing the responsivity while keeping a spectrally-flat responsivity seems possible with thickness-tailored NCG. Previously, bolometric near-infrared photodetection with a 4 nm thin NCG layer has been demonstrated.[37] However, due to the non-optimized layer structure, the responsivity of the thin NCG layer was merely 1.7×10^{-6} A/W at 1 V bias and 1065 nm.

In this chapter, the near infrared photoresponse with NCG on a SiO_2/Si substrate is reported by tailoring the thickness of NCG and SiO_2. In the targeted near- to short-wavelength infrared, the responsivity exceeded the previous thin layer result by more than two orders of magnitude. First, the optimum SiO_2 and NCG thickness that is required for maximizing the optical absorption in NCG between 1100 nm and 2100 nm wavelength was computed through transfer matrix simulations. The synthesis conditions to obtain the targeted NCG thicknesses is then described. The synthesized films were characterized using Raman spectroscopy to confirm the hybridization and domain size. Devices with source and drain electrodes were fabricated on the optimized NCG/SiO_2/Si layer structure and were electrically characterized for the current-voltage characteristics. The scanning photocurrent measurements were conducted with an intensity-calibrated, chromatic-aberration corrected setup under short-circuit and voltage-bias conditions using a lock-in technique to spectrally and spatially resolve photocurrents. The extrinsic and intrinsic responsivities were determined and analyzed in terms of the photodetection mechanism. In the end, a compilation of performance figures of 2D infrared detectors is presented.

4.1 NCG thickness optimization and transfer matrix simulation

The optimum thickness of the NCG layer and SiO_2 layers on Si was determined by transfer-matrix method (TMM) simulations to maximize the NIR to SWIR light absorption through the NCG layer. The calculations were performed with s-polarized light under normal incidence in the 400 to 2100 nm wavelength range. The NCG and SiO_2 layer thicknesses were varied from 5 to 100 nm and 50 to 1000 nm, respectively, and the refractive index of the NCG layer was approximated by the wavelength-dependent refractive index of graphite.[32] (For TMM simulation details see **Chapter 3**).

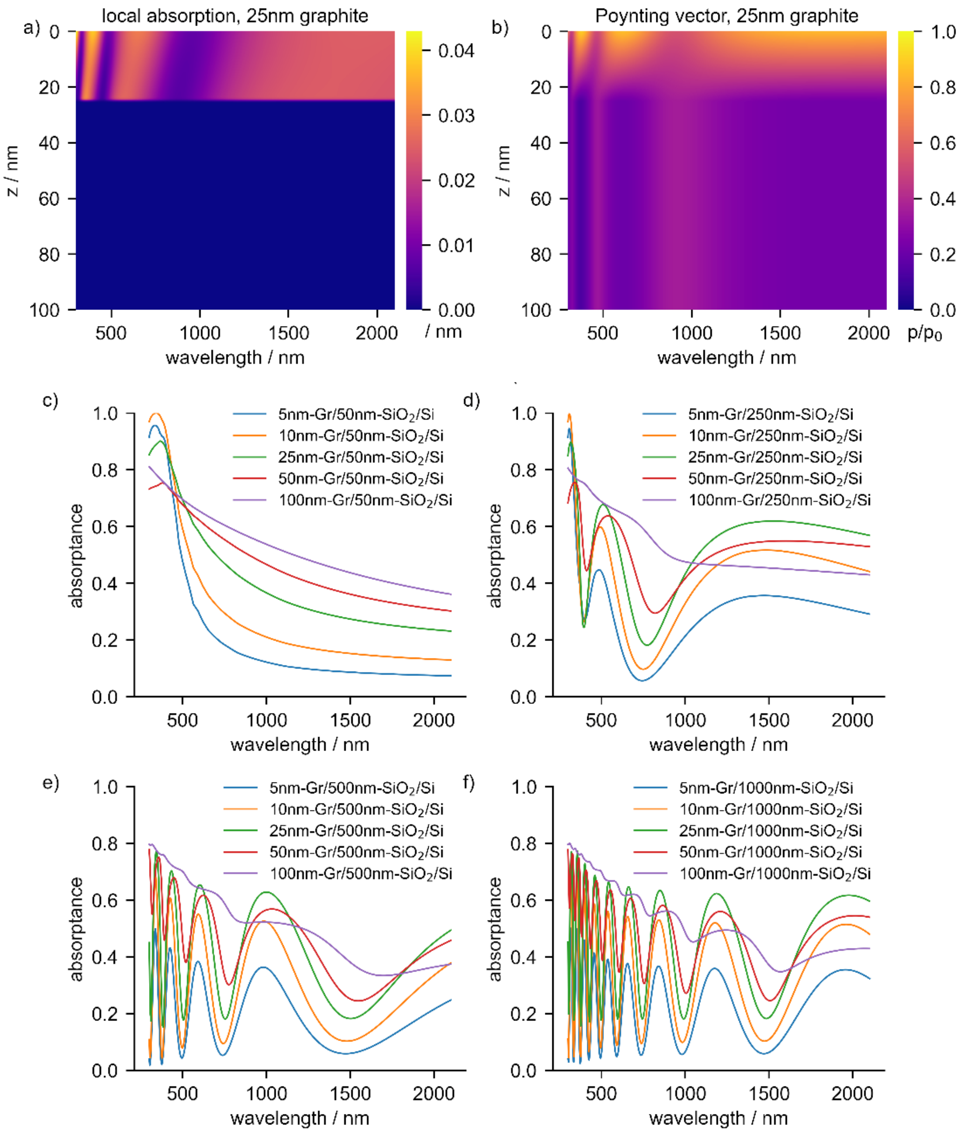

Figure 4.1: Transfer matrix simulation of (a) the local absorption and (b) Poynting vector in a 25nm graphite/300nm-SiO2/Si multilayer. The z-axis points along the surface normal into the substrate; the origin is at the graphite-air interface. (c-f) Calculated total absorptance in the graphite layer for different graphite and SiO_2 layer thicknesses. Simulated with s-polarized light under normal incidence.

Figure 4.1a and **Figure 4.1b** show the local light absorption and the Poynting vector - the directional energy flux - in the upper 100 nm of a 25nm graphite/300nm-SiO_2/Si layer structure. As expected, the local light absorption in the graphite layer is strongly dependent on wavelength and depth and, in turn, depends on the thickness of the graphite and SiO_2 layers. Relevant for photodetection is the integrated local light absorption in the graphite layer, the absorptance, which is shown for a wide range of parameters in **Figures 4.1c-f**. For a given oxide thickness, the fraction of light absorbed in graphite first increases with its thickness and then decreases as the reflectance from the graphite layer increases. In addition, the multilayer interference induces wavelength oscillations which become more prominent for oxide layers thicker than 250 nm. As a result, for the targeted broad wavelength range from 1100 to 2100 nm, it was found that the absorptance in graphite is maximized for 25 nm thick graphite on top of a Si substrate with a 250 nm thick SiO_2 layer (green curve in **Figure 4.1d**). The devices were fabricated using 300 nm thick SiO_2 instead of 250 nm, because of commercial availability and the almost identical simulation results. We note, that the optimized graphite thickness of 25 nm is close to the thickness that corresponds to the universal layer number $N = (2/\pi\alpha) = 87$ in graphite at an interlayer distance $d = 0.335$ nm. For values larger than $N \cdot d \approx 29$ nm, the reflectance of graphite becomes significant and its absorptance wavelength dependent. (See discussion also in **Chapter 2**)

4.2 Synthesis of thickness optimized NCG films

Nanocrystalline graphite was grown on 300 nm-SiO_2/Si substrates by graphitization of a spin-casted photoresist.[37] The photoresist solutions were prepared by diluting an S1805 photoresist in propylene glycol monomethyl ether acetate (PGMEA).

Table 4.1: Spin coating conditions and the resulting NCG thickness.

Dilution ratio	Spincoating speed/rpm	Thickness/nm
1:1	2000 rpm	42 ± 3
1:1	4000 rpm	24 ± 0.5
1:4	4000 rpm	11

The NCG thickness optimization study was carried out by adjusting the S1805: PGMEA dilution ratio and the spin coating conditions (rotation speed). After graphitization at 1000℃ for 10 hours under high vacuum, the NCG thickness was confirmed by atomic force microscopy (AFM). Devices fabricated from NCG layers with 11 nm and 24 nm thicknesses were used for the photocurrent measurements. **Table 4.1** summarizes the spin coating parameters used, and the resulting thicknesses obtained after graphitization.

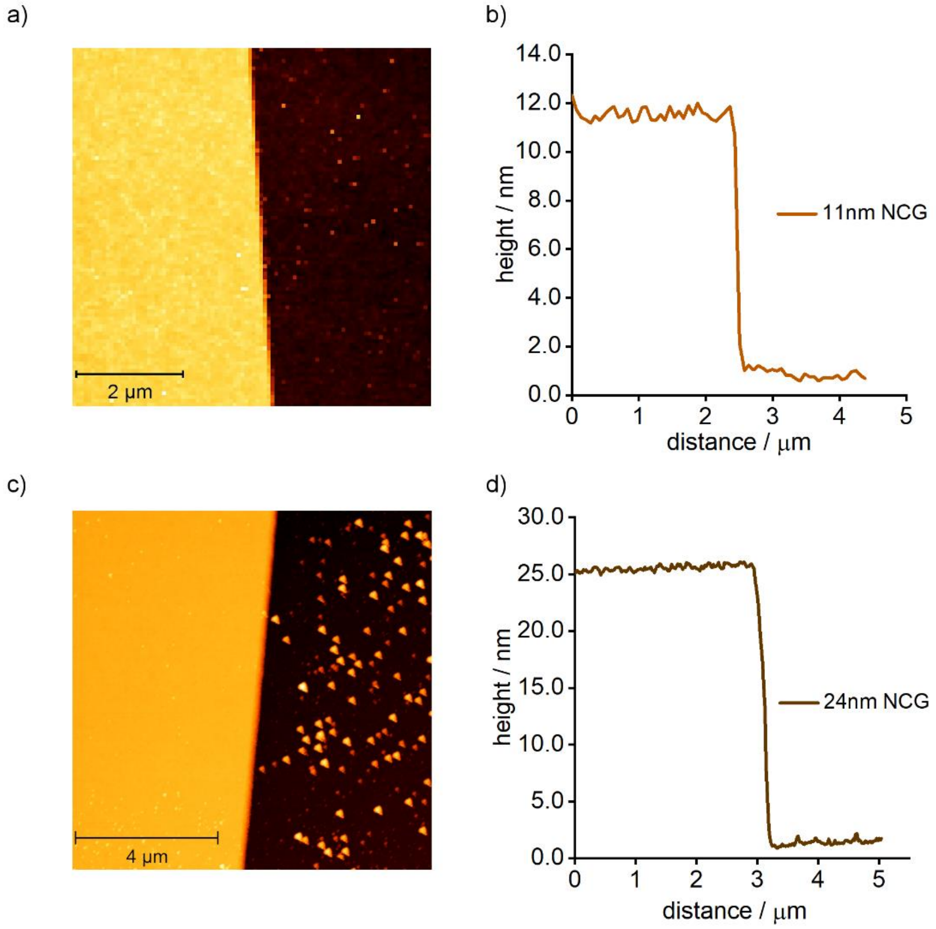

Figure 4.2: (a) and (c) AFM images of the 11 nm and 24 nm NCG films and their respective line-cuts in (b) and (d).

It should be pointed out the duration of the plasma cleaning step before spin coating influenced the final roughness of the synthesized NCG film. As the resist coats the SiO_2 surface conformally, the final NCG roughness is similar to the surface roughness of SiO_2. An optimized plasma cleaning step with a duration of 30 s was implemented, resulting in films with roughness below 1 nm.

4.3 Raman spectroscopy of NCG films

The synthesized NCG films were measured by Raman spectroscopy. Raman spectra of the NCG films show broad D-, G- and 2D-mode peaks, characteristic of nanocrystalline graphite (**Figure 4.3a**). The Raman spectra of the NCG films were analyzed to confirm the degree of sp^2-hybridization and to determine the average crystallite size, similar to the previous report where the optimum graphitization conditions from Raman and X-ray photoelectron spectroscopy was determined.[37]

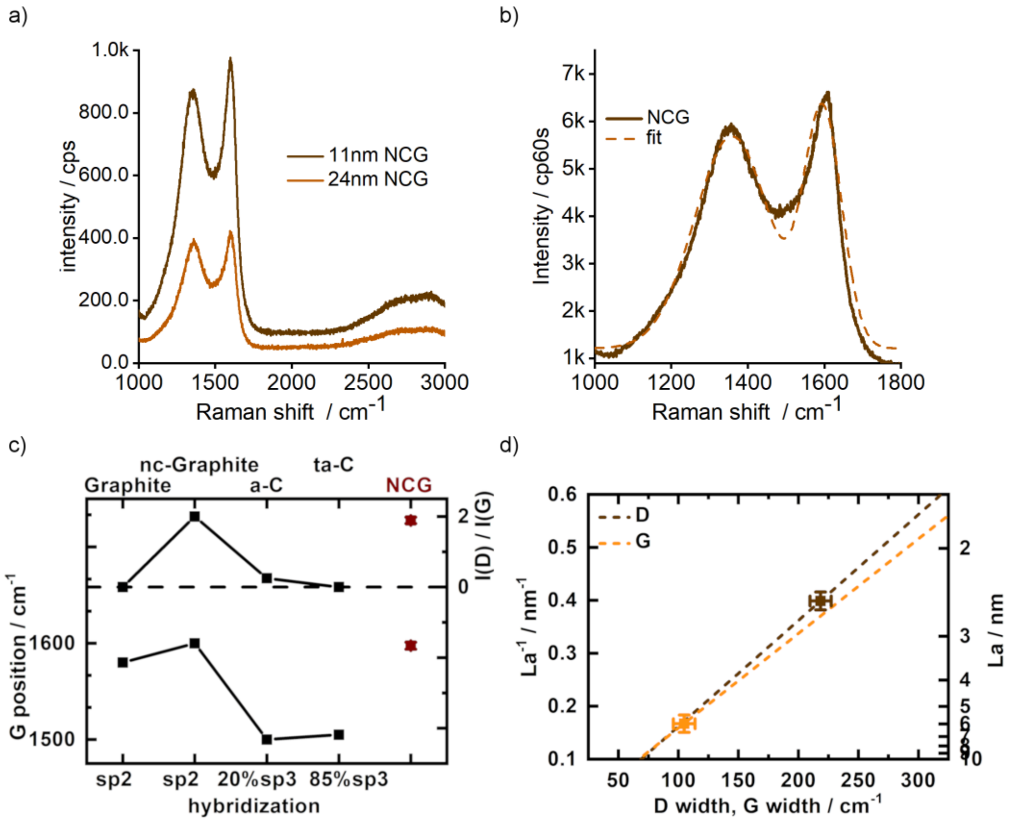

Figure 4.3: (a) Raman spectra of NCG/300 nm-SiO2/Si with 11 and 24 nm NCG thicknesses. (b) NCG Raman spectra fitted to Gaussian peaks for obtaining the D- and G- line widths. Shown is the overall fit. (c) Raman G-peak position and intensity ratio of D-peak and G-peak for NCG compared with data from Ferrari et al.[50] for graphite, nanocrystalline (nc) graphite, and two forms of DLC. The sp-hybridization is indicated. (d) Crystallite size La in NCG determined from the FWHM of the D- and G-peaks. The dashed lines are extrapolated correlations based on Cancado et al. [56,57]

The spectra were fitted to the Gaussian peaks centered near 1350 cm^{-1} and 1595 cm^{-1} to extract the D- and G-mode line widths corresponding to the Fullwidth-at-the-half maximum (FWHM); the overall fit is shown in **Figure 4.3b**. The G- and D-mode intensities were computed from the areas under the respective Gaussian peaks. Next, the G-peak position and the ratio of the D-mode and G-mode intensities have been fitted to the hybridization trajectory of Robertson and Ferrari[53] **(Figure 4.3c**), showing that the NCG films are fully graphitized (100% sp^2-hybridization).[37] The amorphization trajectory proposed by Robertson and Ferrari is discussed in **chapter 2** (section 2.2). The crystallite size in the NCG films was determined from the width of the D-peak to 2-3 nm and a corresponding statistical evaluation of the crystallite size is given in **Figure 4.3d**, which is similar to the previously reported Raman and electron diffraction analyses of the NCG films prepared under similar conditions.[37,134,135] Since the thickness of the synthesized graphitic films is larger than the crystallite size, the films in this work are referred to as nanocrystalline graphite.

It should be noted that the intensity of the Raman peaks is lower for the thicker film because of optical interference in the multilayer structure and reabsorption of the scattered light emanating from the lower part of the NCG layer by the upper part of the NCG layer. The Raman intensity of multilayer graphene on SiO_2/Si depends not only on the thickness of the graphitic layer and the oxide layer, but also on the laser excitation wavelength and on the numerical aperture of the objective.[136] Complementary to Raman spectroscopy, the hybridization and the thickness information of the NCG films can also be obtained from X-ray photoelectron spectroscopy (XPS).[37] NCG films show the characteristic C 1s core level signal with the main peak at 284.4 eV, observed also in graphite and corresponds to the sp^2 hybridization in carbon atoms. Further, using the attenuated SiO_2 (Si 2p attenuation) substrate signal due to the NCG layer, the thickness of NCG can be estimated.

4.4 Device fabrication and electrical characterization

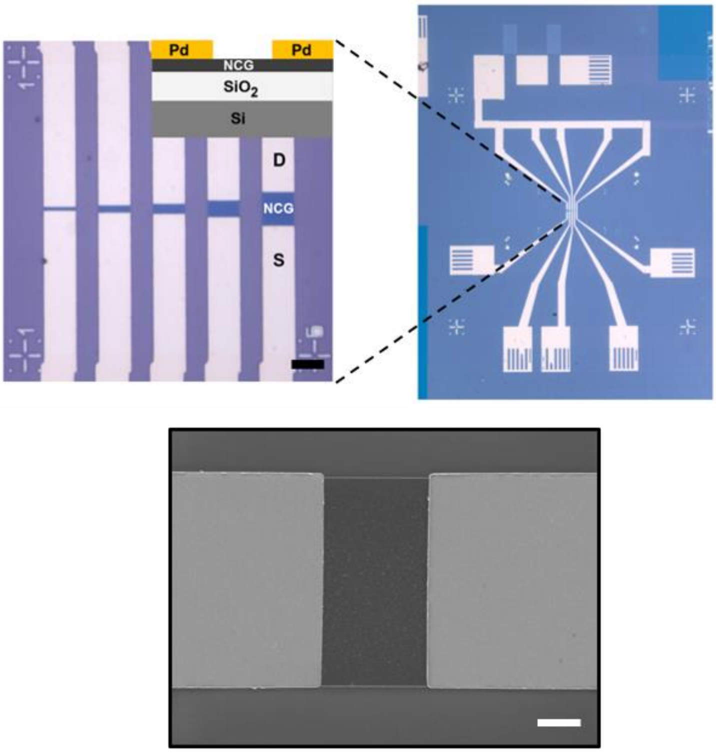

Figure 4.4: Device overview. (top) on the left is the zoom-in optical micrograph of NCG devices on SiO2/Si substrate with different channel lengths. Scale bar equals 10 µm. Inset shows a cross-sectional view with Pd source (S) and drain (D) electrodes. Structure overview with electrode leads and pads is shown on the right. (bottom) Representative SEM image of a 5 µm channel length device. Scale bar equals 2 µm.

NCG was patterned into a multi-device layout shown in **Figure 4.4**. The devices were fabricated by etching NCG into 100 µm long and 10 µm wide strips and depositing Pd/Cr source and drain contacts, to form NCG channels of 10 µm width *w* and 1-10 µm lengths (see also device fabrication details in **Chapter 3**).

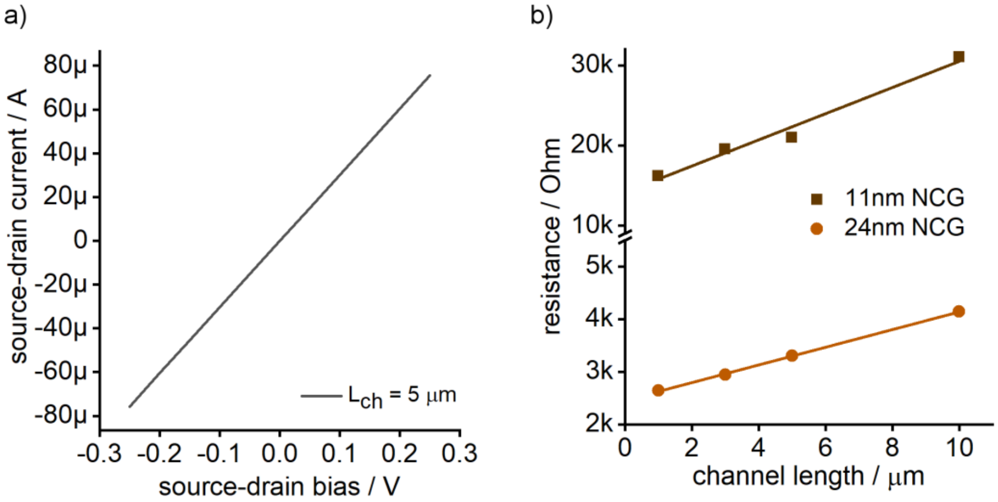

Figure 4.5: I-V curve of the 5 µm channel length device of 24 nm thick film (b) Device resistance vs channel length for the 11 and 24 nm NCG film thicknesses.

The device resistance was determined from the linear current-voltage curves measured for each channel length. **Figure 4.5a** shows the measured current-voltage curve for the 5 µm channel length device. The intention of the large contact area between NCG and the metal electrodes was to minimize the contact resistance. Still, a contact resistance R_C is observed, which is not dependent on the channel length and shows up as an offset of the resistance versus channel length data, as shown in **Figure 4.5b**. R_C is very different for the two film thicknesses (14.2 kΩ@11 nm, 2.45 kΩ@24 nm) showing that the major contribution to R_C comes from the resistance of the NCG layer underneath the metal electrodes. The NCG sheet resistance R_S and the resistivity ρ were determined from the slope of the linear fit to the resistance versus channel length data. We obtain R_S = 16.4 kΩ and $\rho = 1.6 \cdot 10^{-4}$ Ωm for the 11 nm thick film, and R_S = 1.6 kΩ and $\rho = 3.6 \cdot 10^{-5}$ Ωm for the 24 nm thick film. The resistivity values are comparable to thinner films prepared under identical graphitization conditions with similar grain size ($\rho = 6 \cdot 10^{-5}$ Ωm @ 1 nm, $1.2 \cdot 10^{-4}$ Ωm @ 6 nm).[37] The resistivity, however, is significantly different for the 11 nm and 24 nm thick NCG films. To explain why R_S changes by a factor of 10 although the thickness *d* of the 11 nm and 24 nm films differs by only a factor of 2.2, it must be concluded that ρ is layer dependent ($R_S=\rho/d$).

To trace the change in ρ to the microstructure is difficult. On the one hand, the Raman D-mode linewidth and the G-mode position do not show any dependence on the layer thickness, which indicates that the average grain size is not thickness dependent and neither is the degree of graphitization. On the other hand, the temperature dependence of the sheet resistance (for instance, see **Figure 4.6**) for the NCG film can be fitted to a variable range hopping mechanism, which is typical for polycrystalline graphitic films,[137] and shows that grain boundaries are the limiting factor for the charge transport also in NCG. Hence a small change in the tunneling barrier between the grains can lead to a change in the resistivity without leaving a trace in the structural analysis methods.

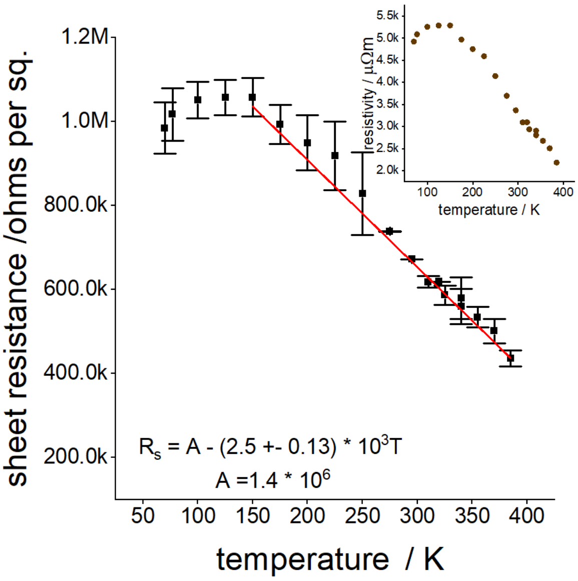

Figure 4.6: Sheet resistance RS of NCG as a function of temperature (77K-400K). Inset shows the resistivity as a function of temperature. The linear temperature coefficient α has been calculated as $\alpha = R_S^{-1} \cdot dR_S/dT$.

Concerning the transport behavior in polycrystalline graphitic films; the conduction mechanism can be described as either metallic or variable range hopping (VRH), depending on the temperature regime. The metallic behavior dominates the conduction at low temperatures, and VRH is responsible for conduction at high temperatures. A similar temperature-dependence of resistance was also observed in the case of NCG. The details of this study can be found in the PhD work of S. Kumar.[138] **Figure 4.6** will be revisited again in the context of bolometric photocurrent discussion.

4.5 Scanning photocurrent spectroscopy

The photocurrents were measured with a lock-in technique to probe the amplitude and the phase. The intensity modulation required for this was induced by the AOTF. Simultaneously with the photocurrent imaging, the laser signal reflected from the sample surface was recorded with a photoreceiver to image the electrodes and to correlate the photocurrent signal with the position of the laser spot.

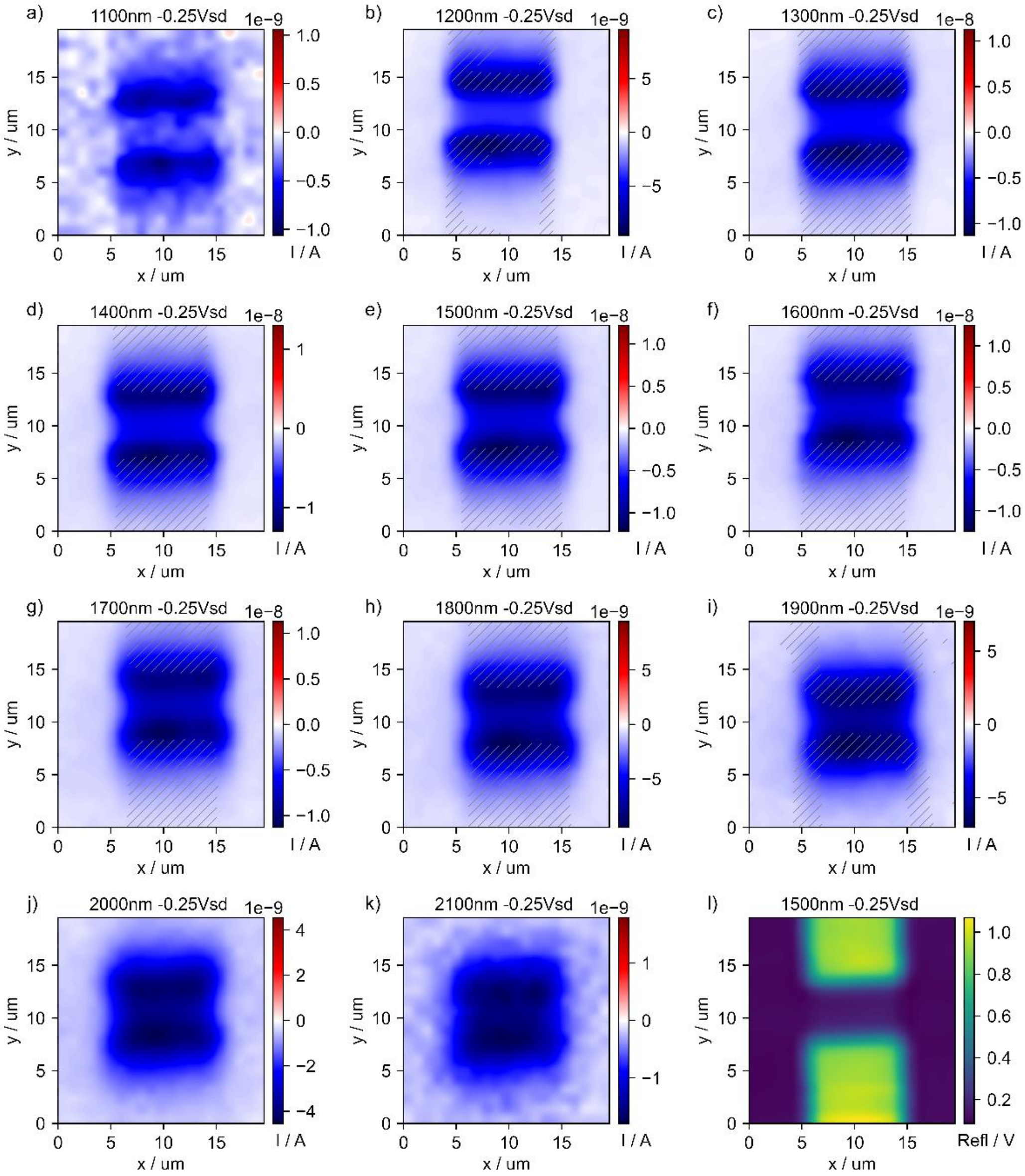

Figure 4.7: Scanning photocurrent imaging at -0.25 V source-drain bias. (a-k) Measurements taken between 1100 nm and 2100 nm wavelength with a device with 24 nm NCG layer thickness and 5 µm channel length. (l) Scanning reflectance images were recorded simultaneously, here shown at 1500 nm during the photocurrent scan. The reflectance data were superimposed on the photocurrent maps in (a-k) as grey shaded areas to indicate the position of the electrodes.

The setup details and the measurement scheme have already been discussed in **Chapter 3**. **Figures 4.7a-k** show the scanning photocurrent images of a device with 24 nm thick NCG and a channel length of 5 µm, recorded at 250 mV source-drain bias. The scans were acquired over a 20 µm x 20 µm area with 1 µm step size and 1100 nm to 2100 nm wavelength range with 100 nm increments. The positions of the electrodes were determined for each scan from the reflectance measurement and overlayed as grey shaded areas to the corresponding photocurrent images. An exemplary reflectance image, recorded at 1500 nm, is given in **Figure 4.7l**. The photocurrents are plotted as the real part $I_{RE} = M \cdot \cos(\varphi - \varphi_{\mathrm{ref}})$ from the magnitude M and the phase φ of the photocurrent signal, with the lock-in reference oscillator phase φ_{ref} set to zero.

From the **Figure 4.7**, it can be seen that photocurrents are generated in the entire NCG channel and the contact region and that the sign of the real photocurrent depends on the polarity of the applied external bias. An imaginary component was not detected. In the wiring scheme, the bias was applied to the drain and the photocurrent was measured at the source.[139] Identical signs of the photocurrent and the voltage bias mean in this experiment that the current increases when the light is on. Note, that the dark current I_{dark} = 250 mV / 3.3 kΩ = 75 µA was not detected with the lock-in technique. For a voltage-biased device, the photo-induced increase of the current is due to a reduction of the resistance. Since NCG has no bandgap, the illumination modulates the charge carrier transport rather than the charge carrier concentration. The relative change in resistance under illumination can be calculated from the photocurrent integrated over the device area $I_{INT\text{-}PC}$ and from the dark current I_{dark} as $(R_{\mathrm{illum}}-R_{\mathrm{dark}})/R_{\mathrm{dark}} = (I_{INT\text{-}PC} + I_{dark} - I_{dark}) / I_{dark}$, which yields ≈ 2 % at 1500 nm with $I_{INT\text{-}PC} \approx 1.5$ µA. Since the absorbed photons are converted into heat, relevant is the temperature dependence of the resistance, and this has been measured for the case of a thin NCG film (**Figure 4.6**). Expectedly, the resistance decreases with temperature due to thermally activated grain-to-grain tunneling of carriers leading to variable-range hopping in the nanocrystalline material.[35] At room temperature, for the linear temperature coefficient of the resistivity $\alpha = \rho^{-1} \cdot \mathrm{d}\rho/\mathrm{d}T = -0.004 \cdot \mathrm{K}^{-1}$, the light-induced heating by several kelvin leads to the measured photocurrents. Hence it can be concluded that the photocurrent measured at finite bias is bolometric.

It is instructive to look closer at the bolometric photocurrent distribution, which is determined by the local bolometric current density

$$\vec{J}_{bol} = -\alpha \cdot \rho^{-1} \cdot \Delta T \cdot \vec{E} \qquad (4.1)$$

and depends not only on the temperature coefficient α, the resistivity ρ, and the photo-induced change in temperature ΔT, but also on the electric field $\boldsymbol{E}$. The bolometric current is thus proportional to the electric field distribution and disappears in field-free regions. From TMM simulations we have determined that 14-20 % of the light is absorbed by the Pd metal electrodes (**Figure 4.8**). The rest of the light is back-reflected and none is absorbed by the NCG underneath the Pd. As a result, the heating of NCG is much smaller underneath the Pd electrodes than in the channel, where 60 % of the light is absorbed by NCG. Still, the bolometric current close to the electrodes is larger than in the center of the channel, which shows that the electric field is larger at the contact than in the channel. This is not surprising since the resistance of the 5 µm long channel is 0.85 kΩ, whereas the resistance R_C of the regions next to the channel accounts for 2.45 kΩ. Hence 74 % of the applied bias drops off at the two contact regions. The bolometric current distribution shows that these regions are narrow and lead to a large electric field that is concentrated to a narrow region at the Pd electrodes. Since R_C is determined by the NCG thickness and not by the interface between NCG and Pd, the electric field distribution is very similar for the 11 nm NCG device, where we find that 71 % of the applied bias drops at the contact region. Therefore, the photocurrent distribution looks similar for the thinner NCG film as shown in **Appendix 2.1**. The temperature coefficient α of NCG is one order of magnitude larger than that of graphite,[140] resulting in a correspondingly higher bolometric responsivity (eq. 4.1).

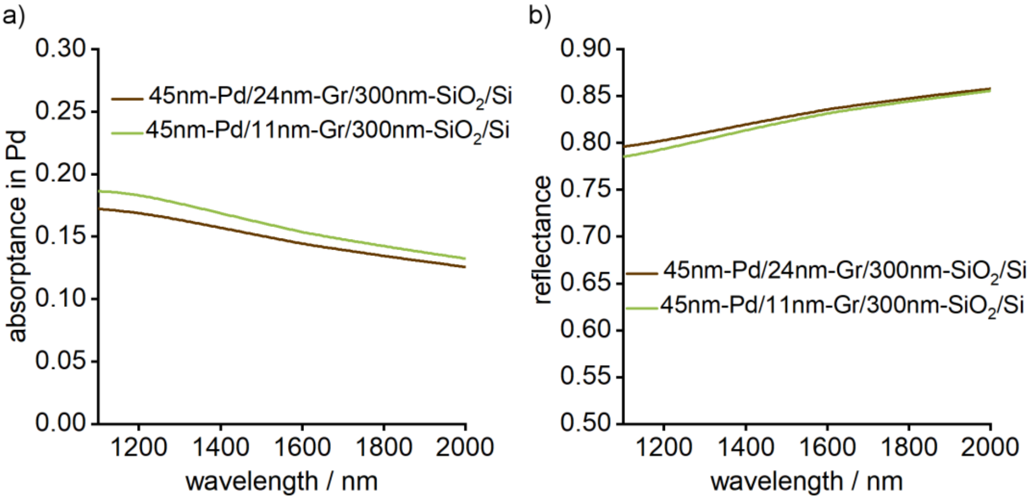

Figure 4.8: Simulated absorptance in Pd (a) and reflectance from the Pd/Gr/SiO2/Si multilayer (b).

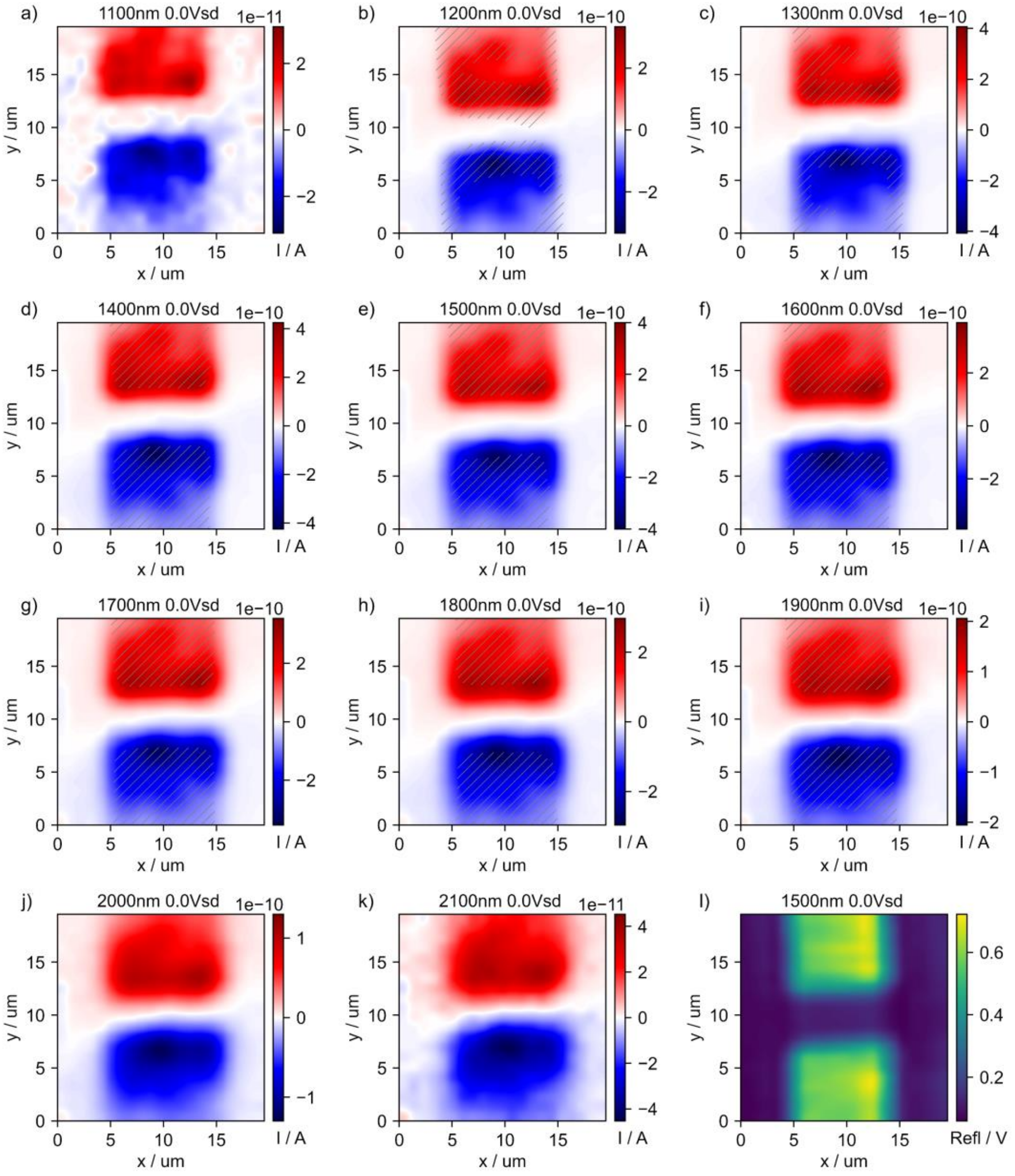

Figure 4.9: Scanning photocurrent imaging under short-circuit conditions. (a-k) Measurements taken between 1100 nm and 2100 nm wavelength with a device with 24 nm NCG layer thickness and 5 µm channel length. (l) Scanning reflectance images were recorded simultaneously, here shown at 1500 nm during the photocurrent scan. The reflectance data were superimposed onto the photocurrent maps in (a-k) as grey shaded areas to indicate the position of the electrodes.

At zero bias, the scanning photocurrent images look very different, as shown in **Figures 4.9a-k** for the same 24 nm thick NCG device. The data for the 11 nm thick layer is shown in the **Appendix A2**. Photocurrents are generated at the electrodes and with opposite signs at the source and drain electrode. Furthermore, in the channel between the electrodes, the photocurrent is zero. Unlike in the bolometric case with an external bias voltage, the appearance of photocurrents at zero bias requires the generation of a photovoltage. The data shows that this occurs over a large area of the electrodes where Pd forms an interface with NCG. As described before, light is not transmitted through the Pd layer and to a large extent back-reflected. But 14-20 % is absorbed in the Pd and is thus heating indirectly the interface. This leads to the build-up of a voltage across the interface as a result of the difference in the materials Seebeck coefficients S_{NCG} and S_{Pd}. Such a photo-thermoelectric (PTE) effect, induced by contact-heating, has been observed previously on graphene/Au contacts.[141]

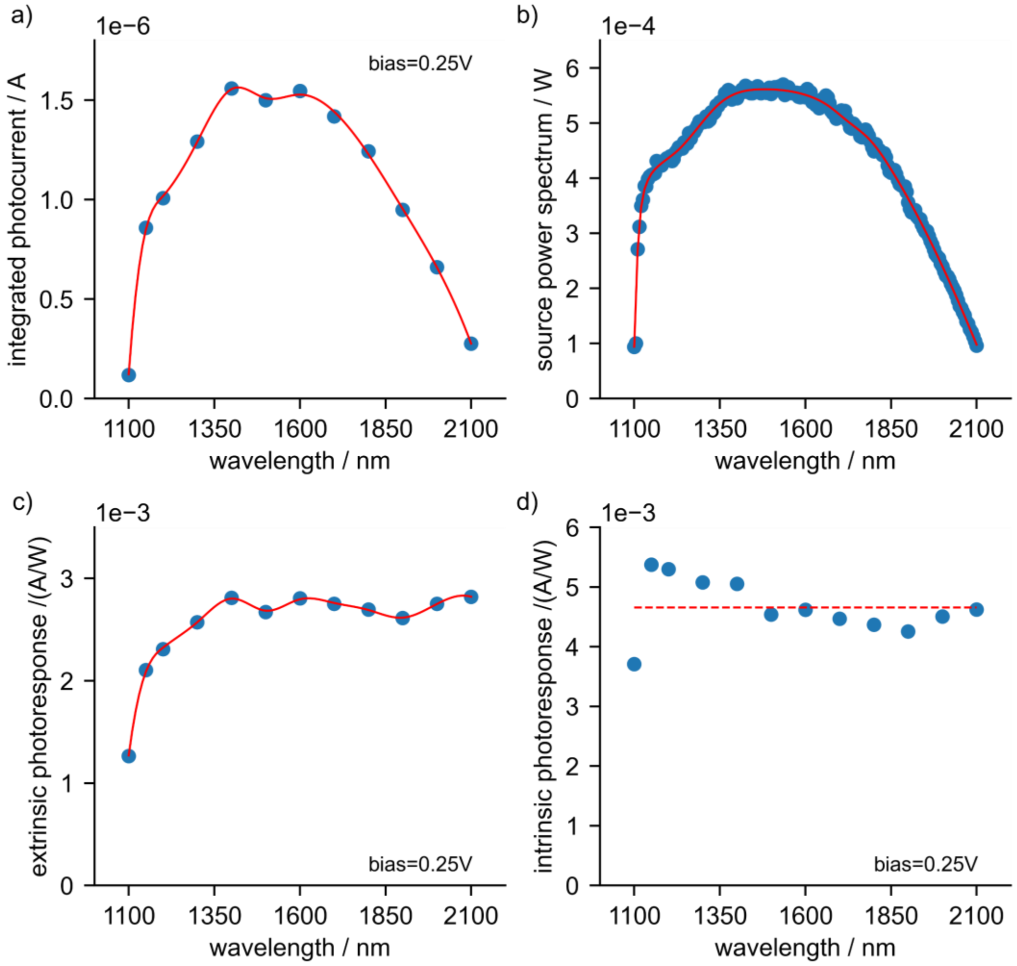

Figure 4.10: Spectroscopic analysis. (a) Integrated photocurrent obtained from the scanning photocurrent maps in Figure 3 of the 24 nm thick NCG device. (b) Calibrated power spectrum measured after wavelength-specific intensity adjustment of the supercontinuum light source by the AOTF. (c) Extrinsic photoresponse from the normalization of the integrated photocurrent with the power spectrum. (d) Intrinsic photoresponse from the normalization of the extrinsic photoresponse with the graphite absorptance.

The spatial extent of such a PTE photocurrent is determined by the heat diffusion and cooling in the structure and the distance of the laser spot from the electrode gap. As a result, the PTE photocurrent extends more into the electrodes than the bolometric photocurrent, which is limited to areas with electric fields induced by the external bias voltage. The PTE photovoltage V_{PTE} is determined by $V_{PTE} = (S_{Pd} - S_{NCG})\cdot\Delta T$, and can be calculated from the PTE photocurrent, integrated over one electrode, and multiplied with the device resistance. We find that V_{PTE} is on the order of 10 µV, which is reasonable assuming that ΔT is on the order of kelvin, and $S_{Pd} - S_{NCG}$ on the order of $\mu V\cdot K^{-1}$.[142,143] The enhanced PTE photocurrents at the corners of the electrodes is a typical signature of a local light-field enhancement leading to enhanced light absorption and heating of the interface.[144] For applications, the bolometric operation mode is advantageous since the entire NCG channel is photoactive and the weak PTE photocurrents with opposing signs do not play a role if the applied voltage bias is larger than V_{PTE}. To quantify the targeted broadband response, the wavelength dependence of the device responsivity was determined, the external responsivity.

The scanning photocurrent maps over the device area were first itntegrated for each wavelength to obtain the photocurrent spectrum shown in **Figure 4.10a**. The parabola-shaped wavelength dependence originates from the spectrum of the light source (**Figure 4.10b**) and the external photoresponse was then calculated by normalizing the photocurrent spectrum with the source spectrum. **Figure 4.10c** shows that the device responsivity is about $2.8\cdot10^{-3}$ A/W over a wide wavelength range. The responsivity falls off below 1300 nm due to the weaker absorptance of light in the NCG layer for the selected layer thicknesses of NCG and SiO_2 on Si (green curve in **Figure 4.1d**). If we normalize the extrinsic responsivity with the simulated NCG light absorptance, we obtain a nearly flat intrinsic responsivity within a 15 % range around $4.7\cdot10^{-3}$ A/W (**Figure 4.10d**). The specific detectivity D^* for the 24 nm thick NCG device is 10^6 Jones at 0.25 V bias and 1500 nm. We have used the expression $D^* = R\cdot(A/(2\cdot q\cdot I_{\mathrm{dark}}))^{0.5}$ with $I_{\mathrm{dark}} = 75$ µA, device area A = (5x10) µm^2, the responsivity R, and the elementary charge q, because our device is shot-noise limited.[145] The spectroscopic analysis for the 11 nm thick NCG device is given in **Appendix**. The weak wavelength dependence is a consequence of the approximation of the optical properties of NCG by graphite in the TMM simulations, which is good but not perfect. This conclusion can be drawn because the responsivity over wavelength is plotted in units of current per power. A bolometric photocurrent is proportional to the absorbed power and hence wavelength-independent for constant absorbed power. The same would be true for a PTE photocurrent. In contrast, a photovoltaic current would be proportional to the photon flux, not the power.

The use of the locally integrated photocurrent to determine the photoresponse requires explanation. In our scanning photocurrent measurements, the photoactive device area is larger than the laser spot size. As a result, the measured photocurrent under local illumination is not equivalent to measurements under global illumination. This can be understood when treating the channel as a 2D network of resistors.[146] Under local illumination, the resistance of the illuminated area changes while the resistance in the non-illuminated remains unchanged. As a result, the current distribution in the biased channel depends on the size and the position of the illuminated area. We simulated the scanning photocurrent experiment by solving the stationary continuity equation of the bolometric photocurrent $\nabla \vec{j}_{bol} = 0$, using a finite element method (FEM) solver in 2 dimensions. The illuminated spot within the simulated channel was mimicked as a region with reduced resistivity and the current was calculated with Dirichlet and Neumann boundary conditions for the potential at the sides with and without electric contacts, respectively. (see details in **Chapter 3**). The scanning photocurrent measurement was simulated by calculating the current for every position of the laser spot, keeping the step size of the raster scan equal to the spot size. The simulation shows that spatially integrating the scanning photocurrent is equivalent to measurements under global illumination with the same light intensity per area, provided that *r*, the ratio between the resistivity with and without illumination, approaches unity as shown in **Figure A3 in Appendix**. In our experiment, *r* is only a few percent, and the method is therefore applicable.

4.6 Discussion

The thickness dependence of the photoresponse of the NCG films; **Figure 4.11a-c** shows the local absorption, the Poynting vector, and the resulting absorptance in the graphite layer versus the graphite layer thickness at 1550 nm wavelength. The simulations show that reducing the NCG from 24 nm to 11 nm reduced the absorptance by 10 %. However, the measured photoresponse of the 11 nm NCG device is ~3 times lower than that of the device with the optimum NCG thickness of 24 nm (**Figure 4.11d**). This is understood by the ~4 times higher resistivity of the thinner NCG layer, likely due to a thickness-dependent grain structure of the NCG film, which leads to a larger reduction in the photoresponse for the thinner film as expected solely from light absorptance.

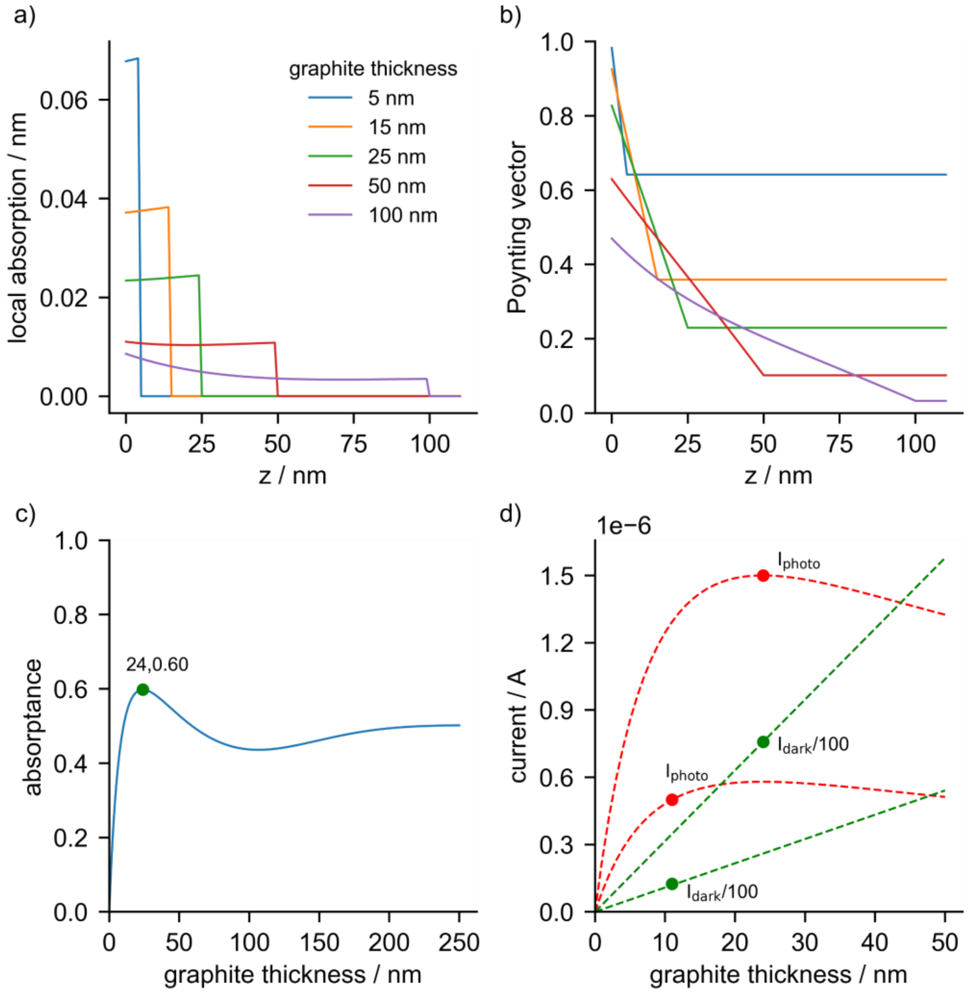

Figure 4.11: (a) Local absorption, (b) Poynting vector, and (c) resulting absorptance in the graphite layer versus the graphite layer thickness at 1550 nm wavelength. (d) Bolometric photocurrent (I_{photo}) and dark current (I_{dark}) measured for 11nm-NCG and 24nm-NCG devices (dots) with extrapolations based on simulation data from (c) and the measured resistivities.

Concerning other thin-film/2D photodetectors, the bolometric responsivity of NCG is quite comparable, with the benefit that the NCG devices require a rather low bias voltage (see **Table 4.2**). Also, the spectral flatness, that can be shifted to other wavelength ranges, in combination with the absence of an intrinsic wavelength cutoff in the absorption makes NCG a potentially interesting material for longer wavelength detection. Furthermore, the NCG photodetectors are made of non-toxic materials and are RoHS compliant. Unfortunately, the detectivity is rather low and in the same range as carbon nanotube-based broadband photodetectors,[73] but nevertheless sufficient for spectroscopy and imaging with moderate light power sources. An improvement towards sensing lower light levels could be realized by using a higher bias and a modified structure. For instance, the addition of a reflective layer underneath the thickness-optimized NCG layer would result in a near-unity absorptance and enhance the responsivity while preserving spectral flatness. Also, the thermalization by the substrate could be eliminated by under etching the NCG layer, to reach a higher ΔT. Further, an optimization of the device geometry to maximize the electric field within the channel region can be envisioned, and hence the bolometric response.

Table 4.2: Compilation of photodetector key performance figures.

Material	**Wavelength / nm**	**Incident power**	**S-D bias / V**	**Responsivity / (mA/W)**
Graphene	1300	3 mW	1.5	0.5
Graphene	1550	10 mW	0.05	6
Si QDs - Graphene	375 – 1870 2500 – 4000	0.2 µW/cm^2 375mW/cm^2	1	10^4 (MIR) 10^{12} (UV-NIR)
MoS$_2$	445 – 2712	8 mW	10	40
a - MoS$_2$	473 – 2712	4 mW	10	47
β - In$_2$Se3/MoS$_2$	830	50 mW cm^{-2}	1	2.4
MoS$_2$ – BP	1550	400 µW	3	20
MoTe$_2$	600 – 1550	20 nW	10	24 at 1060 nm
R6G/MoS$_2$	405 – 980	1 mW	0.1	1.38
BP	940	10 nW	0.2	4.8
Bi$_2$Te$_3$	1064 – 1550	0.67-2.8 mW	2	3.64 at 1064 nm
NCG	1100 – 2100	100 – 550 µW	0.25	4-5 (1100nm-2100nm)

4.7 Conclusion

In summary, spectrally-flat broadband photodetection in the near- to short-wavelength infrared has been realized with light-field simulation optimized nanocrystalline graphite on SiO_2/Si substrates. The flat responsivity is not limited to the chosen wavelength range and can be adjusted to other parts in the electromagnetic spectrum by tailoring the layer thickness of NCG and SiO_2 accordingly. This optimization is possible because the absorptance of graphite is wavelength-independent up to 30 nm thickness. This conceptually new approach could be of interest when spectral flatness over an extended wavelength range is important. Compared to previous works with thinner films, the bolometric photoresponse at moderate voltage bias is two orders of magnitude larger, and has the potential to be further improved through grain size and grain boundary engineering,[66,147] back-reflective coating, thermal decoupling, and electric field optimization.

Chapter 5 NIR Photodetection with Carbon Nanotube Films

Introduction

In single-walled carbon nanotubes (SWCNTs), the diameter (d_t) and the excitonic optical transition energies (E) have an inverse relationship, and due to this E-d_t scaling, the nanotube diameter can be tuned for the energy-selective light absorption. In particular, with the increasing diameter, SWCNTs become optically active in the technologically relevant near-infrared telecommunication band. Though the single-tube device architecture helps understand the nanoscale device physics, the small absorption cross-section of the individual nanotubes makes them inefficient photodetectors for practical applications. Therefore, large-area devices with high nanotube densities are necessary. In this chapter, carbon nanotube film networks with a diameter distribution suitable for the near-infrared photodetection were synthesized on the SiO_2/p-Si substrate. The growth process of SWCNT films is first briefly described, followed by the film characterization using multi-wavelength resonant Raman spectroscopy for determining the diameter distribution and SWCNT type from the radial breathing mode (RBM) frequency. The devices were fabricated on the CNT-SiO_2/p-Si substrates in a transistor geometry. Scanning photocurrent measurements were conducted in the 1100 nm – 1800 nm spectral region under short-circuit and biasing conditions, and the resulting photoresponse is discussed in terms of the photodetection mechanisms.

Contribution: I have fabricated the CNT devices and performed the scanning photocurrent measurements.

5.1 Raman spectroscopy of carbon nanotube films and device fabrication

The semiconducting single-walled carbon nanotube (s-SWCNT) films with a diameter distribution tailored for the near-infrared (NIR) photodetection were synthesized at the Institute of Metals Research, Shenyang. In this section, the growth process of the CNT films is briefly described. The detailed synthesis and growth mechanism can be found in the work of F. Zhang and co-workers.[148]

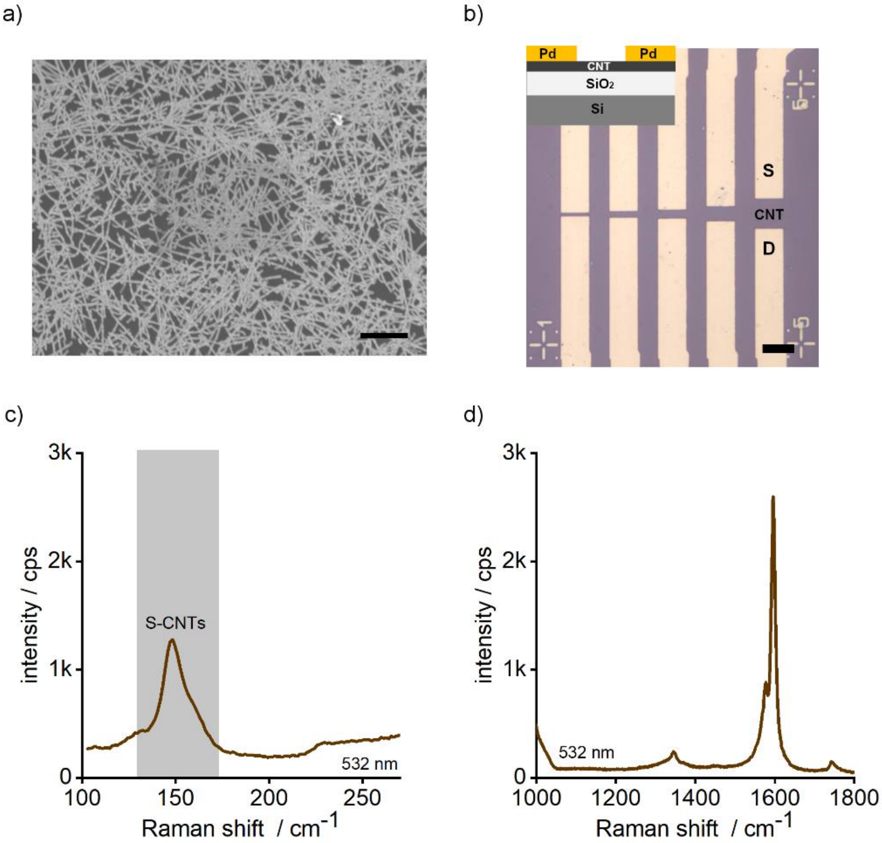

Figure 5.1: Fabrication and characterization of CNT devices. (a) SEM micrograph of CNT film on SiO_2/Si substrate. Scale bar equals 2 µm. (b) Optical micrograph of CNT devices on 300nm-SiO_2/Si substrates with different channel lengths. Scale bar equals 10 µm. Inset shows a cross-sectional view with the Pd source (S) and drain (D) electrodes. (c), (d) Raman spectra of CNT/300nm-SiO_2/Si.

The SWCNT networks were synthesized on SiO_2/Si substrates by chemical vapor deposition (CVD) process at 700 °C using Co nanoparticles with a partial carbon coating layer as a catalyst material. Ethanol was used as a carbon source and hydrogen as a carrier gas. A small change in the diameter and chirality in the SWCNTs can modify the electrical type from semiconducting (s) to metallic (m), and hence, the synthesized films are a mixture of m-SWCNTs and s-SWCNTs (as confirmed by electrical and Raman measurements below). During the synthesis process, H_2 gas also functions as an *in-situ* etchant for the selective etching of m-SWCNTs. However, the Raman measurements detect the presence of also the metallic tubes in the network. The diameter distribution in the network was tailored by controlling the coverage of carbon coating on the Co nanoparticle catalyst. Furthermore, the carbon coating prevents the agglomeration of nanoparticles and thus enabling a close diameter control in the SWCNT film. **Figure 5.1a** shows a scanning electron micrograph of a dense network of SWCNTs with lengths extending up to several microns. **Figure 5.1c-d** shows the Raman spectra of the CNT film characterized using a 532 nm (2.33 eV) excitation laser line. In **Figure 5.1c**, the peak at ~148 cm^{-1} corresponds to the radial breathing mode (RBM) originating from the s-SWCNT according to the Kataura plot.[149] Using different excitation laser lines and from the RBM peak positions, the SWCNTs can be assigned to either m-SWCNT or s-SWCNT. **Figure 5.1d** shows the characteristic G^+ (high-frequency mode) and G^- (low-frequency mode) Raman active modes near ~1590 cm^{-1} observed in isolated and bundled metallic/semiconducting SWCNTs.[150] The discussion on the relative intensities and shape of the G^+ and G^- peaks in relation to the type of CNTs is outside the scope of the current chapter.

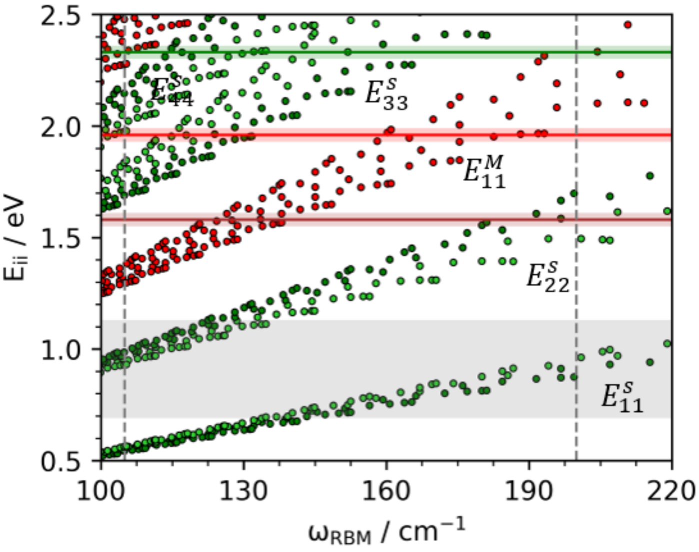

Figure 5.2: The calculated optical resonances ΔE = E_{ii} for SWCNTs in the 100 – 220 cm^{-1} frequency range. The E_{ii} versus ω_{RBM} (Kataura plot) was calculated using the equations presented in the work of Araujo et al.[151] The solid lines in color indicate the E_{laser} used in the Raman measurements and the narrow color strips correspond to the respective width of the resonance region (E_{laser} ± 0.06) eV. The grey shaded region represents the laser excitation energies in the photocurrent experiment. The vertical dashed lines correspond to the measured radial breathing mode frequency region of the SWCNT network.

To understand the type (metallic or semiconducting) and diameter of the SWCNTs present in the network, **Figure 5.2** is considered first, which shows the calculated optical transition energies ($E_{ii}^{S,\,M}$) for different SWCNTs as a function of radial breathing mode (RBM) frequency (ω_{RBM}), referred to also as a Kataura plot. The Jorio group in their work on the "super-growth" SWCNTs on SiO_2/Si substrates, formulated a set of equations to study the transition energies E_{ii} as a function of nanotube diameter (d_t), chiral angle (θ), and chiral index (i). The optical transition energies in **Figure 5.2** were calculated using the equations described in the work of Araujo et al.[151] Experimentally, the optical resonances and RBM frequencies of the SWCNTs can be accessed through resonant Raman scattering as described below. See also **Chapter 2** for a discussion on the details of the Kataura plot. The green and red bullets in **Figure 5.2** correspond to the semiconducting (E_{ii}^{S}) and metallic transition (E_{ii}^{M}) energies. Starting from the bottom, the lowest group of optical transitions represent E_{11}^{S}, followed by E_{22}^{S}, E_{11}^{M}, E_{33}^{S} and so on. The colored solid lines at (532 nm = 2.33 eV), (633 nm = 1.95 eV) and (785 nm = 1.57 eV) indicate the laser excitation energies used for the Raman measurements. A radial breathing mode is observed when the laser excitation energy is close to one of the E_{ii} transitions (red or green bullets). The experimentally observed RBM frequencies in the SWCNT film for the three excitation energies span the 105 - 200 cm^{-1} wavenumber shift, as indicated by the two dashed vertical lines in the plot (See **Appendix A4** for the complete distribution of RBM frequency from the three laser energies). By mapping the measured RBM frequencies from the three laser lines onto the **Figure 5.2,** it can be concluded that the 532 nm and 633 nm laser lines excite the RBM modes in semiconducting tubes, whereas 633 nm and 785 nm excite the metallic tubes in the network. In **Figure 5.2**, the narrow strip of colored regions around the respective laser excitation energies represents the resonance window. The resonance window is defined as the range of laser energy values relative to E_{ii} that can result in a RBM mode, typically the resonance window is $E_{laser} \pm 0.06$ eV.[59] It should be noted that the change in SWCNT environment results in a 40 - 100 meV red shift in the E_{ii} transitions.[152],[153] Finally, from the above discussion on the measured RBM frequencies, it can be concluded that the SWCNT network consists of both semiconducting and metallic tubes.

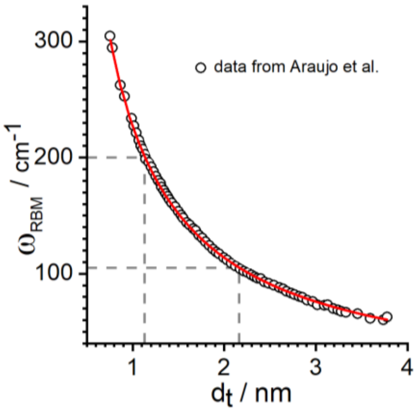

Figure 5.3: RBM data from Araujo et al. shown in open circles.[154] The RBM frequency range (105 - 200 cm^{-1}) of the SWCNT film (from **Figure 5.2**) is mapped here as the dashed horizontal lines, and the corresponding vertical lines indicate the diameter range in the film.

The RBM frequency can be used to calculate the nanotube diameter by using the relation $d_t = (227/(\omega_{RBM} - 0.3))$ for the nanotubes grown on silicon substrates.[154] Araujo et al. studied the correlation between the RBM frequency and nanotube diameter, and their experimental data is reproduced in **Figure 5.3** (open circles). In order to estimate the diameter distribution of the SWCNT film investigated here, the RBM frequencies (105 cm^{-1} to 200 cm^{-1}) obtained from the Raman measurements were mapped (horizontal dashed lines, ω_{RBM} axis in **Figure 5.3**) onto the data of Araujo et al. and the vertical lines projected onto the diameter (d_t) axis predict a diameter distribution of 1.13-2.16 nm. The calculated optical transitions (energy gaps) and the nanotube diameter for the SWCNTs in the diameter range 1.13 nm – 2.16 nm is given in **Table 5.1**. In the $E^S - d_t$ relation, γ_0 is the interaction energy between the neighboring carbon atoms and a_0 is the carbon-carbon bond distance.[155] E^S_{11} to E^S_{44} denote the energy states of the first four semiconducting optical transitions. E^M_{11} and E^M_{22} denote the first and second metallic transitions. In the photocurrent experiment, the targeted NIR excitation wavelength (1100 nm – 1800 nm) range overlaps with the E^S_{11} and E^S_{22} transitions (**Table 5.1**), shown as region in grey in **Figure 5.2**.

Table 5.1: Predicted optical transitions of s-SWCNTs and m-SWCNTs in the CNT network.

Energy gap	**d_t = 1.13 nm** **$\lambda_{optical}$ / nm**	**d_t = 2.16 nm** **$\lambda_{optical}$ / nm**
$E^S_{11} = \frac{2a_0\gamma_0}{d_t}$	1701	3252
$E^S_{22} = \frac{4a_0\gamma_0}{d_t}$	851	1626
$E^M_{11} = \frac{6a_0\gamma_0}{d_t}$	567	1084
$E^S_{33} = \frac{8a_0\gamma_0}{d_t}$	425	813
$E^S_{44} = \frac{10a_0\gamma_0}{d_t}$	340	651
$E^M_{22} = \frac{12a_0\gamma_0}{d_t}$	284	542

Finally, the CNT film was patterned with a multi-device layout as shown in optical micrograph in **Figure 5.1b**. The devices were fabricated by etching CNT film into 100 µm long and 10 µm wide strips and sputtering Pd/Cr source and drain contacts, to form CNT channels of 10 µm width *w* and 1-10 µm lengths *l* (see also **Chapter 3** for experimental details).

5.2 Electrical characterization

The electrical characterization of the CNT devices (**Figure 5.1b**) was conducted after vacuum annealing at 430 °C for one hour. The devices were measured in the transistor configuration with silicon substrate as the back gate. **Figure 5.4a-c** show the transconductance of the devices with three different channel lengths. All the measured devices show moderately p-type characteristics. The source-drain bias and gate voltage range were kept at low values to minimize the risk of device damage before the photocurrent measurements (see also methods section in **Chapter 3**). In the measured gate voltage window, the devices do not show a clear off state, with the On/Off ratio being at most ≈10 for the largest channel length device of 10 µm. The low On/Off ratio implies that the residual m-SWCNTs are long enough to short-circuit the channel, resulting in a higher off-state current. An On/Off ratio up to 10^6 was reported for devices fabricated with the similar channel material but with channel width of 100 µm and channel length greater than 40 µm.[148]

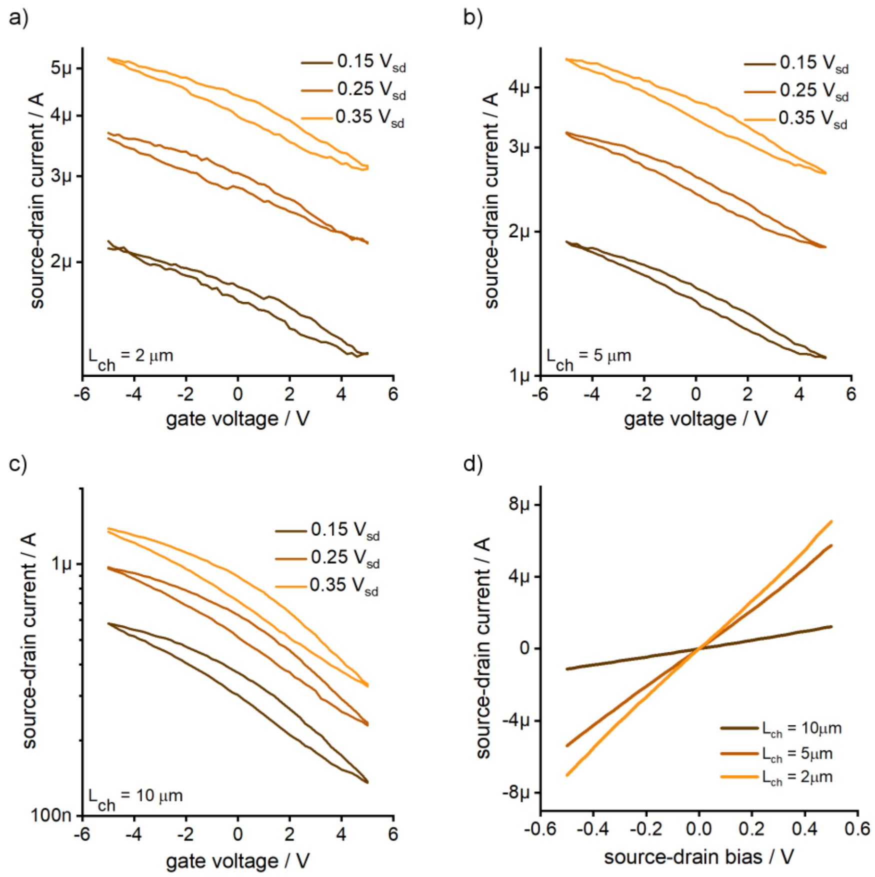

Figure 5.4: Electrical characterization of the SWCNT devices. (a)-(c) Transfer characteristics. (d) current - voltage (I_{sd}-V_{sd}) characteristics with no applied gate voltage.

A small hysteresis was observed in all the devices. Hysteresis in nanotube transistors arises out of the charge-trap states resulting from: charge doping from the molecules in the ambient atmosphere, trapped charges at the gate oxide/air interface, and mobile charges associated with the oxide layer. Strategies to reduce hysteresis in nanotube devices include surface functionalization of oxide with a dielectric hydrophobic layer such as polytetrafluoroethylene (PTFE).[156] Additionally, packaging nanotubes between a h-BN bottom layer and PTFE top layer eliminates hysteresis.[157] **Figure 5.4d** shows the current-voltage characteristics, and the device resistance extracted from the slope of the I-V curves is between 80 kOhm – 430 kOhm.

5.3 Scanning photocurrent measurements

The devices were wire bonded to a chip carrier and mounted to the photocurrent setup as shown in **Figure 3.4** of **Chapter 3**. Identical to the photocurrent measurement procedure described for the NCG films, a similar experimental protocol was implemented for the photocurrent measurements of CNT devices. The broadband supercontinuum (SC) spectrum was first transformed into a smooth power spectrum from 1100 to 2100 nm by implementing a wavelength-specific intensity adjustment to the acousto-optic tunable filter (AOTF) as described in **Chapter 3**. The chromatic aberration of the setup was compensated by adjusting the focus through the piezo-controlled NIR objective to have a diffraction-limited laser spot at each wavelength before scanning the device. The photocurrents were measured with a lock-in technique to probe the amplitude and the phase of the signal; the laser intensity modulation required for this was induced by the AOTF. The AOTF was electrically modulated to have sinusoidal light output with minimum intensity near zero to result in a high signal-to-noise ratio in the measured photocurrents. In sync with the photocurrent imaging, the laser signal reflected from the device area was recorded with a NIR photoreceiver to image the electrodes and device area to correlate the photocurrent signal with the position of the laser spot. For additional details of the setup, and measurement technique see **Chapter 3**.

The photocurrent measurements on CNT films were carried out under three conditions: zero-bias, a fixed source-drain bias, and a gate voltage bias. The NIR wavelength range 1100 nm – 1800 nm was chosen to target the E_{11}^{S} and E_{22}^{S} region of the s-SWCNTs (see **Table 5.1**.) In this section, the photocurrent measurements at zero bias are described first, then followed by the measurements with a source-drain bias and under gate voltage. **Figure 5.5a-k** show the scanning photocurrent images of a CNT film device with a channel length of 10 µm, recorded at the short-circuit conditions. The scans were acquired over a 20 µm x 20 µm area with 1 µm step size and 1150 nm to 1800 nm wavelength range with 50 nm or 100 nm increments. The positions of the electrodes were determined for each scan from the reflectance measurement and overlaid as grey shaded areas to the corresponding photocurrent images. The reflectance image recorded at excitation wavelength of 1550 nm, is shown in **Figure 5.5l**. The photocurrents are plotted as the real part $I_{RE} = M \cdot \cos(\varphi - \varphi_{ref})$ from the magnitude M and the phase φ of the photocurrent signal, with the lock-in reference oscillator phase φ_{ref} set to zero.

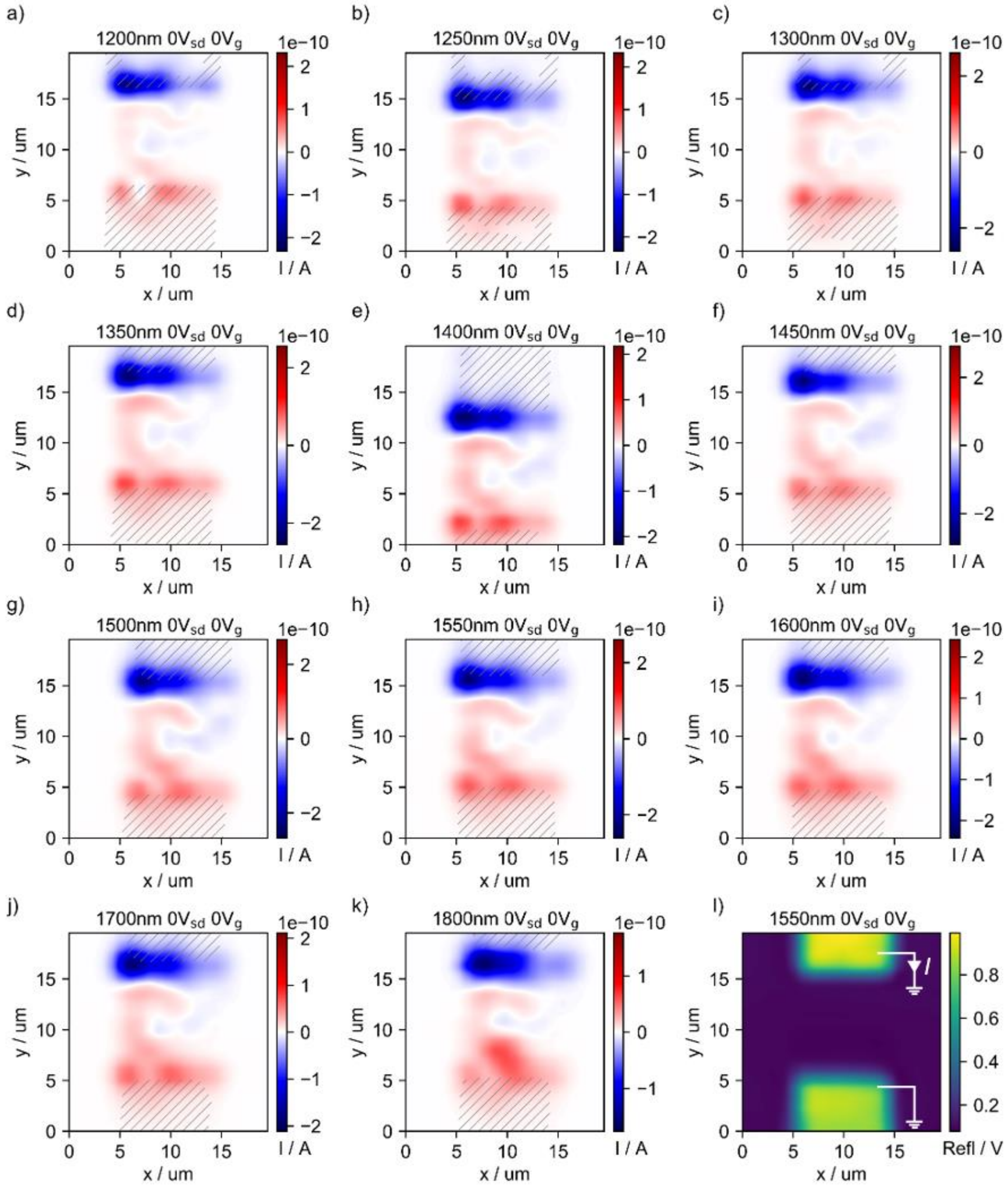

Figure 5.5: Scanning photocurrent imaging under short-circuit conditions. (a-k) Measurements taken between 1200 nm and 1800 nm wavelength with a device of 10 µm channel length. (l) Scanning reflectance images were recorded simultaneously, here shown at 1550 nm during the photocurrent scan. The electrode with current amplifier and grounded electrode are indicated. The reflectance data are superimposed onto the photocurrent maps in (a-k) as grey shaded areas to indicate the position of the electrodes.

Here, a positive current is defined as flowing from source to drain. From the photocurrent maps, it can be observed that the photocurrents are generated at both the source and drain electrodes with opposite signs. The photocurrent in the channel region is non-zero and has a distribution that is reproducibly seen in all the wavelength maps. In the setup, the current preamplifier is connected to the source electrode and the drain electrode is grounded. In this configuration, the phases recorded at source and drain electrodes are $\phi \approx 180°$ and $\phi \approx 0°$ corresponding to negative and positive real photocurrents, respectively. Strong localized photocurrents on the order of 100 pA are generated near the contact regions, and the photocurrent drops off away from the metal-CNT edge.

To explain the observed short-circuit photoresponse in the CNT film, the photocurrent behaviour in nanocrystalline graphite (NCG) described in **Chapter 4** is briefly recalled. A comparison can be drawn since the device architecture (channel width, electrode material, and electrode thickness) is identical in CNT and NCG devices. In NCG devices, under short-circuit conditions, a strong photocurrent signal was measured at the contacts and a zero signal in the center of the channel. The photocurrent signal on the metal contacts was attributed to light absorption in palladium electrodes and thereby indirectly heating the NCG film underneath. In the 1100 nm – 1800 nm wavelength range, 14 -20% of light is absorbed in palladium contacts (See **Chapter 4**). A strong signal was observed at the metal-NCG edge due to the light absorption in both metal and NCG film. The observed photocurrents were attributed to a photothermoelectric origin due to the difference in the Seebeck coefficients (Pd and NCG) and local rise in temperature near the illuminated contact. Since the NCG film is homogenous, the Seebeck coefficient at the center of the channel is uniform, resulting in zero photoresponse. With this background on the NCG devices, we now proceed to understand the photoresponse in the CNT devices by considering the photothermoelectric effect.

Similar to the NCG device, the maximum photocurrent signal at the contact-CNT edge is likely due to the light absorption in both CNTs and the metal electrode. However, in the channel region, the photocurrent is non-zero. The likely scenario in the channel is that the metal is not directly heated but rather heated indirectly through the light absorption in sc-SWCNTs (see **Table 5.1**, in the photocurrent experiment, only the sc-SWCNTs can be excited). However, the local heating depends on the microscopic arrangement of the tubes in the network, and probing at the individual tube level is difficult due to the lack of spatial resolution. In the case of NCG film, the channel had a uniform Seebeck coefficient, and consequently a zero photoresponse. The non-zero photoresponse in the CNT channel is likely due to a non-uniform Seebeck coefficient. Indeed, the presence of different tube chiralities (m- or s-SWCNTs) in the film can modify the Seebeck coefficient. For a similar diameter range, the intrinsic Seebeck coefficient of the s-SWCNTs can be an order of magnitude higher than for the m-SWCNTs. The Seebeck coefficient of s-SWCNTs can be as high as several hundreds of µV/K. For instance, Hung et al. calculated a Seebeck coefficient of 400 µV/K for s-SWCNT with a diameter ≈ 1.5 nm.[158] In another report by Hu et al. a Seebeck coefficient between –87 µV/K to 70 µV/K was reported for SWCNT films depending on the doping in the film.[159] Furthermore, in an SWCNT film network, the fraction of metallic content dictates the overall Seebeck coefficient. Higher the s-SWCNT purity in the network, the larger is the film's Seebeck coefficient. It should also be noted (from SEM image in **Figure 5.1**) that there are dense/thick and sparse/thin regions within the network, which can have very different Seebeck coefficients due to the difference in air doping and the associated slow thermal desorption from dense regions.[91] The random orientation of the nanotubes in the network and the multitude of m-SWCNT/s-SWCNT and s-SWCNT/s-SWCNT intertube junctions strongly influence the overall electrical and heat transport in the film.[160] The localized photocurrent distribution within the channel is resolvable due to the diffraction-limited laser spot, which was otherwise not possible under a global illumination.[91]

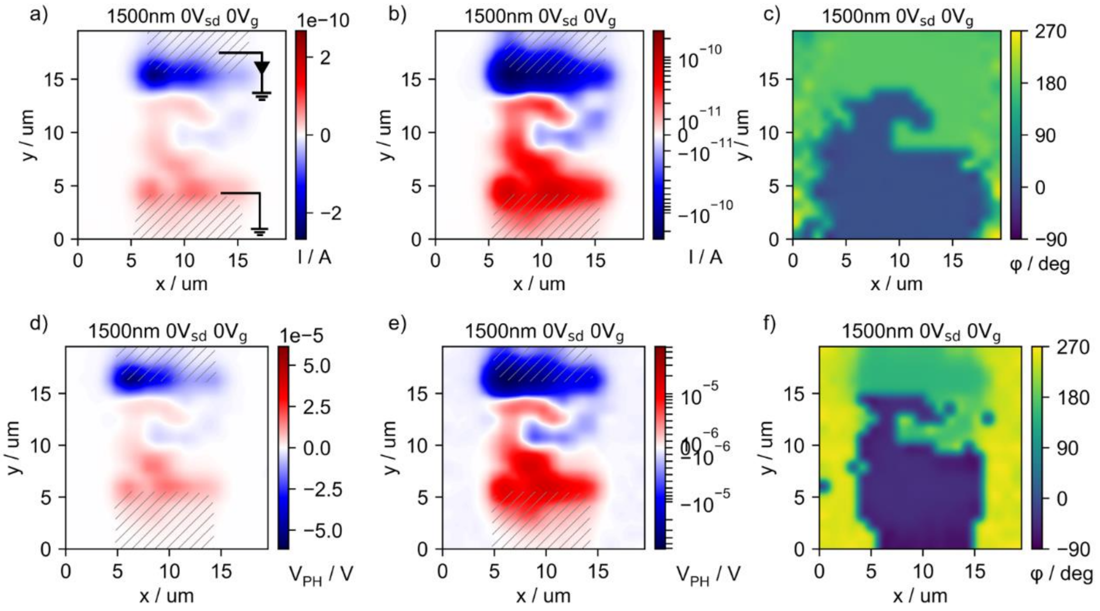

Figure 5.6: Scanning photocurrent and photovoltage imaging under short-circuit conditions at 1500 nm of the 10 µm device. (a-b) Photocurrent maps in linear and log scale, respectively. (c) Phase of the photocurrent signal. (d-e) Scanning photovoltage image in linear and log scale. (f) Phase of the photovoltage signal.

To further confirm the photothermoelectric origin of the photoresponse under short-circuit conditions, photovoltage maps were recorded on the device in the same setup but without a current preamplifier (**Figure 5.6**). Indeed, the measured photovoltage is on the order of tens of microvolts and agrees with the Seebeck coefficient difference of the SWCNT film and Pd electrode (S_{Pd} - S_{CNT}), assuming a temperature difference (ΔT) on the order of kelvin reported for CNT films and individual CNTs.[91],[88] In addition, a weak signal is still detected when the laser spot is illuminated away from the metal-CNT junction into the contact region, evidenced by the phase, photocurrent and photovoltage maps in **Figure 5.6,** confirming the photothermoelectric effect due to indirect heating of the CNT film underneath the metal contacts. The spatial extent of the photoresponse (photocurrent / photovoltage) signal depends on the heat diffusion in the metal and the distance of the laser spot from the channel gap.[141] In **Appendix A5**, photocurrent maps of an additional device (electrode gap ≈ 5 µm) are shown where the spatial extent of the signal deeper into the contact region is evident.

A final comment on why a photovoltaic picture cannot explain the presence of the observed long-ranged signals in the channel and signals at the contacts. The photocurrent is expected to be zero when the illumination is at the center of the channel due to the absence of built-in electric fields that are otherwise responsible for the photoexcited carrier separation at the metal-CNT contacts.[161] However, the measured open-circuit photovoltage is on the order of tens of microvolts from the photovoltage maps, whereas it is on the order of ≈100 mV for a photovoltaic effect.[162]

Next, the spectroscopic analysis (**Figure 5.7**) of the short-circuit photocurrent maps from **Figure 5.5** are discussed. The scanning photocurrent maps have regions with positive and negative real photocurrents, as indicated in the blue and red in **Figure 5.5**. The absolute quantities of the real photocurrents are integrated over the device area at each wavelength to obtain the integrated photocurrent spectrum shown in **Figure 5.7a**. The shape of the integrated photocurrent spectrum originates from the power spectrum of the supercontinuum source shown in **Figure 5.7b.** The extrinsic photoresponse was then obtained by normalizing the integrated photocurrent spectrum with the source spectrum in **Figure 5.7b**. The red dashed lines in **Figure 5.7c, d** indicate the mean value of the extrinsic photoresponse. The observed extrinsic responsivity is nearly wavelength-independent with contributions from metal electrodes and nanotube film. Since palladium has broadband, nearly flat absorption (14 – 20%) in the 1100 – 1800 nm range (see also **Chapter 4, Figure 4.8**), it is reasonable to assume that the nanotube film must also have a similar wavelength-independent response due to the nearly flat overall extrinsic responsivity (**Figure 5.7c-d**). A wavelength-dependent photoresponse would then mean a photothermoelectric effect as the PTE current is proportional to the absorbed power and therefore is wavelength-independent at constant absorbed power.

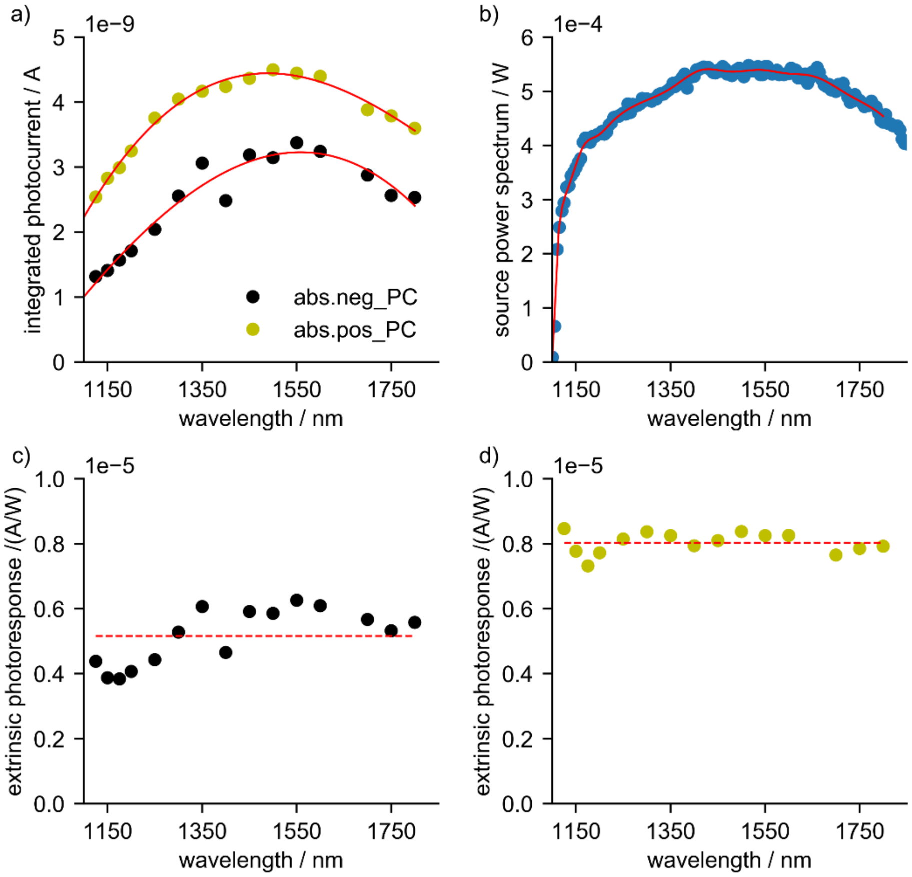

Figure 5.7: Spectroscopic analysis of the 10 µm device in short-circuit conditions. (a) Integrated photocurrent obtained from the scanning PC maps in Figure 5.5. The absolute quantity of the positive and negative real photocurrents is shown. (b) Calibrated source spectrum. (c,d) Extrinsic photocurrent obtained after the normalization of the integrated photocurrent with the source spectrum in (b).

It should be noted that it is challenging to extract the wavelength-dependence of the nanotubes alone in this device configuration since the wavelength-dependent absorption of the 300 nm-SiO_2/Si stack in the channel and at the metal contact is different. Additionally, in a nanotube network, due to the absence of any macroscopic alignment, the photoresponse in the channel is not sensitive to the polarization of light. A polarization-dependent photoresponse was observed in the case of macroscopically aligned films.[69] [92] A similar wavelength-independent behaviour was reported in MoS_2, where the above- and below-bandgap excitations resulted in identical photoresponse due to the light absorption in gold electrodes resulting in a photothermoelectric effect.[69] In the CNT films investigated here, the wavelength-dependence in the photoresponse near $\approx E_{11}^{S}$ was not investigated due to the lack of a strong light source in the E_{11}^{S} region.

5.4 Measurements under a source-drain bias

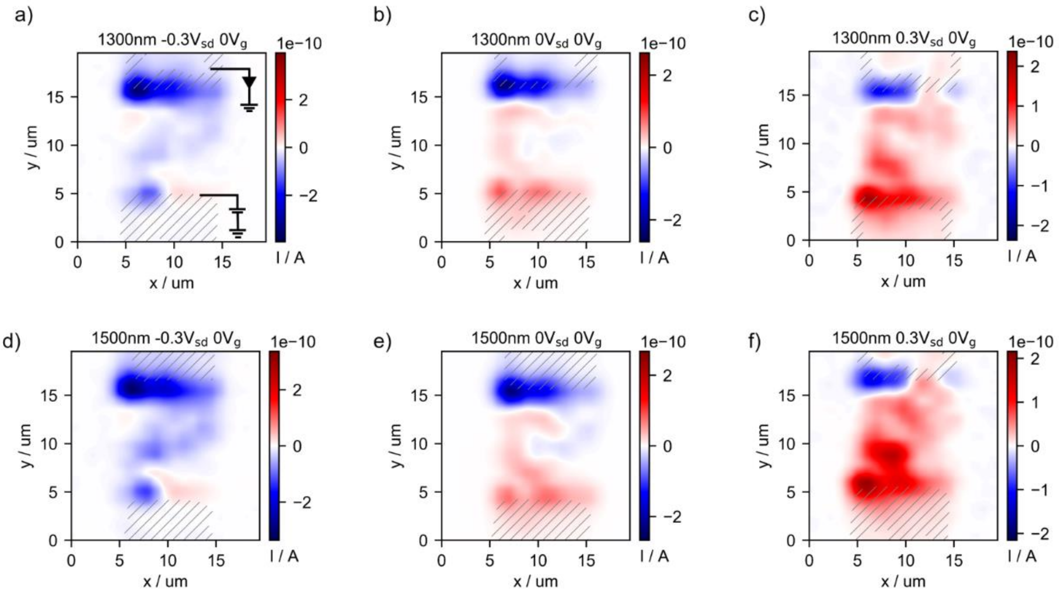

Figure 5.8: Scanning photocurrent imaging under a source-drain bias at 1300 nm and 1500 nm with a device of 10 µm channel length. The reflectance data were superimposed onto the photocurrent maps as grey shaded areas to indicate the position of the electrodes. (a-c) at 1300 nm with V_{sd} = -0.3V, 0V and 0.3V. (d-f) at 1500 nm with V_{sd} = -0.3V, 0V and 0.3V.

Next, the photoresponse under an applied source-drain bias is discussed in the following. In **Figure 5.8**, photocurrent maps at 1300 nm and 1500 nm are shown for -0.3 V and +0.3 V source-drain bias. The corresponding short-circuit PC maps at the respective wavelengths are also shown for comparison. In the biasing scheme, S-D bias is applied on the drain electrode and the source electrode is connected to the current preamplifier (**Figure 5.8a**). Since the lock-in technique is an a.c measurement mode, the change in current (ΔI) under illumination is the detected quantity. The polarity of ΔI is overall uniform throughout the channel region, with the photocurrent direction opposite to the dark current in the device. The direction of the photocurrent is independent of the polarity of applied bias with its direction opposite to the d.c current in the device. Therefore, under an applied source-drain bias and illumination, the total current in the device decreases. A similar unipolar photocurrent behavior in the channel has been previously reported for individual CNTs and networks.[163],[164] At the contacts, however, the photocurrent has contributions from both positive and negative real currents (blue and red colored regions), indicating possibly an electrothermal origin. Further, the photocurrent has similarities with the zero-bias condition (see for instance **Figure 5.8a, b**). A further indication is in the magnitude of the observed photocurrent which is identical in both the biasing conditions.

5.5 Measurements under a gate voltage in short-circuit condition

The gate voltage-dependent photocurrent study by DeBorde and co-workers on an isolated suspended single-walled semiconducting CNT discussed in **Chapter 2** is briefly recalled here.[88] Though the background discussion on single-tube device cannot be directly extended for the more complicated case of nanotube network, it still provides for a qualitative understanding of the gate dependence in photoresponse.

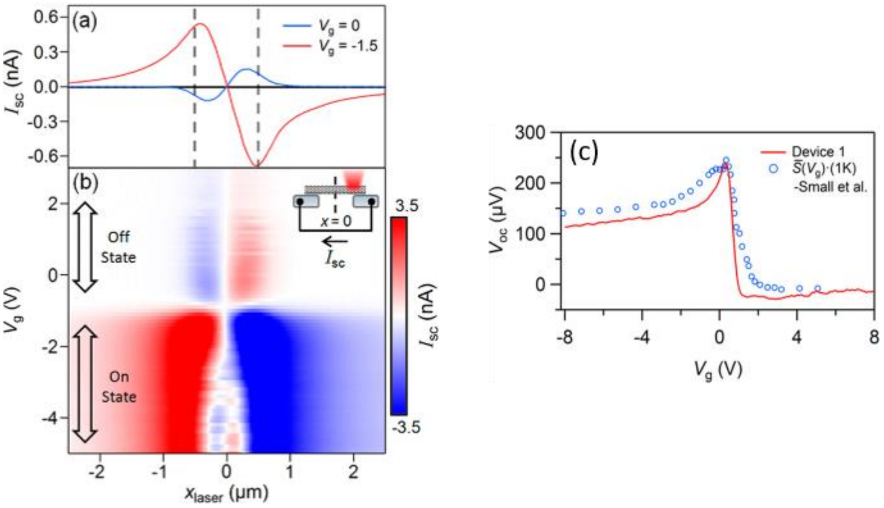

Figure 5.9: (a) Gate voltage dependent line scans of the short-circuit photocurrent (I_{sc}) in the device On state (V_g = -1.5 V) and Off state (V_g = 0 V). Dashed vertical lines indicate the electrode edges. The device scheme is shown in the inset of (b) with the device center at x = 0. (b) Gate voltage map: I_{sc} as a function of the gate voltage along the device x-axis. (c) In red shows the open-circuit voltage (V_{OC}) as a fuction of gate voltage measured at x = 1.8 μm. Open circles in blue represent the Seebeck coefficient from sc-SWCNT measured by Small et al.[89] Adapted with permission from from [[88]]. Copyright 2014 American Chemical Society.

Figure 5.9 shows the scanning photocurrent measurements conducted on suspended semiconducting CNTs by DeBorde et al. In their work, the gate dependence of the short-circuit photoresponse (photocurrent and photovoltage) I_{sc} was studied. In a particular gate voltage regime (in the device On state), a strong photocurrent signal extending several micrometers into the metal contact was observed. The origin of this photoresponse was attributed to a photothermoelectric effect (PTE), as discussed in the following. In **Figure 5.9a,** the line profiles $I_{sc}(x_{laser})$ for the device (inset in **Figure 5.9b**) are shown for the two gate conditions V_g = -1.5 V (On state) and V_g = 0 V (Off state) where the photocurrent is stronger in the On state and has an opposite polarity with respect to the Off state photoresponse. The complete gate voltage dependence of I_{sc} along the length of the CNT is shown in the photocurrent map $I_{sc}(x_{laser}, V_g)$ in

Figure 5.9b. It was observed that the photocurrent distribution and the magnitude are different in the device On state and Off state. Further, a strong photocurrent at the CNT-metal contact in the On state was observed due to heating in both the CNT and the metal contact. In the Off state, however, the heating in the metal does not contribute to a photocurrent. Instead, the observed photocurrent was due to a built-in field assisted photovoltaic effect at the contacts (details of the Off state photocurrent are discussed in **Chapter 2** Section 2.10). Since the On state photocurrent has contributions from metal and CNT, the discussion in this section is limited to the device ON state. **Figure 5.9c** shows the open-circuit voltage V_{OC} when the laser spot is located at a distance of x = 1.8 µm (illumination of the metal electrode, and not the CNT). The photovoltage increases and has a peak at the threshold gate voltage $V_g = 0$ V, and plateaus at more negative voltages and is almost zero in the device Off state. In their work, DeBorde et al. refer to the work of Small et al. to confirm the measured photovoltages in their device correspond to a PTE effect. Small et al. reported on thermoelectric measurements on substrate-supported SWCNTs and determined an effective Seebeck coefficient (S) for p-type SWCNT (open circles in **Figure 5.9c**). The open-circuit voltage (V_{OC}) and the temperature difference ΔT across the device is related by the following relation $V_{OC} = S(V_g)\Delta T$. The V_{OC} measured (in red) by DeBorde et al. agrees with the data from Small et al.[89] In their devices, DeBorde et al. estimate a ΔT of 1 K. Therefore, the observed spatial extent (≈ several micrometers from the contact edge) of the photocurrent into the metal contact in the On state can be explained by PTE effect.

Further deep into the On state ($V_g < -3$V), the additional polarity change (between x = -0.2 µm and x = 0.2 µm) observed is due to the spatially inhomogeneous doping across the CNT. This inhomogeneous doping is due to the band bending at the contacts in the On state. In the regions of CNT that are heavily doped (section of CNT in channel center) the Seebeck coefficient takes a smaller value and in the regions that are lightly doped (section of CNT at the contacts) the Seebeck coefficient is large. The open-circuit voltage for such an inhomogeneous system is given by the relation below.

$$V_{OC}(x_{laser}) = -\int S(x)\frac{dT(x,x_{laser})}{dx}\,dx$$

$T(x, x_{laser})$ is the profile of the temperature along the CNT as a function of laser position. For homogeneous Seebeck coefficient S(x), the net open-circuit voltage is zero.

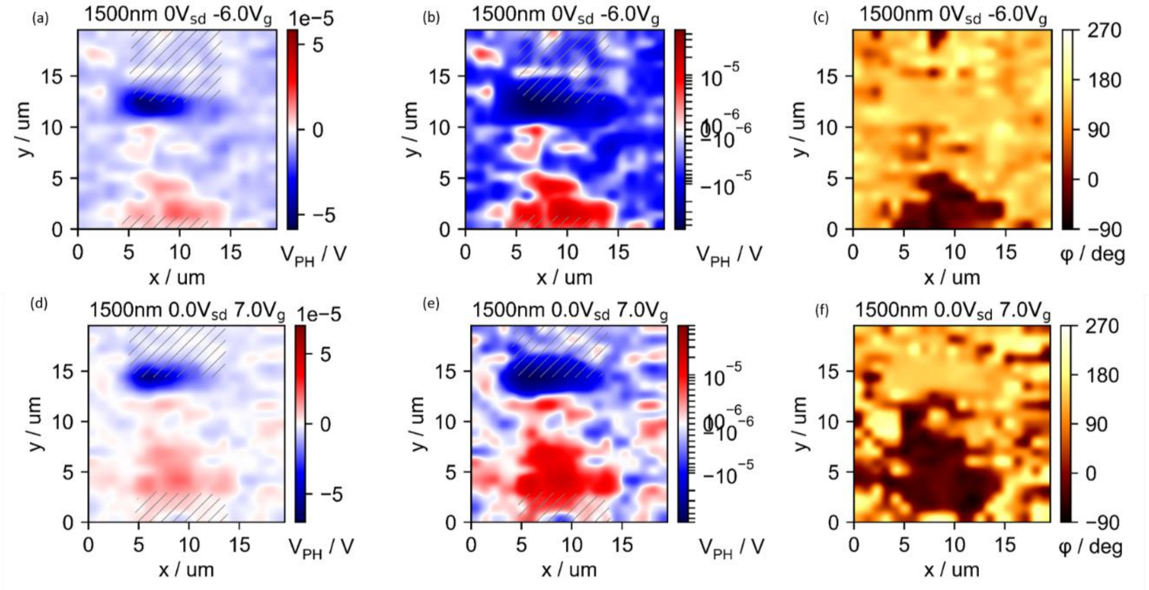

Figure 5.10: Scanning photovoltage imaging under different gate polarities at 1500 nm with a device of 10 µm channel length. (a,b) photovoltage maps under gate voltage -6 V shown in the linear and symlog scale. (c) corresponding phase map at -6 V. (d,e) photovoltage maps under gate voltage 7 V shown in the linear and symlog scale. (f) corresponding phase map at 7 V.

Figure 5.10 shows the scanning photovoltage maps recorded at 1500 nm under a gate voltage and zero source-drain bias. The measured photovoltage is on the order of tens of microvolts and the maximum in the signal is observed near the electrodes. The corresponding phase of the signal at the gate voltages -6V and 7 V is shown in **Figure 5.10c** and **Figure 5.10f**. The magnitude of the in-phase photovoltage and distribution near the electrodes are similar to that of the photovoltage maps discussed for the zero source-drain bias condition in **Figure 5.6**, where the measured photovoltages were attributed to a photothermoelectric effect. A similar photodetection mechanism therefore is also responsible for the measured photovoltages here under an applied gate voltage and zero S-D bias. Furthermore, from the previous discussion on single-tube devices, one would expect the photovoltage to have different polarities near the electrodes for the two gate voltage conditions (that is, in the device On-state and Off-states). However, the measured photovoltage at the electrodes seems to be independent of the gate polarity thus indicating a very weak or no gate dependence of the gate voltage on the Seebeck coefficient of the nanotube film. In the single-tube semiconducting device, there is a clear device-off state, and therefore a sign change in the photocurrent for the gate voltages in the on-state and off-state (on/off ratio = approx. five orders) was observed. On the other hand, in CNT film device discussed here, the on/off ratio is less than one order (< 8) in the measured gate voltage range, the low on/off ratio is likely due to the presence of residual metallic tubes in the network as discussed previously in **Section 5.2.** Barkleid et al. investigated the photocurrent behavior in suspended metallic single-tube device with split gates.[74] The scanning photocurrent imaging in the p-n junction configuration showed a large spatial extent of the photocurrent, spanning entire nanotube length. Further, a complex gate-dependence with a six-fold sign change in the photocurrent was observed (similar to the case of graphene, **Figure 2.12**) when the laser was focussed at the p-n junction interface as a function of dual gate voltages.

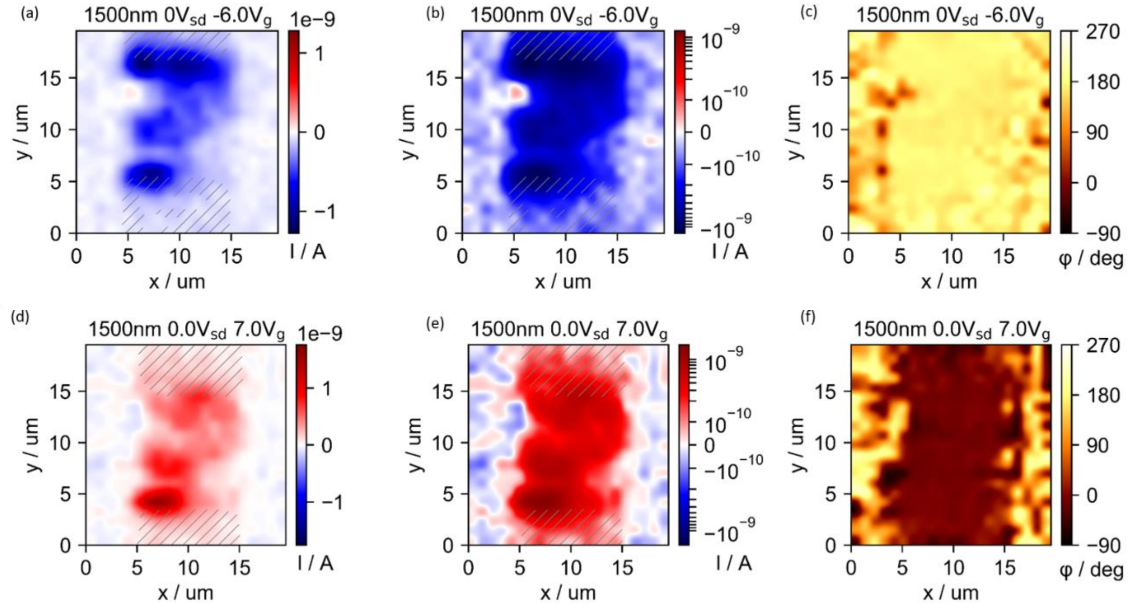

Figure 5.11: Scanning photocurrent imaging under different gate polarities at 1500 nm with a device of 10 µm channel length. (a,b) photocurrent maps under gate voltage -6 V shown in the linear and symlog scale. (c) corresponding phase map at -6 V. (d,e) photocurrent maps under gate voltage 7 V shown in the linear and symlog scale. (f) corresponding phase map at 7 V.

The **Figure 5.11** shows the complementary scanning photocurrent maps measured at 1500 nm under the same gate voltage conditions and zero source-drain bias similar to the photovoltage maps discussed in **Figure 5.10**. The measured photocurrents are on the order of nA and are unipolar depending on the polarity of gate voltage. For a negative (positive) gate polarity, a negative (positive) photocurrent is recorded (see **Figure 5.11a** and **Figure 5.11d**). The magnitude of the in-phase photocurrent is on the same order for both the gate voltages and the maximum in the signal being detected at the electrodes. The corresponding phase of the signal is shown in the maps in **Figure 5.11c** and **Figure 5.11f**. In contrast to the photovoltage maps, the observed photocurrent has the same polarity in the channel and at the contacts. The dependence of the sign of the in-phase photocurrent on the gate voltage polarity is unexpected. The in-phase photocurrent under a gate voltage could likely have an origin in the capacitive photocurrent effect in the CNT device. In the CNT channel, the total capacitance has two contributions that are in series with each other (**Figure 5.12**): the back gate or the oxide capacitance (C_{ox}) and the intrinsic capacitance of the nanotube, also known as the quantum capacitance (C_q) that has its origin in the finite density of states (DOS) of SWCNTs. The gate oxide capacitance is dependent on the geometry, and the dielectric constant of the oxide layer. On the other hand, in the quantum system like nanotube with a limited density of states at the Fermi level, the addition of new charges would require additional energy to occupy the higher electronic states.[165] This would in turn result in a change in the total capacitance in the form of quantum capacitance. The quantum capacitance of the single-tube devices has been experimentally demonstrated by Ilani et al.[165] The total capacitance is given by the relation: $1/C_{tot} = 1/C_{ox} + 1/C_q$.

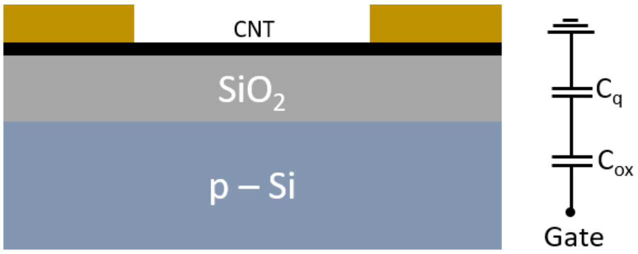

Figure 5.12: Schematic side view of CNT device indicating the oxide and quantum capacitance

Due to the local illumination and light absorption in the nanotube film, the charge carriers would hop on and off from the illuminated area and result in the change in the quantum capacitance of the film; resulting in an instantaneous change in the total device capacitance. Theses light-induced local carrier changes in the nanotube film are therefore detected as a capacitive photocurrent. The sign of this capacitive photocurrent is therefore dependent on the applied gate field direction. To detect a capacitive photocurrent, the nanotubes must be photoactive and should have an energy gap matching the energy of the incident light.

In addition, the underlying silicon substrate can also contribute to a photocurrent signal by photogating effect (topic of the next section). However, in the present case, the incident wavelength is well above the silicon bandgap (> 1100 nm) and where there is only doping-dependent free carrier absorption. Therefore, the silicon cannot contribute to photocurrent in this wavelength range.

5.6 Photogating in Silicon substrates

In this section, under an applied gate voltage and source-drain bias the photoresponse in silicon substrate is reviewed. The light induced gating (photogating) that is commonly observed at the semiconductor-insulator interface (Si-SiO_2) is described in the following. For the photogating effect to occur, first, silicon should be absorbing in the wavelength range of the measurement. Second, due to the modulation of incident light, an additional a.c gate voltage (δV) is generated because of the band bending at the interface, and an effective gate voltage (applied d.c + δV) is now experienced by the nanotube channel. Subsequently, the change in the current due to this light-induced gate modulation is then detected.

Photogating is observed in silicon substrates under illumination when used as a back gate electrode in the field-effect transistor (FET) configuration. The photogating effect manifests as a background signal and has been previously reported on scanning photocurrent measurements of CNTFETs. In a CNTFET, the gate electrode modulates the current flow in the nanotube channel. In addition to the applied gate voltage, the light absorbed in silicon modifies the channel conductance.

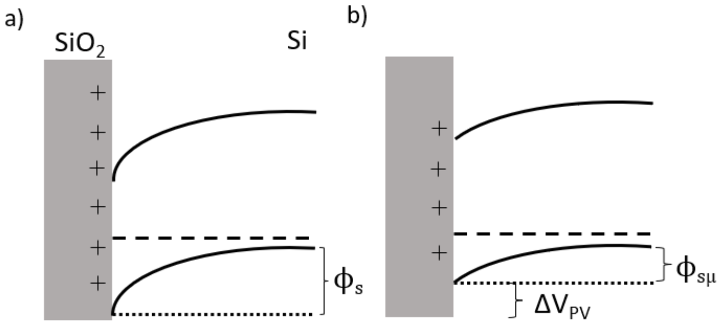

Figure 5.13: Band bending in p-type silicon substrate (a) without illumination (b) under illumination

Origin of photogating: At the interface of Si-SiO_2, due to interface states, mobile ions and charges in the oxide, the bands in the silicon are bent at the interface. The direction of band bending in silicon depends on the type of doping. **Figure 5.13** shows the band bending in p-type silicon. The light absorbed in silicon creates photoexcited carriers, and the e-h pairs are split by the built-in electric field at the interface. The trapped charges (electrons) at the interface modify the band bending as shown in **Figure 5.13b**.

In **Figure 5.13**, the surface potential in as-fabricated p-type silicon substrate before the illumination is $\phi_{S,}$ and it changes from ϕ_S to $\phi_{S\mu}$ under illumination due to the redistribution of carriers and subsequent trapping. The difference in the two potentials is measured as a surface photovoltage ΔV_{PV}. The magnitude of the measured photovoltage/photogating depends on the oxide thickness, level and type of doping in silicon. Higher doping levels lead to increased sub-gap free carrier absorption in silicon.[166] The electronic band bending/surface photovoltage at the SiO_2/p-Si interface has been characterized using core-level X-ray photoelectron spectroscopy (XPS) and at the SiO_2/p-Si interface, a downward band bending of -0.4 eV was reported.[167]

Using scanning photocurrent measurements, Marcus and co-workers, first reported on the photogating effect in individual SWCNTs.[168] Sczygelski et al. later studied the photogating effect in CNT films.[164] Their main findings are discussed in the following. The photoresponse from photogating is dominant for the excitation wavelengths at and below the silicon bandgap (bandgap ≈ 1100 nm). At those wavelengths, the photoresponse was observed between the electrodes; within and outside of the SWCNT channel region. Outside the channel region where CNTs are not present, the photoresponse originates from photogating in silicon substrate and a negative photoresponse was measured. The silicon substrate was n-doped, and due to the excess carriers generated in silicon under illumination, holes are accumulated at the oxide-substrate interface, thus depleting the carriers in CNTs (the CNT film is p-doped in the ambient conditions). The large diffusion length (≈ 100 µm) of the minority carriers in n-Si resulted in a spatial extent of the photocurrent signal even in the regions without CNTs. In another study by P. B. Selvasundaram (PhD thesis), a background signal due to photogating in the photocurrent responsivity was observed for the above and sub-band gap excitation for both the 300 nm and 800 nm SiO_2 thicknesses in SiO_2/p-Si substrate. The electrodes were bridged with a few tubes (< 10 tubes per µm width) using electric field assisted deposition. Replacing silicon with a sapphire substrate resulted in a photoresponse contribution from tubes alone and with no background signal from the substrate.

In the study of Sczygelski et al., the photogating from the silicon substrate gets weaker moving away from the bandgap of silicon as the photoresponse follows the absorption coefficient trend in silicon (at 1100 nm, $\alpha > 1\ cm^{-1}$ and at 1300 nm $\alpha < 0.1\ cm^{-1}$, α is the absorption coefficient). However, the absorption spectrum of silicon is strongly modified by its doping density due to free carrier absorption and is very different compared to an undoped sample. Hence, silicon becomes absorbing at photon energies lower than the bandgap for highly doped samples.[169] In the work of P. B. Selvasundaram, a p-doped silicon substrate with resistivity less than 0.005 Ωcm was used, and the doping density at this value is between 10^{19} to $10^{20}\ cm^{-3}$, and the absorption coefficient due to corresponding free carrier absorption was between $100 - 1000\ cm^{-1}$ in the wavelength range 1100 nm – 2000 nm. The magnitude and spatial extension of the photogating effect depends not only on the wavelength-dependent absorption coefficient of silicon but also on its doping density. For lightly doped silicon, the lifetime of the carriers is long, and therefore the signal strength and spatial extension is also large (centimeters). On the other hand, in heavily doped Silicon substrate, the carrier lifetime is shorter, but still the effect is observed locally (up to several micrometers from the channel region).[119]

In the CNT films prepared here on the p-doped silicon substrates, the resistivity of silicon is 0.05-0.2 Ωcm, and the corresponding doping density is between 10^{17} to 10^{18} cm^{-3}. The absorption coefficient due to the free carriers is then 1-10 cm^{-1} in 1100 nm – 2000 nm wavelength range. Hence, in addition to the CNTs, silicon is also photoactive at 1500 nm due to free-carrier absorption. To clearly quantify the individual contributions to the photoresponse from silicon substrate and CNT films separately, a device design modification would be required, for instance, making the electrodes wider (or reducing the width of the CNT film within the channel), this would then allow for the detection of photoresponse due to the substrate in the channel region where the CNTs are absent.

Chapter 6 Plamonic-photonic (PPhC) structures for light-matter enhancement in nanocarbon materials

Introduction

In Chapters 4 and 5, light detection from nanocrystalline graphite and carbon nanotubes were discussed. The complimentary light emission has also been demonstrated in the past.[18,37,170,171] However, as discussed in the preceding chapters, the intrinsic light-matter interaction of the nanocarbon materials (graphene and CNTs) is weak, and therefore for device applications, they must be integrated into optical or photonic crystal cavities. The integrated device architectures have been previously demonstrated for narrowband applications, where the photonic structure was tuned to a narrow wavelength band to match the emitter's absorption or emission spectrum.[172,173] On the other hand, structures with multiple optical resonances are advantageous for applications involving photoactive materials with a distribution of optical transitions (for instance, CNT films with a diameter distribution in the network as discussed in Chapter 5). In this chapter, the discussion is based on the local enhancements in the so-called plasmonic-photonic crystals (PPhCs), which combine the plasmonic resonances and the photonic guided resonances. These hybrid plasmonic-photonic resonances span the visible and near-infrared frequencies. The PPhCs were previously employed for fluorescence detection in biomarker molecules.[103–105,174] In this chapter, first, the fabrication of PPhCs with different structural parameters (lattice-distance between air-holes) using electron-beam lithography is described. The enhancement in the Raman signal of graphene transferred on top of the PPhCs is then discussed. The nature of the plasmonic-photonic resonances is understood from the complementary near-field and far-field simulations.

Contribution: I have fabricated the plasmonic-photonic structures and performed the Raman measurements.

6.1 Fabrication and design overview of PPhC structures

In the following, the design and fabrication of the plasmonic-photonic structures (PPhCs) is described. For the design implementation, as a starting point, the structural parameters (air-hole diameter (d) and lattice-parameter (a)) were chosen from the work of Iwanaga et al. targeting the visible and near-infrared resonances. Iwanaga and co-workers have extensively investigated the fluorescence detection in biomarker molecules using PPhC structures.[103,105,174] The optical resonances in the PPhC structure can be tuned by varying either the air-hole diameter or the lattice parameter. In the present work, the air-hole diameter was fixed, and the lattice parameter was tuned for the visible and NIR resonances. As a function of increasing lattice parameter, the optical resonances are red-shifted in wavelength. The PPhC structures were fabricated on silicon-on-insulator substrates.

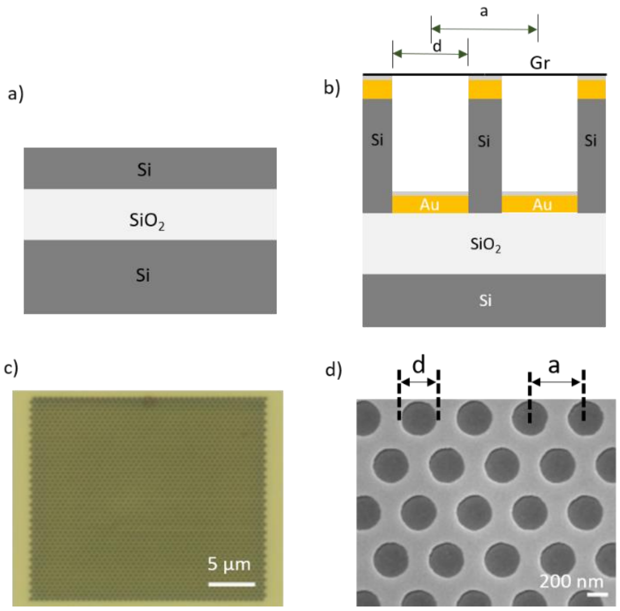

Figure 6.1: (a) Side view scheme of silicon-on-insulator (SOI) stack with 250 nm-Si/3000 nm-SiO_2/p-Si SOI. (b) Side view scheme of the PPhC structure obtained by etching air-holes into the top silicon layer of the SOI stack followed by gold layer deposition. (c) Optical micrograph of the fabricated PPhC field. (d) SEM micrograph (top view) of the PPhC structure. The lattice distance is represented as **a**, and the air-hole diameter is represented as **d**.

Figure 6.1a shows the side view scheme of the silicon-on-insulator (SOI) substrate. The SOI stack consisted of 250 nm p-Si/3000 nm-SiO_2/p-Si. The plasmonic-photonic structures (PPhCs) were fabricated on the SOI stack using electron-beam lithography as described below. First, the proximity effect correction was implemented by adjusting the electron dose distribution in the photonic crystal design using Raith Nanosuite software. The proximity effect correction ensures that every point in the high-fidelity design receives a similar electron dose and therefore results in precise control over the air-hole diameters in the fabricated photonic structures (see **Figure 6.1d**). For the e-beam lithography, a thick PMMA resist (**Table 6.1**) was spin-casted onto the SOI substrate, with the resist acting also as an etch mask for the subsequent silicon etching step. After the e-beam exposure, the resist was developed in a cold solution of MIBK and isopropanol in one part to three parts mixture and then soft baked at 90 ˚C on a hot plate for one minute. In the second step, silicon was etched in the regions defined by lithography by reactive ion etching (RIE) (see **Table 6.1** for the etching recipe), and the resulting air-holes are 250 nm deep (see **Figure 6.1b**). In the third step, a 35 nm gold layer was deposited by electron beam evaporation. Finally, a 5 nm Al_2O_3 dielectric spacer was deposited using atomic layer deposition. **Figure 6.1c** shows the top view optical micrograph of a single PPhC field, several such fields with varying lattice distance (from 470nm to 590 nm in 30 nm step size) and fixed air-hole diameter (310nm) were fabricated in the same SOI substrate. Finally, graphene was transferred onto the fabricated PPhC. The graphene transfer was carried out in the group of Prof. Martin Kalbac, at the J.H Institute of Physical Chemistry, Prague.

Table 6.1: Plasmonic-photonic structure fabrication parameters.

Parameter	Plasmonic-photonic structure
PMMA resist	950k, A8.0, 8000 rpm
E-beam litho.	30 kV proximity corr.
Development	cold (0 °C), MIBK:ISO 1:3
PMMA Etch mask thickness	~ 700 nm
Silicon etching	30sccm CHF_3, 14sccm SF_6, 5sccm O_2, 15mTorr, 100W
Etching time	3 minutes
Au film deposition	2 nm Ti (0.003 nm/s), 35 nm Au (0.06 nm/s)
Al_2O_3 layer (ALD)	5nm Al_2O_3, 130°C TMA/H_2O (83 cycles)

6.2 Description of PPhC resonances

In this section, the qualitative nature of the near-infrared PPhC resonances is described by considering a PPhC structure with fixed air-hole and lattice diameter. An example of PPhC with resonances in the telecommunication spectral region is considered in the following. As it will be explained below, not all of the resonances can contribute to an enhancement near the top interface (where we would like to have an emitter) of the PPhC structure. The near-field simulations for this example were performed using COMSOL software by Aimi Abass at INT, KIT.

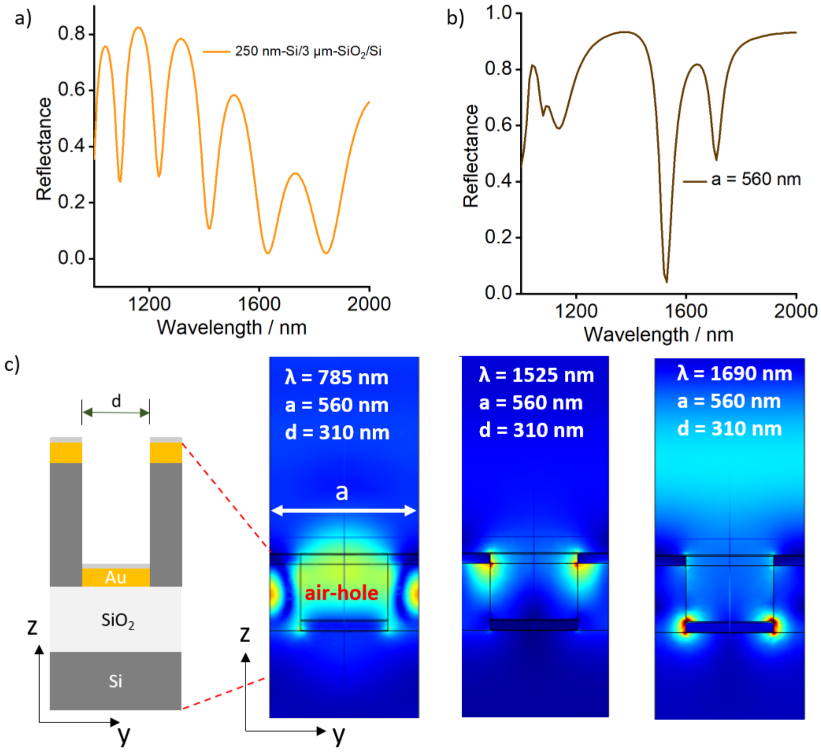

Figure 6.2: (a) Calculated reflectance under normal incidence of the (SOI) stack with 250 nm-Si/3 µm-SiO$_2$/p-Si. (b) Calculated reflectance under normal incidence of the plasmonic-photonic structure (**Figure 6.1b**) with air-hole diameter 310 nm and lattice distance 560 nm. (c) Side view scheme showing one air-hole and the corresponding side view near field maps showing the regions of E-field enhancement at 785 nm, 1525 nm, and 1690 nm. The dashed red lines indicate the top and the bottom surface in the PPhC structure.

The resonances in the PPhC structures can be understood from **Figure 6.2** which summarizes the far-field and near-field wavelength-dependent optical response. The reflectance from a planar SOI stack is also shown for comparison. **Figure 6.2a** shows the calculated wavelength-dependent reflection under normal incidence in a multilayer planar SOI stack for the layer thicknesses described in **Figure 6.1a**. The dips in reflectance are due to the multiple reflections at SiO$_2$–Si interfaces. On the other hand, nano structuring the SOI substrate strongly modifies the far-field reflection (see **Figure 6.2b**). In **Figure 6.2b**, the calculated reflectance under normal incidence in a PPhC structure with the lattice distance of 560 nm and air-hole diameter of 310 nm is shown. It can be seen that the number of dips in the reflection are now reduced, and the dip near ≈ 1600 nm is now even stronger. Since the dips in reflection correspond to the localized light absorption in PPhC nanostructures, the absorption A is then related to reflection by, A = 100 - R% for the condition of zero transmission.[105]

Indeed, the field enhancements due to the local absorption can be visualized from the near-field maps shown in **Figure 6.2c.** The schematic shows the side view (z-y slice) of a single air-hole. The side-view near-field enhancement profiles for the three resonance modes at 785 nm, 1525 nm, and 1690 nm are shown. The three modes have distinct local absorption in the structure, with the 785 nm mode resulting in field enhancement within and above the air-hole, the 1525 nm mode resulting in the field enhancement at the corners (near the rim) of the top gold layer. In the 1690 nm mode, the enhancement is near the corners of the bottom gold layer. The optical signal of a fluorophore/scatterer is enhanced when the incoming (excitation) or the outgoing (emission/scattering) wavelength is in resonance with one of the plasmonic-photonic modes. However, it should be noted that in the case of planar 2D scatterer like graphene, the modes from the bottom gold layer (that are 250 nm below the surface) can contribute only very weakly to a signal enhancement. Furthermore, the guided modes that are confined entirely to the silicon photonic crystal also cannot result in an enhancement at the surface. With this background on PPhC resonances, the Raman measurements of graphene on PPhC structures can be understood.

6.3 Raman measurements

The Raman spectra were measured using laser excitation lines 532 nm and 785 nm. **Figure 6.3b** shows the Raman spectrum of graphene on a PPhC structure under 785 nm excitation. The Raman spectra were acquired on PPhCs with different lattice parameters as described in **section 6.1**. The Stokes-shifted scattered wavelengths corresponding to the D, G and 2D peaks for the 532 nm and 785 nm excitation are indicated in **Table 6.2**. The numerical aperture (NA) of the objective used was 0.85 (100x). The signal acquisition time was for 60 s.

Table 6.2: Stokes wavelengths corresponding to the Raman scattered light in graphene.

Laser excitation	D-peak	G-peak	2D-peak
532 nm	573 nm	581 nm	621nm
785 nm	875 nm	896 nm	986 nm

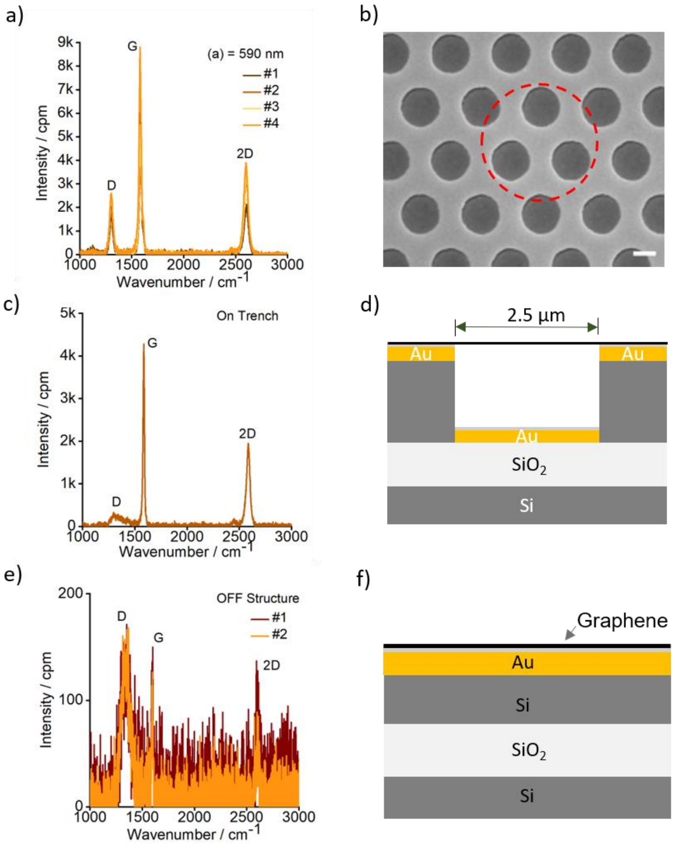

Figure 6.3: (a) Raman spectrum of graphene on a PPhC with a = 590 nm, and d = 310 nm. (#) indicates the signal at different sites on the PPhC. (b) SEM image of the PPhC structure from the Figure 6.1d. (c) Raman spectrum of graphene on suspended graphene over a 2.5 µm wide trench. (d) Side-view scheme of the trench. (e) Raman spectrum of graphene on supported graphene Au-SOI stack. (f) Schematic of the planar stack.

Figure 6.3 shows the Raman spectra for three different substrate configurations as described in the following. The corresponding substrate top view and side view schemes are shown next to the Raman spectra. The Raman spectrum on a representative PPhC with a lattice parameter of 590 nm and air-hole diameter of 310 nm is shown in **Figure 6.3a**. The prominent, D, G and 2D peaks signature of graphene are distinguished. In the PPhC structure (top view, **Figure 6.3b**), the Raman intensity in the regions of suspended (on the air-hole) and the supported (on flat metal, outside the air-hole) graphene can be very different. Therefore, the Raman signal for the suspended and supported graphene was measured independently: (i) by realizing a trench of 250 nm deep and

2.5 µm wide in the SOI stack and depositing a 35 nm gold layer (see **Figure 6.3d**), the corresponding Raman spectrum of the suspended graphene layer from the trench is shown in **Figure 6.3c**. (ii) on the SOI substrate with Au layer on the top, where the graphene layer is supported on the substrate (**Figure 6.3f**), the corresponding Raman spectrum is shown in the **Figure 6.3e**. Inferring from the **Figure 6.3c** and **Figure 6.3e**, it can be concluded that the Raman signal is strongly enhanced in the case of suspended graphene while it is suppressed when the graphene is supported on the substrate. The suppressed signal in the supported case is expected since the graphene on gold layer is only weakly absorbing in the visible spectral region.[175] This implies that even in the case of PPhC structure, the regions outside the air-holes where the graphene is supported by the substrate should result in a signal suppression, while in the air-holes where the graphene is suspended should contribute to the enhancement.

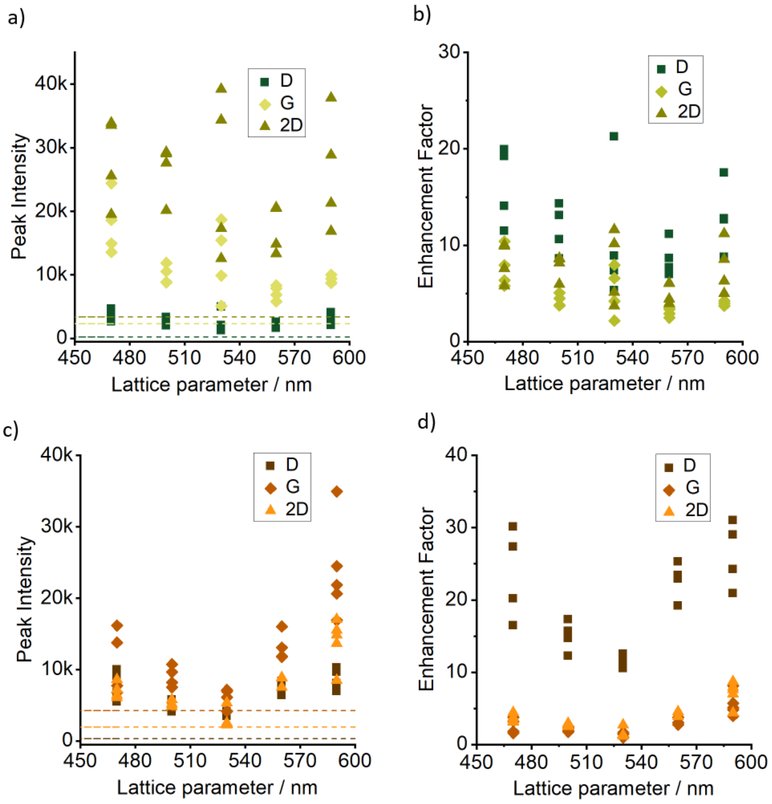

Figure 6.4: (a) Fill-factor (FF) normalized peak intensities of the D, G and 2D peaks as a function of lattice parameter for 532 nm laser excitation. The dashed lines indicate the corresponding peak intensities for the case of suspended graphene (**Figure 6.3d**). (b) Enhancement factor obtained after normalizing the FF-normalized peak intensities with that of the suspended graphene. (c), (d) for 785 nm excitation.

Therefore, a suitable reference must be considered while evaluating the enhancement factor from the PPhC structure to avoid overestimation of enhancement factors. Usually, a flat substrate like bare silicon is chosen as a reference, but this may always not be an appropriate reference due to the strong signal suppression at the planar surface. Instead, in this work, the signal from the suspended graphene (trench signal) is chosen as a reference.

Considering that only the air-holes contribute to the signal enhancement in the plasmonic structures, the peak intensities of D, G, and 2D peaks obtained from the plasmonic-photonic structures with different lattice parameters were normalized with their corresponding fill-factor of air-holes using the fill-factor for hexagonal lattice arrangement. In **Figure 6.4a** and **Figure 6.4c**, the fill-factor normalized peak intensities under 532 nm and 785 nm excitation are shown. The spread in the data of the individual peak intensities correspond to the data measured at multiple sites on the same plasmonic-photonic structure. The D, G and 2D peak intensities from the suspended graphene on a trench are shown by the dashed lines. By normalizing the fill-factor normalized peak intensities with the corresponding peak intensities from the suspended graphene the enhancement factors were obtained as shown in **Figure 6.4b** and **Figure 6.4d**. The enhancement in the Raman signal was observed for all the peaks and the signals were enhanced up to 30 times. Overall, the observed enhancement factors for all the Raman peaks show a weak lattice parameter dependence (**Figure 6.4b** and **Figure 6.4d**). On the other hand, the D peak in **Figure 6.4d**. can also have contribution from the defects introduced in graphene during the transfer process. To probe the independent contributions locally would require nanoscale mapping of Raman intensities on top of the air-hole and is unfortunately not possible in the current experimental setup. The signal enhancements in **Figure 6.4a** and **Figure 6.4c** can be understood by considering the far-field reflectance spectra of the PPhC structures. From the earlier discussion in **section 6.2**, the signature of the field enhancements due to the PPhC resonances is present in the reflectance spectrum. The simulated reflectance (simulation details are discussed in section 6.3) under normal incidence in the 500 nm – 1000 nm spectral region for different lattice parameters is shown in **Figure 6.5**. The reflectance spectra consist of multiple reflection dips, and the solid vertical lines shown in green and red at 532 nm and 785 nm indicate the laser excitation wavelengths, respectively. The corresponding D, G, and 2D wavelengths of the scattered light (see **Table 6.1**) are indicated in dashed vertical lines. The plasmonic-photonic modes in the reflectance spectrum near these wavelengths give rise to the observed enhancements in the Raman signal. Next, the observed local minima in the Raman peak intensities in **Figure 6.4c** near the 530 nm lattice parameter is discussed. For this lattice parameter, considering the reflectance dip at ≈ 900 nm in **Figure 6.5c**, one would expect a strong signal enhancement for the G and 2D peaks due to the sharp reflectance dip. However, the appearance of the minima in the Raman signals is not surprising since this effect is likely related to the large

NA objective used in the Raman measurements. A large NA objective was used in experiment to record Raman spectrum locally at multiple sites on the small area photonic fields (area ≈ 24 µm x 24 µm). The reflection dips in **Figure 6.5** too therefore will be blue-shifted with the increasing angle of incidence (condition of non-normal incidence).[176] For instance, in the reflectance spectra of SOI photonic structure with air-holes, a measured blue-shift of up to 30 nm was reported for around 18 degrees change in the angle of incidence.[177] See also discussion in **Section 6.3**.

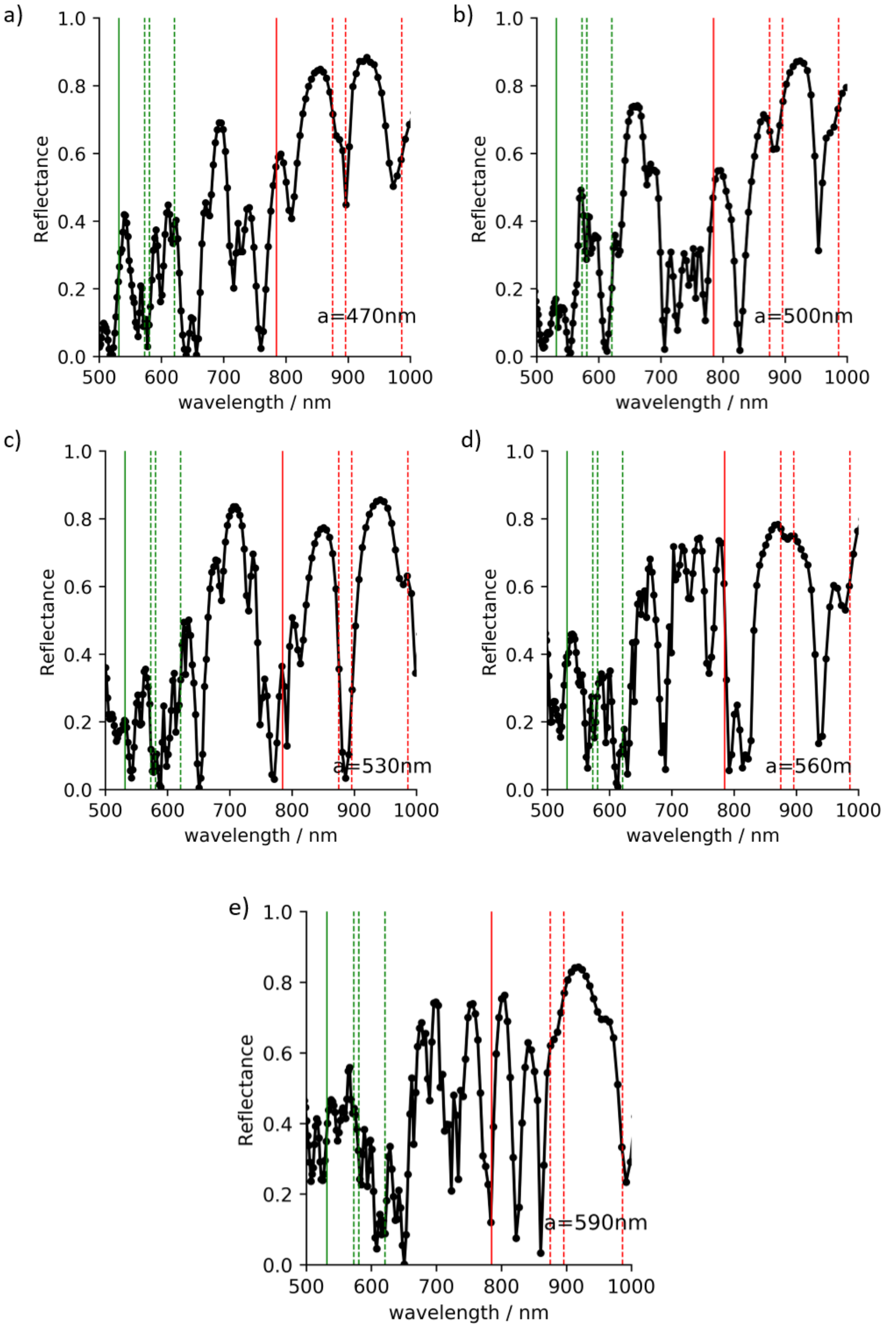

Figure 6.5: (a)-(e) Simulated reflectance spectrum of PPhCs under normal incidence for different lattice parameters. The solid vertical dashed lines indicate the 532 nm and 758 nm laser excitation and the dashed lines indicate the respective D, G and 2D Raman scattered light (see **Table 6.1**)

6.4 Simulations of PPhC

From the previous section (**Figure 6.3**), it was understood that the suspended graphene near the air-hole should result in an enhancement whereas the supported graphene should result in a signal suppression. Indeed, the simulated electric-field in the near-field maps at the surface of the plasmonic-photonic structure confirms this.

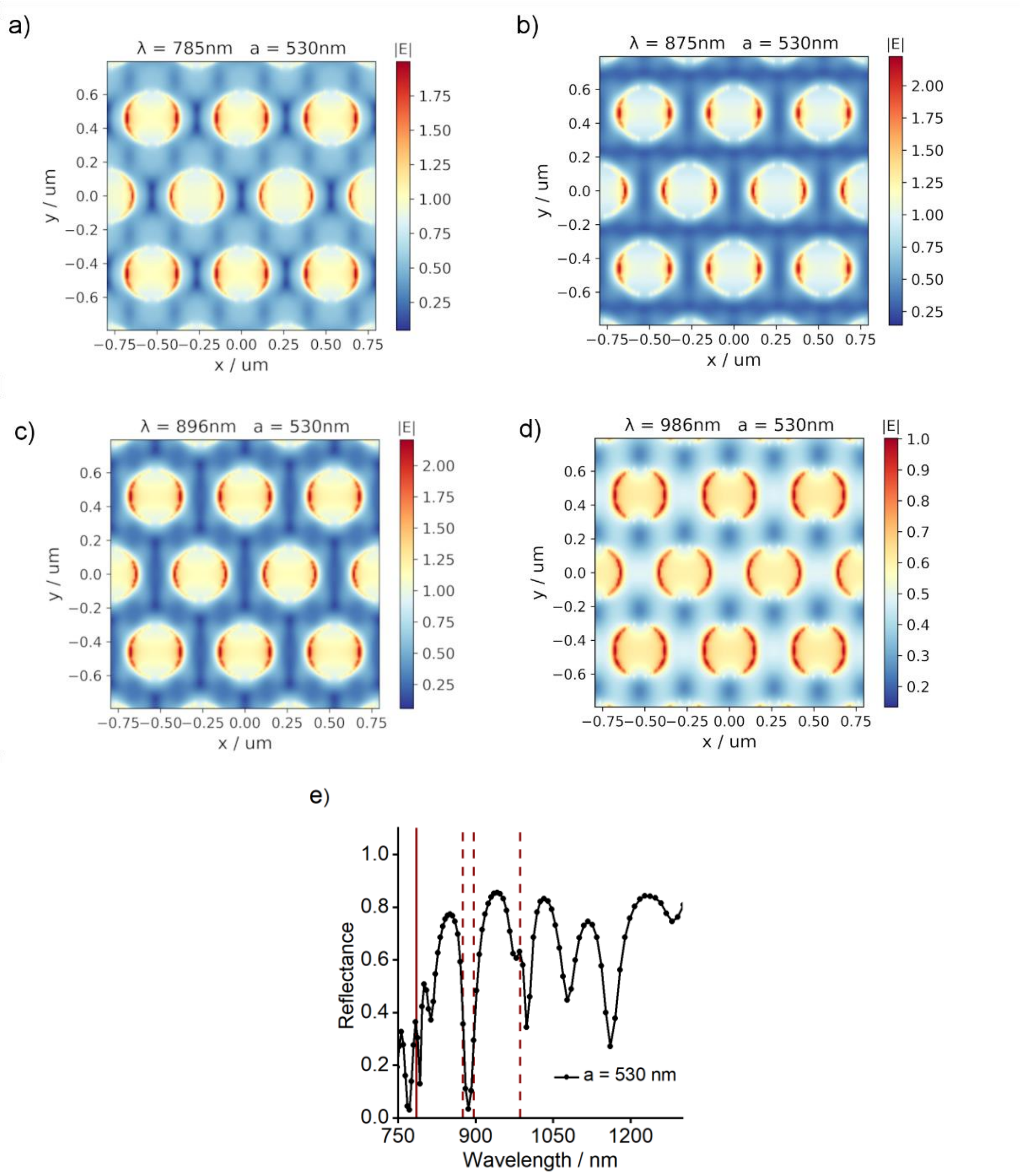

Figure 6.6: The near-field maps showing the electric-field distribution (E-field amplitude w.r.t the incident E-field amplitude) at the top of the plasmonic-photonic structure in the x-y plane (See also Figure 6.3b for the corresponding top view SEM image) for the structure with the 530 nm lattice parameter and the air-hole diameter of 310 nm. The near-field maps under normal incidence in xz plane with p-polarization and incident electric field amplitude of 0.5 are shown for (a) laser excitation wavelength of 785 nm (b) at the D peak near 875 nm (c) at the G peak near 896 nm (d) at the 2D peak near 986 nm. (e) Reflectance of the plasmonic-photonic structure under normal incidence. The dashed lines indicate the laser excitation, D peak, G peak and the 2D peak, respectively.

The FDTD simulations were performed using the MEEP software package on a remote eight-core CPU by Juan Ramon at INT, KIT. From the simulations, the complementary near-field maps and the far-field reflectance spectra were obtained. As described previously, the maximum in the local field enhancements in the near-field maps is encoded in the far-field reflectance spectra. **Figure 6.6** shows the representative near-field maps of the plasmonic-photonic structure with a lattice parameter of 530 nm and air-hole diameter of 310 nm. The near-field maps were obtained at the wavelengths of laser excitation, D-peak, G-peak, and 2D peaks (see **Table 6.1**) by plane wave illumination. The simulations were performed with a p-polarized plane wave source and the amplitude of the incident electric field in the simulation was 0.5. The maximum in the electric field with respect to the incident field is observed at the edges of the air-holes, while between the air-holes (on the metal surface), the electric field is suppressed. This behavior is similar for excitation at the four wavelengths (See **Figure 6.6a-d**). The local field enhancement or absorption would mean a dip in the reflectance (R). The reflection dips corresponding to the laser excitation, D, G and 2D peaks are shown in **Figure 6.6e** as the dashed lines. The R dip near 900 nm is responsible for the D and G peaks. The R dip responsible for the 2D peak near ≈ 985nm is shallow compared to the other dips (at 785nm, D, G peaks) and therefore the corresponding near-field enhancement is reduced. The near-field maps for the photonic structures with other lattice parameters at the fixed air-hole diameter of 310 nm are shown in the **Appendix A6.** The near-field enhancements for different lattice parameters are in the same range as discussed for the example in **Figure 6.6.**

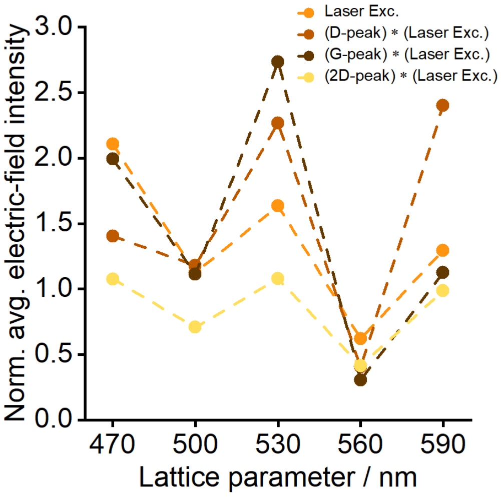

Figure 6.7: Averaged electric field intensity at the top of the plasmonic-photonic surface for 785 nm laser excitation obtained by integrating the local electric field amplitude in the near-field maps (maps for a = 530 nm are shown in **Figure 6.6**). The electric field is integrated over the entire area including the region between the air-holes. The normalized electric-field intensity as a function of lattice parameter is plotted for the laser excitation, and the product of laser excitation and (D, G, and 2D) peaks (see text for the description).

The **Figure 6.7** shows the averaged electric field intensities on top of the plasmonic-photonic structure as a function of lattice parameter obtained by integrating the local electric field amplitude from the near-field maps. Since the total enhancement has two contributions: excitation and scattering, the product of electric-field intensities of the laser excitation and the excitation at wavelengths corresponding to the D, G and 2D peaks is shown in **Figure 6.7**. The near-field maps for lattice distance a = 530 nm and air-hole diameter d = 310 nm are shown in **Figure 6.6.** The near-field maps for other lattice parameters are shown in Appendix A6. In the following, **Figure 6.6** is considered to explain why the averaged electric field intensities in **Figure 6.7** may underestimate the actual enhancements from the PPhC structure discussed in **Figure 6.4c**. Though the near-field maps give the local E-field distribution, the direct comparison of the field enhancements with the measured enhancements is not meaningful because the near-field maps are obtained under normal incidence whereas the Raman measurements were conducted using an objective with large numerical aperture (NA = 0.85). Therefore, the contribution from the non-normal incidence/excitation and the light scattered at large angles (angle-averaged) should also be incorporated into the simulations while calculating the overall enhancement factors. Furthermore, the simulated reflectance shown for normal incidence **Figure 6.7e**, in reality would result in a blue shift in the R-dips when measured with a high NA objective due to the non-normal incidence. Additionally, the excitation and scattering events must also be treated separately for the estimation of the overall enhancement factors. For instance, in the work of Yekani et al. the Raman scattered light from the graphene layer (1 nm above suspended Germanium substrate) was simulated by treating graphene as an in-plane dipole emitter radiating power into the upper half space.[62] On the other hand, for the excitation condition, a plane wave illumination was considered. The total enhanced signal therefore is the product of the two contributions.

Chapter 7 Summary

The present work focused on the advancement of scanning near-infrared spectroscopy to investigate photodetection in nanocarbon materials. In the recent years, considerable efforts have been devoted to realize wafer scale in-situ synthesis and growth of nanocarbon and other 2D materials for optoelectronic device applications. In this work, nanocrystalline graphite (NCG) and single-walled carbon nanotube (SWCNT) networks were synthesized directly on dielectric substrates without involving intermediate transfer processes. The potential of nanocarbon materials for broadband near-infrared photodetection was explored by studying the local photoresponse behavior using scanning photocurrent spectroscopy. The setup was first optimized for acquiring near-infrared spatial photocurrent mapping. In NCG devices, to maximize broadband absorption in the near-infrared, the layer thicknesses of NCG and SiO_2 were optimized by using the complementary light-field simulations. In SWCNT photodetection, the broadband NIR response was tailored by the diameter distribution of CNTs in the network.

The specific findings from the near-infrared photodetection studies from the nanocarbon materials are summarized in the following.

In Chapter 3, particular emphasis was laid on the scanning photocurrent experiment description. The following are the main improvements implemented in the scanning photocurrent setup: The setup was improved and optimized for conducting near-(NIR) to short-wavelength infrared (SWIR) scanning photocurrent imaging. The setup development included a concentric setup built-up to reduce thermal drifts due to the ambient temperature changes. The NIR supercontinuum light source spectrum after the acousto-optic tunable filter (AOTF) consisted of strongly wavelength-dependent fine structures. The source spectrum was therefore calibrated by implementing a wavelength-specific intensity modulation to result in a smooth wavelength dependence. For diffraction-limited NIR photocurrent imaging, the chromatic aberration of the setup was corrected for the NIR wavelengths, resulting in axial chromatic focus shifts up to 60 µm.

In Chapter 4, spectrally-flat broadband photodetection in the near- to short-wavelength infrared was realized with transfer matrix simulation optimized nanocrystalline graphite on SiO_2/Si substrates. Up to 60% of the incident light is absorbed in the thickness optimized NCG layer in the 1100 nm – 2100 nm spectral region. under a source-drain bias, entire channel region was photoactive, and the photodetection mechanism was attributed to heating-induced bolometric effect in the NCG. The measured flat intrinsic responsivity was not only limited to the above wavelength range and can be extended to other parts in the electromagnetic spectrum by suitably adjusting the layer thickness of NCG and SiO_2. The spectrally flat optimization was possible because of the absorptance of graphite is wavelength-independent up to 30 nm thickness (≈ 87 layers). Compared to previous works with thin NCG, the bolometric photoresponse at low source-drain bias is nearly two orders of magnitude larger. Further improvements in the responsivity can be easily realized by device modifications as described in the outlook section below.

In Chapter 5, the large-area, large-diameter SWCNTs networks grown directly on the SiO_2/p-Si substrate with a diameter distribution tuned for NIR light absorption were investigated. Since single-tube devices have a very weak absolute absorption, networks or films are required to boost the absorption for practical photodetection applications. The diameter distribution and the electronic type of the SWCNTs in the network were studied by multi-wavelength Raman spectroscopy using the radial breathing mode (RBM) frequency; a diameter distribution of 1.1 nm – 2.1 nm was confirmed from the Raman data analysis. The Raman spectra show an enrichment of the semiconducting-SWCNTs in the network, with a signature of metallic-SWCNTs still being detected. The spatial photocurrent and photovoltage distribution, with a nearly-flat spectral response, indicate a photothermoelectric origin of the zero-bias photoresponse. The spectral response in the 1100 nm – 1800 nm spectral region confirms the broad E_{11} peak expected for a broad-diameter distribution of the SWCNTs in the network. These SWCNT networks are, therefore, suitable for broadband NIR photodetection. The metallic content and the tube-tube junctions in the CNT networks could limit the photodetection efficiency. The aligned SWCNT networks, however, would further enhance the photoresponse as the intertube junctions are minimized, and further, a polarization-dependent photoresponse could be tailored.

In the chapter 6, plasmonic-photonic (PPhC) structures with optical resonances in the visible and near-infrared spectral region are described. By adjusting the structural parameters of the PPhC structure; lattice parameter and air-hole diameter, the spectral position of the resonances was tuned for the enhancements in vis-NIR spectrum. The near-field local enhancements and the far-field reflectance of the resonances were investigated using complementary near-field and far-field FDTD simulations. The Raman enhancement of graphene transferred on the PPhC structures was then studied using multi-wavelength laser excitation. The enhancement factors up to 30 were reported.

In conclusion, the results described in the above chapters show that by tailoring the optical properties of nanocarbon materials the photoresponse can be optimized for braodband detection in the near-infrared spectral region. The scanning photocurrent technique is advantageous as the photocurrent generation mechanisms can be directly deduced from the local photocurrent distribution. Furthermore, the technique is particularly useful in characterizing substrate-supported CNT networks (directly grown) that are otherwise difficult to characterize by absorption spectroscopy due to the strong signal domination from the underlying substrate. By extending the photocurrent spectroscopy to the visible spectral region, the full absorption spectrum of the CNT networks can therefore be reconstructed.

Outlook and Future work

For optoelectronic applications, devices from nanocrystalline graphite have the following advantages over some of the 2D materials discussed in **Table 4.2**; large photoactive device areas, ease of large-scale fabrication, thickness-controlled growth on desired substrates, and use of non-toxic materials. However, a few important challenges still have to be addressed to make the NCG devices marketable and competitive to the current state-of-the-art infrared detectors, including the improvements in photoresponsivity and detection of low light signals.

The local electric field determines the bolometric response as discussed in connection to **Figure 4.6**, and the response is dominated by the regions of high resistance, implying that the device design and geometry influences the photodetection performance. The bolometric response can be maximized in the center of the channel region, away from the metal electrodes, by creating a bow-tie-shaped channel. The applied source-drain bias would then drop mainly across the narrow region of the NCG channel rather than at the wide NCG-metal contacts. Riaz et al. realized such a structure to maximize the photocurrent from the NCG in the channel constriction.[37] Further improvements in the photoresponsivity can be achieved by suspending the NCG layer. As shown in the **Figure A7** (see Appendix) suspending NCG in a gold back reflective geometry would result in near unity absorptance in a very wide spectral range. Besides, the thermal sinking to the substrate can be reduced and a high ΔT in the NCG film can be reached.

As described in chapter 4, the detectivity of NCG is rather very low when compared to the other NIR detectors, it is on the order of 10^6 Jones. Therefore, for the detection of low light signals the detectivity of NCG devices is insufficient.

$$D^* = -\frac{\alpha \cdot t}{l}\sqrt{\frac{V}{2 \cdot q \cdot t \cdot \rho}}$$

The specific detectivity D^* can be expressed in terms of NCG properties (resistivity ρ and temperature coefficient of resistance α) and device parameters (thickness t and channel length l). By tuning the NCG parameters suitably and/or increasing the bias voltage V, an enhancement in the detectivity appears feasible (See **Appendix A7** for derivation of detectivity).

Bibliography

[1] R. P. Feynmann, *Eng. Sci.* **1960**, *25*, 22–36.

[2] S. Yamashita, *APL Photonics* **2019**, *4*, 034301.

[3] S. Yamashita, A. Martinez, B. Xu, in (Eds.: G.S. Subramania, S. Foteinopoulou), **2013**, p. 88080Q.

[4] Y. L. Kim, H. Y. Jung, S. Park, B. Li, F. Liu, J. Hao, Y.-K. Kwon, Y. J. Jung, S. Kar, *Nat. Photonics* **2014**, *8*, 239–243.

[5] K. S. Novoselov, A. K. Geim, S. V. Morozov, D. Jiang, Y. Zhang, S. V. Dubonos, I. V. Grigorieva, A. A. Firsov, *Science (80-.).* **2004**, *306*, 666–669.

[6] H. W. Kroto, J. R. Heath, S. C. O'Brien, R. F. Curl, R. E. Smalley, *Nature* **1985**, *318*, 162–163.

[7] S. Iijima, *Nature* **1991**, *354*, 56–58.

[8] C. Lee, X. Wei, J. W. Kysar, J. Hone, *Science (80-.).* **2008**, *321*, 385–388.

[9] A. A. Balandin, S. Ghosh, W. Bao, I. Calizo, D. Teweldebrhan, F. Miao, C. N. Lau, *Nano Lett.* **2008**, *8*, 902–907.

[10] K. I. Bolotin, K. J. Sikes, Z. Jiang, M. Klima, G. Fudenberg, J. Hone, P. Kim, H. L. Stormer, *Solid State Commun.* **2008**, *146*, 351–355.

[11] P. Avouris, M. Freitag, V. Perebeinos, *Nat. Photonics* **2008**, *2*, 341–350.

[12] J. Kong, A. Javey, Eds. , *Carbon Nanotube Electronics*, Springer US, Boston, MA, **2009**.

[13] M. G. Burdanova, G. M. Katyba, R. Kashtiban, G. A. Komandin, E. Butler-Caddle, M. Staniforth, A. A. Mkrtchyan, D. V. Krasnikov, Y. G. Gladush, J. Sloan, A. G. Nasibulin, J. Lloyd-Hughes, *Carbon N. Y.* **2021**, *173*, 245–252.

[14] M. Liu, X. Yin, E. Ulin-Avila, B. Geng, T. Zentgraf, L. Ju, F. Wang, X. Zhang, *Nature* **2011**, *474*, 64–67.

[15] F. H. L. Koppens, T. Mueller, P. Avouris, A. C. Ferrari, M. S. Vitiello, M. Polini, *Nat. Nanotechnol.* **2014**, *9*, 780–793.

[16] X. He, F. Léonard, J. Kono, *Adv. Opt. Mater.* **2015**, *3*, 989–1011.

[17] Z. Sun, H. Chang, *ACS Nano* **2014**, *8*, 4133–4156.

[18] X. He, H. Htoon, S. K. Doorn, W. H. P. Pernice, F. Pyatkov, R. Krupke, A. Jeantet, Y. Chassagneux, C. Voisin, *Nat. Mater.* **2018**, *17*, 663–670.

[19] R. R. Nair, P. Blake, A. N. Grigorenko, K. S. Novoselov, T. J. Booth, T. Stauber, N. M. R. Peres, A. K. Geim, *Science (80-.).* **2008**, *320*, 1308–1308.

[20] F. Jiang, M. Shi, J. Zhou, Y. Bu, J.-P. Ao, X. S. Chen, *Adv. Photonics Res.* **2021**, *2*, 2000187.

[21] Y. Liu, R. Cheng, L. Liao, H. Zhou, J. Bai, G. Liu, L. Liu, Y. Huang, X. Duan, *Nat. Commun.* **2011**, *2*, 579.

[22] P. Ma, Y. Salamin, B. Baeuerle, A. Josten, W. Heni, A. Emboras, J. Leuthold, *ACS Photonics* **2019**, *6*, 154–161.

[23] S. Reich, C. Thomsen, J. Maultzsch, *Carbon Nanotubes: Basic Concepts and Physical Properties*, Wiley, **2008**.

[24] F. Wang, G. Dukovic, L. E. Brus, T. F. Heinz, *Science (80-.).* **2005**, *308*, 838–841.

[25] Y. Murakami, E. Einarsson, T. Edamura, S. Maruyama, *Phys. Rev. Lett.* **2005**, *94*, 087402.

[26] K. Liu, X. Hong, S. Choi, C. Jin, R. B. Capaz, J. Kim, W. Wang, X. Bai, S. G. Louie, E. Wang, F. Wang, *Proc. Natl. Acad. Sci.* **2014**, *111*, 7564–7569.

[27] F. Bonaccorso, Z. Sun, T. Hasan, A. C. Ferrari, *Nat. Photonics* **2010**, *4*, 611–622.

[28] R. Byron Pipes, S. J. V. Frankland, P. Hubert, E. Saether, *Compos. Sci. Technol.* **2003**, *63*, 1349–1358.

[29] C. Kittel, *Introduction to Solid State Physics*, Wiley, **2004**.

[30] M. Fox, *Optical Properties of Solids*, Oxford University Press, **2010**.

[31] M. Machón, S. Reich, C. Thomsen, D. Sánchez-Portal, P. Ordejón, *Phys. Rev. B* **2002**, *66*, 155410.

[32] K. Sasaki, K. Hitachi, *Commun. Phys.* **2020**, *3*, 90.

[33] A. B. Kuzmenko, E. van Heumen, F. Carbone, D. van der Marel, *Phys. Rev. Lett.* **2008**, *100*, 117401.

[34] X. Li, C. W. Magnuson, A. Venugopal, J. An, J. W. Suk, B. Han, M. Borysiak, W. Cai, A. Velamakanni, Y. Zhu, L. Fu, E. M. Vogel, E. Voelkl, L. Colombo, R. S. Ruoff, *Nano Lett.* **2010**, *10*, 4328–4334.

[35] A. Turchanin, D. Weber, M. Büenfeld, C. Kisielowski, M. V. Fistul, K. B. Efetov, T. Weimann, R. Stosch, J. Mayer, A. Gölzhäuser, *ACS Nano* **2011**, *5*, 3896–3904.

[36] Z. Zhang, Y. Guo, X. Wang, D. Li, F. Wang, S. Xie, *Adv. Funct. Mater.* **2014**, *24*, 835–840.

[37] A. Riaz, F. Pyatkov, A. Alam, S. Dehm, A. Felten, V. S. K. Chakravadhanula, B. S. Flavel, C. Kübel, U. Lemmer, R. Krupke, *Nanotechnology* **2015**, *26*, 325202.

[38] A. Isacsson, A. W. Cummings, L. Colombo, L. Colombo, J. M. Kinaret, S. Roche, *2D Mater.* **2016**, *4*, 012002.

[39] I. Vlassiouk, S. Smirnov, I. Ivanov, P. F. Fulvio, S. Dai, H. Meyer, M. Chi, D. Hensley, P. Datskos, N. V Lavrik, *Nanotechnology* **2011**, *22*, 275716.

[40] A. W. Cummings, D. L. Duong, V. L. Nguyen, D. Van Tuan, J. Kotakoski, J. E. Barrios Vargas, Y. H. Lee, S. Roche, *Adv. Mater.* **2014**, *26*, 5079–5094.

[41] I. S. Beloborodov, A. V. Lopatin, V. M. Vinokur, K. B. Efetov, *Rev. Mod. Phys.* **2007**, *79*, 469–518.

[42] B. I. Shklovskii, A. L. Efros, *Electronic Properties of Doped Semiconductors*, Springer Berlin Heidelberg, Berlin, Heidelberg, **1984**.

[43] R. Saito, G. Dresselhaus, M. S. Dresselhaus, *Phys. Rev. B* **2000**, *61*, 2981–2990.

[44] R. Saito, M. Fujita, G. Dresselhaus, M. S. Dresselhaus, *Phys. Rev. B* **1992**, *46*, 1804–1811.

[45] L. Van Hove, *Phys. Rev.* **1953**, *89*, 1189–1193.

[46] S. Bellucci, P. Onorato, in *Phys. Prop. Ceram. Carbon Nanoscale Struct.*, Springer Berlin Heidelberg, Berlin, Heidelberg, **2011**, pp. 45–109.

[47] S. P. Schießl, X. de Vries, M. Rother, A. Massé, M. Brohmann, P. A. Bobbert, J. Zaumseil, *Phys. Rev. Mater.* **2017**, *1*, 046003.

[48] M. Rother, S. P. Schießl, Y. Zakharko, F. Gannott, J. Zaumseil, *ACS Appl. Mater. Interfaces* **2016**, *8*, 5571–5579.

[49] N. F. Zorn, J. Zaumseil, *Appl. Phys. Rev.* **2021**, *8*, 041318.

[50] F. Tuinstra, J. L. Koenig, *J. Chem. Phys.* **1970**, *53*, 1126–1130.

[51] A. C. Ferrari, J. C. Meyer, V. Scardaci, C. Casiraghi, M. Lazzeri, F. Mauri, S. Piscanec, D. Jiang, K. S. Novoselov, S. Roth, A. K. Geim, *Phys. Rev. Lett.* **2006**, *97*, 187401.

[52] A. C. Ferrari, D. M. Basko, *Nat. Nanotechnol.* **2013**, *8*, 235–246.

[53] A. C. Ferrari, J. Robertson, *Phys. Rev. B* **2001**, *64*, 075414.

[54] A. C. Ferrari, J. Robertson, *Philos. Trans. R. Soc. London. Ser. A Math. Phys. Eng. Sci.* **2004**, *362*, 2477–2512.

[55] A. C. Ferrari, J. Robertson, *Phys. Rev. B* **2000**, *61*, 14095–14107.

[56] L. G. Cançado, A. Jorio, M. A. Pimenta, *Phys. Rev. B* **2007**, *76*, 064304.

[57] L. G. Cançado, K. Takai, T. Enoki, M. Endo, Y. A. Kim, H. Mizusaki, A. Jorio, L. N. Coelho, R. Magalhães-Paniago, M. A. Pimenta, *Appl. Phys. Lett.* **2006**, *88*, 163106.

[58] J. E. Proctor, D. Melendrez Armada, A. Vijayaraghavan, *An Introduction to Graphene and Carbon Nanotubes*, CRC Press, **2017**.

[59] P. T. Araujo, P. B. C. Pesce, M. S. Dresselhaus, K. Sato, R. Saito, A. Jorio, *Phys. E Low-dimensional Syst. Nanostructures* **2010**, *42*, 1251–1261.

[60] P. T. Araujo, I. O. Maciel, P. B. C. Pesce, M. A. Pimenta, S. K. Doorn, H. Qian, A. Hartschuh, M. Steiner, L. Grigorian, K. Hata, A. Jorio, *Phys. Rev. B* **2008**, *77*, 241403.

[61] Z. Zhang, B. Ge, Y. Guo, D. Tang, X. Wang, F. Wang, *Chem. Commun.* **2013**, *49*, 2789.

[62] R. Yekani, E. Rusak, A. Riaz, A. Felten, B. Breitung, S. Dehm, D. Perera, J. Rohrer, C. Rockstuhl, R. Krupke, *Nanoscale* **2018**, *10*, 12156–12162.

[63] S. K. Jerng, J. H. Lee, D. S. Yu, Y. S. Kim, J. Ryou, S. Hong, C. Kim, S. Yoon, S. H. Chun, *J. Phys. Chem. C* **2012**, *116*, 7380–7385.

[64] N. Lindvall, M. T. Cole, T. J. Booth, P. Bøggild, J. Liu, A. Yurgens, *J. Appl. Phys.* **2012**, *111*, 044103.

[65] A. Guerra, A. Achour, S. Vizireanu, G. Dinescu, S. Messaci, T. Hadjersi, R. Boukherroub, Y. Coffinier, J.-J. Pireaux, *Appl. Surf. Sci.* **2019**, *481*, 926–932.

[66] T. Zhao, C. Xu, W. Ma, Z. Liu, T. Zhou, Z. Liu, S. Feng, M. Zhu, N. Kang, D.-M. Sun, H.-M. Cheng, W. Ren, *Nat. Commun.* **2019**, *10*, 4854.

[67] O. Simionescu, R. C. Popa, A. Avram, G. Dinescu, *Plasma Process. Polym.* **2020**, *17*, 1900246.

[68] S. Datta, *Lessons from Nanoelectronics*, World Scientific, **2018**.

[69] M. Buscema, M. Barkelid, V. Zwiller, H. S. J. van der Zant, G. A. Steele, A. Castellanos-Gomez, *Nano Lett.* **2013**, *13*, 358–363.

[70] X. Xu, N. M. Gabor, J. S. Alden, A. M. van der Zande, P. L. McEuen, *Nano Lett.* **2010**, *10*, 562–566.

[71] T. J. Echtermeyer, P. S. Nene, M. Trushin, R. V. Gorbachev, A. L. Eiden, S. Milana, Z. Sun, J. Schliemann, E. Lidorikis, K. S. Novoselov, A. C. Ferrari, *Nano Lett.* **2014**, *14*, 3733–3742.

[72] M. Freitag, T. Low, P. Avouris, *Nano Lett.* **2013**, *13*, 1644–1648.

[73] B. C. St-Antoine, D. Ménard, R. Martel, *Nano Lett.* **2011**, *11*, 609–613.

[74] M. Barkelid, V. Zwiller, *Nat. Photonics* **2014**, *8*, 47–51.

[75] F. Niklaus, C. Vieider, H. Jakobsen, in (Eds.: J.-C. Chiao, X. Chen, Z. Zhou, X. Li), **2007**, p. 68360D.

[76] M. E. Itkis, F. Borondics, A. Yu, R. C. Haddon, *Science (80-.).* **2006**, *312*, 413–416.

[77] E. C. Peters, E. J. H. Lee, M. Burghard, K. Kern, *Appl. Phys. Lett.* **2010**, *97*, 193102.

[78] T. Mueller, F. Xia, M. Freitag, J. Tsang, P. Avouris, *Phys. Rev. B* **2009**, *79*, 245430.

[79] G. Rao, M. Freitag, H.-Y. Chiu, R. S. Sundaram, P. Avouris, *ACS Nano* **2011**, *5*, 5848–5854.

[80] J.-M. Liu, I.-T. Lin, *Graphene Photonics*, Cambridge University Press, **2018**.

[81] N. M. Gabor, J. C. W. Song, Q. Ma, N. L. Nair, T. Taychatanapat, K. Watanabe, T. Taniguchi, L. S. Levitov, P. Jarillo-Herrero, *Science (80-.).* **2011**, *334*, 648–652.

[82] K. J. Tielrooij, J. C. W. Song, S. A. Jensen, A. Centeno, A. Pesquera, A. Zurutuza Elorza, M.

Bonn, L. S. Levitov, F. H. L. Koppens, *Nat. Phys.* **2013**, *9*, 248–252.

[83] J. C. W. Song, K. J. Tielrooij, F. H. L. Koppens, L. S. Levitov, *Phys. Rev. B* **2013**, *87*, 155429.

[84] S. Piscanec, M. Lazzeri, F. Mauri, A. C. Ferrari, J. Robertson, *Phys. Rev. Lett.* **2004**, *93*, 185503.

[85] M. Lazzeri, S. Piscanec, F. Mauri, A. C. Ferrari, J. Robertson, *Phys. Rev. Lett.* **2005**, *95*, 236802.

[86] R. Bistritzer, A. H. MacDonald, *Phys. Rev. Lett.* **2009**, *102*, 206410.

[87] M. Freitag, T. Low, F. Xia, P. Avouris, *Nat. Photonics* **2013**, *7*, 53–59.

[88] T. DeBorde, L. Aspitarte, T. Sharf, J. W. Kevek, E. D. Minot, *ACS Nano* **2014**, *8*, 216–221.

[89] J. P. Small, K. M. Perez, P. Kim, *Phys. Rev. Lett.* **2003**, *91*, 256801.

[90] Q. Zeng, S. Wang, L. Yang, Z. Wang, Z. Zhang, L. Peng, W. Zhou, S. Xie, *Nano Res.* **2012**, *5*, 33–42.

[91] B. C. St-Antoine, D. Ménard, R. Martel, *Nano Res.* **2012**, *5*, 73–81.

[92] S. Nanot, A. W. Cummings, C. L. Pint, A. Ikeuchi, T. Akiho, K. Sueoka, R. H. Hauge, F. Léonard, J. Kono, *Sci. Rep.* **2013**, *3*, 1335.

[93] S. A. Maier, *Plasmonics: Fundamentals and Applications*, Springer US, New York, NY, **2007**.

[94] J. Aaron, E. de la Rosa, K. Travis, N. Harrison, J. Burt, M. José-Yacamán, K. Sokolov, *Opt. Express* **2008**, *16*, 2153.

[95] Y. Ding, Z. Cheng, X. Zhu, K. Yvind, J. Dong, M. Galili, H. Hu, N. A. Mortensen, S. Xiao, L. K. Oxenløwe, *Nanophotonics* **2020**, *9*, 317–325.

[96] K. Okamoto, I. Niki, A. Shvartser, Y. Narukawa, T. Mukai, A. Scherer, *Nat. Mater.* **2004**, *3*, 601–605.

[97] A. Alù, N. Engheta, *Phys. Rev. E* **2005**, *72*, 016623.

[98] M. Bauch, K. Toma, M. Toma, Q. Zhang, J. Dostalek, *Plasmonics* **2014**, *9*, 781–799.

[99] J. Dostálek, W. Knoll, *Biointerphases* **2008**, *3*, FD12–FD22.

[100] E. Prodan, C. Radloff, N. J. Halas, P. Nordlander, *Science (80-.).* **2003**, *302*, 419–422.

[101] J. A. Fan, C. Wu, K. Bao, J. Bao, R. Bardhan, N. J. Halas, V. N. Manoharan, P. Nordlander, G. Shvets, F. Capasso, *Science (80-.).* **2010**, *328*, 1135–1138.

[102] S.-C. Yang, H. Kobori, C.-L. He, M.-H. Lin, H.-Y. Chen, C. Li, M. Kanehara, T. Teranishi, S. Gwo, *Nano Lett.* **2010**, *10*, 632–637.

[103] M. Iwanaga, B. Choi, *Nano Lett.* **2015**, *15*, 1904–1910.

[104] M. Iwanaga, B. Choi, H. T. Miyazaki, Y. Sugimoto, *Nanoscale* **2016**, *8*, 11099–11107.

[105] B. Choi, M. Iwanaga, H. T. Miyazaki, Y. Sugimoto, A. Ohtake, K. Sakoda, *Chem. Commun.* **2015**, *51*, 11470–11473.

[106] P. B. Selvasundaram, Near Infrared Photocurrent Spectroscopy on Carbon Nanotube Devices, TU Darmstadt, **2020**.

[107] C. Downs, T. Vandervelde, *Sensors* **2013**, *13*, 5054–5098.

[108] H. Chen, H. Liu, Z. Zhang, K. Hu, X. Fang, *Adv. Mater.* **2016**, *28*, 403–433.

[109] Q. Liang, Q. Wang, Q. Zhang, J. Wei, S. X. Lim, R. Zhu, J. Hu, W. Wei, C. Lee, C. Sow, W. Zhang, A. T. S. Wee, *Adv. Mater.* **2019**, *31*, 1807609.

[110] C. Yim, N. McEvoy, S. Riazimehr, D. S. Schneider, F. Gity, S. Monaghan, P. K. Hurley, M. C. Lemme, G. S. Duesberg, *Nano Lett.* **2018**, *18*, 1794–1800.

[111] Q. Wang, J. Lai, D. Sun, *Opt. Mater. Express* **2016**, *6*, 2313.

[112] Y. Xie, B. Zhang, S. Wang, D. Wang, A. Wang, Z. Wang, H. Yu, H. Zhang, Y. Chen, M. Zhao, B. Huang, L. Mei, J. Wang, *Adv. Mater.* **2017**, *29*, 1605972.

[113] T. Yan, S. Cai, Z. Hu, Z. Li, X. Fang, *J. Phys. Chem. Lett.* **2021**, *12*, 9912–9918.

[114] N. Youngblood, C. Chen, S. J. Koester, M. Li, *Nat. Photonics* **2015**, *9*, 247–252.

[115] C. Li, H. Wang, F. Wang, T. Li, M. Xu, H. Wang, Z. Wang, X. Zhan, W. Hu, L. Shen, *Light Sci. Appl.* **2020**, *9*, 31.

[116] Z. Li, X. Liu, C. Zuo, W. Yang, X. Fang, *Adv. Mater.* **2021**, *33*, 2103010.

[117] F. Xia, T. Mueller, R. Golizadeh-Mojarad, M. Freitag, Y. Lin, J. Tsang, V. Perebeinos, P. Avouris, *Nano Lett.* **2009**, *9*, 1039–1044.

[118] J. C. W. Song, M. S. Rudner, C. M. Marcus, L. S. Levitov, *Nano Lett.* **2011**, *11*, 4688–4692.

[119] M. Freitag, T. Low, F. Xia, P. Avouris, *Nat. Photonics* **2013**, *7*, 53–59.

[120] T. J. Echtermeyer, L. Britnell, P. K. Jasnos, A. Lombardo, R. V. Gorbachev, A. N. Grigorenko, A. K. Geim, A. C. Ferrari, K. S. Novoselov, *Nat. Commun.* **2011**, *2*, 458.

[121] X. Gan, R.-J. Shiue, Y. Gao, I. Meric, T. F. Heinz, K. Shepard, J. Hone, S. Assefa, D. Englund, *Nat. Photonics* **2013**, *7*, 883–887.

[122] M. Engel, M. Steiner, A. Lombardo, A. C. Ferrari, H. v. Löhneysen, P. Avouris, R. Krupke, *Nat. Commun.* **2012**, *3*, 906.

[123] S. Schuler, D. Schall, D. Neumaier, B. Schwarz, K. Watanabe, T. Taniguchi, T. Mueller, *ACS Photonics* **2018**, *5*, 4758–4763.

[124] G. Konstantatos, M. Badioli, L. Gaudreau, J. Osmond, M. Bernechea, F. P. G. de Arquer, F. Gatti, F. H. L. Koppens, *Nat. Nanotechnol.* **2012**, *7*, 363–368.

[125] I. Nikitskiy, S. Goossens, D. Kufer, T. Lasanta, G. Navickaite, F. H. L. Koppens, G. Konstantatos, *Nat. Commun.* **2016**, *7*, 11954.

[126] Z. Ni, L. Ma, S. Du, Y. Xu, M. Yuan, H. Fang, Z. Wang, M. Xu, D. Li, J. Yang, W. Hu, X. Pi, D. Yang, *ACS Nano* **2017**, *11*, 9854–9862.

[127] S. Ahn, H. Chung, W. Chen, M. A. Moreno-Gonzalez, O. Vazquez-Mena, *J. Chem. Phys.* **2019**, *151*, 234705.

[128] C.-W. Chiang, G. Haider, W.-C. Tan, Y.-R. Liou, Y.-C. Lai, R. Ravindranath, H.-T. Chang, Y.-F. Chen, *ACS Appl. Mater. Interfaces* **2016**, *8*, 466–471.

[129] K. Roy, M. Padmanabhan, S. Goswami, T. P. Sai, G. Ramalingam, S. Raghavan, A. Ghosh, *Nat. Nanotechnol.* **2013**, *8*, 826–830.

[130] M. Furchi, A. Urich, A. Pospischil, G. Lilley, K. Unterrainer, H. Detz, P. Klang, A. M. Andrews, W. Schrenk, G. Strasser, T. Mueller, *Nano Lett.* **2012**, *12*, 2773–2777.

[131] K. Zhou, Q. Cheng, J. Song, L. Lu, Z. Luo, *Opt. Lett.* **2019**, *44*, 3430.

[132] S.-Y. Son, Y.-J. Noh, C. Bok, S. Lee, B. G. Kim, S.-I. Na, H.-I. Joh, *Nanoscale* **2014**, *6*, 678–682.

[133] Q. Zhang, L. Tang, J. Luo, J. Zhang, X. Wang, D. Li, Y. Yao, Z. Zhang, *Carbon N. Y.* **2017**, *111*, 1–7.

[134] C. N. Shyam Kumar, V. S. K. Chakravadhanula, A. Riaz, S. Dehm, D. Wang, X. Mu, B. Flavel, R. Krupke, C. Kübel, *Nanoscale* **2017**, *9*, 12835–12842.

[135] C. N. Shyam Kumar, M. Konrad, V. S. K. Chakravadhanula, S. Dehm, D. Wang, W. Wenzel, R. Krupke, C. Kübel, *Nanoscale Adv.* **2019**, *1*, DOI 10.1039/c9na00055k.

[136] X.-L. Li, X.-F. Qiao, W.-P. Han, Y. Lu, Q.-H. Tan, X.-L. Liu, P.-H. Tan, *Nanoscale* **2015**, *7*, 8135–8141.

[137] S. Nakamura, D. Miyafuji, T. Fujii, T. Matsui, H. Fukuyama, *Cryogenics (Guildf).* **2017**, *86*, 118–122.

[138] S. Kumar, Nanocarbon Devices and Sensors, TU Darmstadt, **2021**.

[139] A. Riaz, A. Alam, P. B. Selvasundaram, S. Dehm, F. Hennrich, M. M. Kappes, R. Krupke, *Adv. Electron. Mater.* **2019**, *5*, DOI 10.1002/aelm.201800265.

[140] W. Primak, L. H. Fuchs, *Phys. Rev.* **1954**, *95*, 22–30.

[141] K. J. Tielrooij, M. Massicotte, L. Piatkowski, A. Woessner, Q. Ma, P. Jarillo-Herrero, N. F. van Hulst, F. H. L. Koppens, *J. Phys. Condens. Matter* **2015**, *27*, 164207.

[142] P. H. D. A. A. R. U. L. C. F. Blackman, *Proc. R. Soc. London. Ser. A. Math. Phys. Sci.* **1960**, *255*, 293–306.

[143] D. M. Rowe, Ed. , *CRC Handbook of Thermoelectrics*, CRC Press, **2018**.

[144] K. J. Tielrooij, M. Massicotte, L. Piatkowski, A. Woessner, Q. Ma, P. Jarillo-Herrero, N. F. V.

Hulst, F. H. L. Koppens, *J. Phys. Condens. Matter* **2015**, *27*, DOI 10.1088/0953-8984/27/16/164207.

[145] X. Gong, M. Tong, Y. Xia, W. Cai, J. S. Moon, Y. Cao, G. Yu, C.-L. Shieh, B. Nilsson, A. J. Heeger, *Science (80-.).* **2009**, *325*, 1665–1667.

[146] M. Darwish, H. Boysan, C. Liewald, B. Nickel, A. Gagliardi, *Org. Electron.* **2018**, *62*, 474–480.

[147] T. Ma, Z. Liu, J. Wen, Y. Gao, X. Ren, H. Chen, C. Jin, X.-L. Ma, N. Xu, H.-M. Cheng, W. Ren, *Nat. Commun.* **2017**, *8*, 14486.

[148] F. Zhang, P.-X. Hou, C. Liu, B.-W. Wang, H. Jiang, M.-L. Chen, D.-M. Sun, J.-C. Li, H.-T. Cong, E. I. Kauppinen, H.-M. Cheng, *Nat. Commun.* **2016**, *7*, 11160.

[149] H. Kataura, Y. Kumazawa, Y. Maniwa, I. Umezu, S. Suzuki, Y. Ohtsuka, Y. Achiba, *Synth. Met.* **1999**, *103*, 2555–2558.

[150] A. Jorio, A. G. Souza Filho, G. Dresselhaus, M. S. Dresselhaus, A. K. Swan, M. S. Ünlü, B. B. Goldberg, M. A. Pimenta, J. H. Hafner, C. M. Lieber, R. Saito, *Phys. Rev. B* **2002**, *65*, 155412.

[151] P. T. Araujo, S. K. Doorn, S. Kilina, S. Tretiak, E. Einarsson, S. Maruyama, H. Chacham, M. A. Pimenta, A. Jorio, *Phys. Rev. Lett.* **2007**, *98*, 067401.

[152] J. S. Soares, L. G. Cançado, E. B. Barros, A. Jorio, *Phys. status solidi* **2010**, *247*, 2835–2837.

[153] M. Steiner, M. Freitag, J. C. Tsang, V. Perebeinos, A. A. Bol, A. V. Failla, P. Avouris, *Appl. Phys. A* **2009**, *96*, 271–282.

[154] P. T. Araujo, I. O. Maciel, P. B. C. Pesce, M. A. Pimenta, S. K. Doorn, H. Qian, A. Hartschuh, M. Steiner, L. Grigorian, K. Hata, A. Jorio, *Phys. Rev. B* **2008**, *77*, 241403.

[155] R. Saito, G. Dresselhaus, M. S. Dresselhaus, *Phys. Rev. B* **2000**, *61*, 2981–2990.

[156] J. Lefebvre, J. Ding, Z. Li, F. Cheng, N. Du, P. R. L. Malenfant, *Appl. Phys. Lett.* **2015**, *107*, 243301.

[157] S. Kumar, D. Dagli, S. Dehm, C. Das, L. Wei, Y. Chen, F. Hennrich, R. Krupke, *Phys. status solidi – Rapid Res. Lett.* **2020**, *14*, 2000193.

[158] N. T. Hung, A. R. T. Nugraha, E. H. Hasdeo, M. S. Dresselhaus, R. Saito, *Phys. Rev. B* **2015**, *92*, 165426.

[159] C. Hu, C. Liu, L. Chen, C. Meng, S. Fan, *ACS Nano* **2010**, *4*, 4701–4706.

[160] J. L. Blackburn, A. J. Ferguson, C. Cho, J. C. Grunlan, *Adv. Mater.* **2018**, *30*, 1704386.

[161] K. Balasubramanian, M. Burghard, K. Kern, M. Scolari, A. Mews, *Nano Lett.* **2005**, *5*, 507–510.

[162] P. Avouris, M. Freitag, V. Perebeinos, *Nat. Photonics* **2008**, *2*, 341–350.

[163] A. W. Tsen, L. A. K. Donev, H. Kurt, L. H. Herman, J. Park, *Nat. Nanotechnol.* **2009**, *4*, 108–113.

[164] E. Sczygelski, V. K. Sangwan, C.-C. Wu, H. N. Arnold, K. Everaerts, T. J. Marks, M. C. Hersam, L. J. Lauhon, *Appl. Phys. Lett.* **2013**, *102*, 083104.

[165] S. Ilani, L. A. K. Donev, M. Kindermann, P. L. McEuen, *Nat. Phys.* **2006**, *2*, 687–691.

[166] D. K. Schroder, R. N. Thomas, J. C. Swartz, *IEEE Trans. Electron Devices* **1978**, *25*, 254–261.

[167] M. Çopuroğlu, H. Sezen, R. L. Opila, S. Suzer, *ACS Appl. Mater. Interfaces* **2013**, *5*, 5875–5881.

[168] M. S. Marcus, J. M. Simmons, O. M. Castellini, R. J. Hamers, M. A. Eriksson, *J. Appl. Phys.* **2006**, *100*, DOI 10.1063/1.2357413.

[169] S. C. Baker-Finch, K. R. McIntosh, D. Yan, K. C. Fong, T. C. Kho, *J. Appl. Phys.* **2014**, *116*, 063106.

[170] M. Gaulke, A. Janissek, N. A. Peyyety, I. Alamgir, A. Riaz, S. Dehm, H. Li, U. Lemmer, B. S. Flavel, M. M. Kappes, F. Hennrich, L. Wei, Y. Chen, F. Pyatkov, R. Krupke, *ACS Nano* **2020**, *14*, 2709–2717.

[171] Y. D. Kim, H. Kim, Y. Cho, J. H. Ryoo, C.-H. Park, P. Kim, Y. S. Kim, S. Lee, Y. Li, S.-N. Park, Y. Shim Yoo, D. Yoon, V. E. Dorgan, E. Pop, T. F. Heinz, J. Hone, S.-H. Chun, H. Cheong, S. W. Lee, M.-H. Bae, Y. D. Park, *Nat. Nanotechnol.* **2015**, *10*, 676–681.

[172] M. Engel, M. Steiner, A. Lombardo, A. C. Ferrari, H. v. Löhneysen, P. Avouris, R. Krupke, *Nat. Commun.* **2012**, *3*, 906.

[173] M. Furchi, A. Urich, A. Pospischil, G. Lilley, K. Unterrainer, H. Detz, P. Klang, A. M. Andrews, W. Schrenk, G. Strasser, T. Mueller, *Nano Lett.* **2012**, *12*, 2773–2777.

[174] B. Choi, M. Iwanaga, H. T. Miyazaki, K. Sakoda, Y. Sugimoto, *J. Micro/Nanolithography, MEMS, MOEMS* **2014**, *13*, 023007.

[175] M. Kanidi, A. Dagkli, N. Kelaidis, D. Palles, S. Aminalragia-Giamini, J. Marquez-Velasco, A. Colli, A. Dimoulas, E. Lidorikis, M. Kandyla, E. I. Kamitsos, *J. Phys. Chem. C* **2019**, *123*, 3076–3087.

[176] N. Saigal, A. Mukherjee, V. Sugunakar, S. Ghosh, *Rev. Sci. Instrum.* **2014**, *85*, 073105.

[177] B. Choi, M. Iwanaga, T. Ochiai, H. T. Miyazaki, Y. Sugimoto, K. Sakoda, *Appl. Phys. Lett.* **2014**, *105*, 201106.

[178] L. A. Coldren, S. W. Corzine, M. L. Mašanović, in *Diode Lasers Photonic Integr. Circuits*, John Wiley & Sons, Inc., Hoboken, NJ, USA, **2012**, pp. 395–450.

[179] P. Yeh, *Optical Waves in Layered Media*, John Wiley & Sons, Inc., New York, **2005**.

[180] M. Born, E. Wolf, A. B. Bhatia, P. C. Clemmow, D. Gabor, A. R. Stokes, A. M. Taylor, P. A. Wayman, W. L. Wilcock, *Principles of Optics*, Cambridge University Press, **1999**.

[181] S. J. Byrnes, **2016**.

Appendix

A1 Transfer Matrix Methods

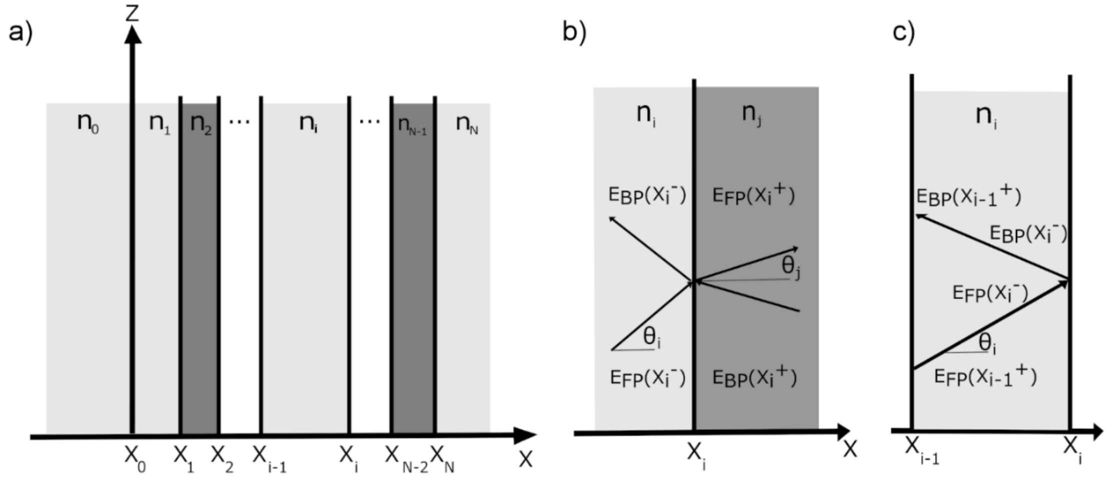

Figure A1: (a) Multilayer dielectric stack system with the light propagation in X-Z plane and the corresponding refractive indices of each layer are indicated. (b) Reflection and transmission at the interface X_i. (c) light propagation within a layer of a certain thickness and refractive index. Adapted from [[178]].

Transfer Matric Method (TMM) is an indispensable tool to calculate the light propagation in a stratified medium. The total reflectance and transmittance in the multilayer stack system can be estimated from the layer thicknesses in the stack and the wavelength-dependent complex refractive index of each layer. In TMM, the stratified medium is treated as an optical system where the electric and magnetic field components at the incident layer are related to the field components at the final layer through a cascade of matrices that contain information about the light propagation in the individual layers and at the layer interfaces.[178],[179] **Figure A1** shows the x-z view of the multilayer structure, where the x-axis is the normal to the interfaces between the layers that are in turn parallel to the y-z plane. The multilayer structure consists of individual layers with thickness d and complex refractive index denoted by n, where d_i and n_i denote the thickness and refractive index of the layer i, and the position of the interface between the layers i and i+1 is denoted by X_i. The $X_{i+1} - X_i$ gives the layer thickness d_i. In the **Figure A1**, the wavevector of the incident light lies only in the x-z plane with the y-component (k_y) being zero. Since the incident wave can be defined with two orthogonal polarizations TE (s-wave) or TM (p-wave), in the following section, the discussion here is restricted to the TE case, that is when the electric field is parallel to the layer interface. The electric field in each layer can be expressed in terms of its amplitude (Eq. A1.1) and all the forward propagating waves in the positive x-direction have the same sign and form a plane wave. The same holds for the backward propagating waves in the negative x-direction. The total electric field in a layer can thus be expressed as a summation of amplitudes/complex amplitude of forward (FP) and backward (BP) propagating waves.

$$E(x,y,z) = A_{FP}e^{-j(k_{x,i}x+k_zz)} + A_{BP}e^{-j(-k_{x,i}x+k_zz)} \qquad \text{(A1.1)}$$

$$= E_{FP}(x)e^{-j(k_zz)} + E_{BP}(x)e^{-j(k_zz)} \qquad \text{(A1.2)}$$

In the relation A1.1, the x-component of the wavevector k_i in the layer i is denoted by $k_{x,i}$ and is given by,

$$k_{x,i} = \sqrt{[(n_ik_0)^2 - k_z^2]} \qquad \text{(A1.3)}$$

In equation (A1.2), i = 0,1,2..N and $k_0 = (\frac{\omega}{c_0})$, where ω is the frequency, and c_0 being the speed of light in vacuum. Due to the boundary conditions (phase is continuous at the boundary x = 0) and the resulting relationship between the field amplitudes of incident, reflected and transmitted waves at the interfaces, k_z thus remains constant. At a given z, the complex electric fields before the first interface (X_0) and behind the last interface (X_{N-1}) in the multilayer stack are related via. the full transfer matrix in the following way.

$$\begin{bmatrix} E_{FP}(x_0^-) \\ E_{BP}(x_0^-) \end{bmatrix} = T_{0N} \begin{bmatrix} E_{FP}(x_{N-1}^+) \\ E_{BP}(x_{N-1}^+) \end{bmatrix} = \begin{bmatrix} T_{11}^{0N} & T_{12}^{0N} \\ T_{21}^{0N} & T_{22}^{0N} \end{bmatrix} \begin{bmatrix} E_{FP}(x_{N-1}^+) \\ E_{BP}(x_{N-1}^+) \end{bmatrix} \qquad \text{(A1.4)}$$

The transfer matrix for the complete multilayer stack can be decomposed into the following two building blocks (i) transfer matrix at an interface and (ii) transfer matrix for the wave propagation within the layer. Transfer matrices are thus calculated for every layer and every interface and their product is the resultant full matrix of the multilayer stack. **Figure A1-b** shows the wave propagation through an interface between layer i and layer j, and the complex electric fields amplitudes of the waves propagating in the forward and backward direction on the either side of the interface (X_i) can be understood by the following relation.

$$\begin{bmatrix} E_{FP}(x_i^+) \\ E_{BP}(x_i^-) \end{bmatrix} = \begin{bmatrix} t_{ij} & r_{ij} \\ r_{ij} & t_{ji} \end{bmatrix} \begin{bmatrix} E_{FP}(x_i^-) \\ E_{BP}(x_i^+) \end{bmatrix} \qquad \text{(A1.5)}$$

In the relation, t and r are the complex transmission and reflection coefficients (from the Fresnel equations[180]), and for the case of TE polarization they are described as

$$r_{ij} = \frac{E_{BP}(x_i^-)}{E_{FP}(x_i^-)} = \frac{k_x^i - k_x^j}{k_x^i + k_x^j} \qquad \text{(A1.6)}$$

$$t_{ij} = \frac{E_{FP}(x_i^+)}{E_{FP}(x_i^-)} = 1 + r_{ij} = \frac{2k_x^i}{k_x^i + k_x^j} \tag{A1.7}$$

The Fresnel equations in terms of the refractive indices and angle of incidence are given by,

$$r_{ij} = \frac{E_{BP}(x_i^-)}{E_{FP}(x_i^-)} = \frac{n_i \cos\theta_i - n_j \cos\theta_j}{n_i \cos\theta_i + n_j \cos\theta_j} \tag{A1.8}$$

$$t_{ij} = \frac{E_{FP}(x_i^+)}{E_{FP}(x_i^-)} = 1 + r_{ij} = \frac{2n_i \cos\theta_i}{n_i \cos\theta_i + n_j \cos\theta_j} \tag{A1.9}$$

Using the Fresnel equations (eq. A1.8 & eq. A1.9) and rewriting the eq. A1.6 results in the following relation for backward and forward propagating waves.

$$\begin{bmatrix} E_{FP}(x_i^-) \\ E_{BP}(x_i^-) \end{bmatrix} = \begin{bmatrix} \frac{1}{t_{ji}} & -\frac{r_{ij}}{t_{ij}} \\ \frac{r_{ij}}{t_{ij}} & t_{ji} - \frac{r_{ij}}{t_{ij}} r_{ji} \end{bmatrix} \begin{bmatrix} E_{FP}(x_i^+) \\ E_{BP}(x_i^+) \end{bmatrix} \tag{A1.10}$$

From the symmetry relations (eq. A1.11 and eq. A1.12) of the Fresnel equations, the eq. A1.10 can be simplified and is expressed in eq. A1.13

$$r_{ij} = -r_{ji} \tag{A1.11}$$

$$t_{ij} t_{ji} - r_{ij} r_{ji} = 1 \tag{A1.12}$$

$$\begin{bmatrix} E_{FP}(x_i^-) \\ E_{BP}(x_i^-) \end{bmatrix} = \frac{1}{t_{ji}} \begin{bmatrix} 1 & r_{ij} \\ r_{ij} & 1 \end{bmatrix} \begin{bmatrix} E_{FP}(x_i^+) \\ E_{BP}(x_i^+) \end{bmatrix} \tag{A1.13}$$

The transfer matrix through the interface can be thus described by eq. A1.14

$$T_{ij} = \frac{1}{t_{ji}} \begin{bmatrix} 1 & r_{ij} \\ r_{ij} & 1 \end{bmatrix} \tag{A1.14}$$

Having described the transfer matrix for the interface, the next step involves the construction of the matrix for the wave propagation inside a layer. In **Figure A1-c**, at a given z, the amplitudes for the forward and backward traveling waves in the layer i at positions X_{i-1} and X_i are related through the following relations.

$$E_{FP}(x_i^-) = E_{FP}(x_{i-1}^+)e^{-jk_{x,i}d_i} \tag{A1.15}$$

$$E_{BP}(x_{i-1}^+) = E_{BP}(x_i^-)e^{-jk_{x,i}d_i} \tag{A1.16}$$

The corresponding transfer matrix for the wave propagation through the layer can be obtained using the relation A1.17.

$$T_i = \begin{bmatrix} e^{j\phi_i} & 0 \\ 0 & e^{-j\phi_i} \end{bmatrix} \tag{A1.17}$$

Where, $\phi = k_{x,i}d_i$ is a complex quantity and can be expressed as,

$$\phi_i = k_{x,i}d_i = \frac{2\pi}{\lambda_0} n_i d_i \cos\theta_i \tag{A1.18}$$

The complete transfer matrix for the layers in the multilayer structure in **Figure A1-a** can now be described using the equation A1.19.

$$\begin{bmatrix} E_{FP}(x_0^-) \\ E_{BP}(x_0^-) \end{bmatrix} = T_{0N} \begin{bmatrix} E_{FP}(x_{N-1}^+) \\ E_{BP}(x_{N-1}^+) \end{bmatrix} = \begin{bmatrix} T_{11}^{0N} & T_{12}^{0N} \\ T_{21}^{0N} & T_{22}^{0N} \end{bmatrix} \begin{bmatrix} E_{FP}(x_{N-1}^+) \\ E_{BP}(x_{N-1}^+) \end{bmatrix} \tag{A1.19}$$

With T_{0N} expressed as,

$$T_{0N} = T_{01}T_1T_{12}T_2 \ldots . T_{N-1}T_{(N-1)N} \tag{A1.20}$$

Equation A1.20 represents the matrix formalism for the wave propagation in a multilayer system. Since the incident wave is only in one direction (positive x) and there is incoming light from the right side of the stack, that is $E_{BP}(x_{N-1}^+) = 0$. Hence the equation A1.19 reduces to the following.

$$\begin{bmatrix} E_{FP}(x_0^-) \\ E_{BP}(x_0^-) \end{bmatrix} = T_{0N} \begin{bmatrix} E_{FP}(x_{N-1}^+) \\ 0 \end{bmatrix} = \begin{bmatrix} T_{11}^{0N} & T_{12}^{0N} \\ T_{21}^{0N} & T_{22}^{0N} \end{bmatrix} \begin{bmatrix} E_{FP}(x_{N-1}^+) \\ 0 \end{bmatrix} \tag{A1.21}$$

The matrix formalism in eq. A1.21 results in two equations with two unknowns ($E_{FP}(x_{N-1}^+)$ and $E_{BP}(x_0^-)$). And for an arbitrary stack of multi-layers the amplitude reflection and transmission coefficients can be calculated using the relations described in equations A1.8 and A1.9.

$$r = \frac{E_{BP}(x_0^-)}{E_{FP}(x_0^-)} = \frac{T_{21}^{0N}}{T_{11}^{0N}} \tag{A1.22}$$

$$t = \frac{E_{FP}(x_{N-1}^+)}{E_{FP}(x_0^-)} = \frac{1}{T_{11}^{0N}} \tag{A1.23}$$

From the above reflection and transmission coefficients, the reflected and transmitted (R and T) power coefficients can be calculated from the Poynting vector. The Poynting vector (**S**) is defined as the net energy in a given volume that propagates through a given area at a certain time and has the units Watts/m^2. The real part of the Poynting vector gives the power density of the forward or backward propagating plane wave in a given layer and is given by eqns. A1.24 and A1.25.

$$\boldsymbol{S} = \boldsymbol{E} \times \boldsymbol{H} = \boldsymbol{E} \times \frac{\boldsymbol{B}}{\mu_0} \tag{A1.24}$$

$$\langle P(x) \rangle = Re\big(S(x)\big) \tag{A1.25}$$

From $E = cB$, where $c = \frac{c_0}{n}$, and $c_0 = \frac{1}{\sqrt{\mu_0 \epsilon_0}}$ and the free-space impedence $Z_0 = \sqrt{\frac{\mu_0}{\varepsilon_0}}$, the time averaged power density can be expressed as[181]

$$\langle P(x) \rangle = Re(n) \frac{|E(x_i)|^2}{2Z_0} \tag{A1.26}$$

The power density parallel to the layers is given by,

$$\langle P(x)_{\parallel} \rangle = Re(n) \cos\theta_i \frac{|E(x_i)|^2}{2Z_0} \tag{A1.27}$$

Next, the local absorption in given layer at a given depth can be calculated in terms of the energy density (power per volume), which can also be expressed in the multiples of incoming power density (power per area), this ratio would then result in absorptance or the absorbed energy density in units of 1/length:[181]

$$\alpha(x) = \frac{|E(x_i)|^2 Im(n \cos\theta_i) k_{x,i}}{Re(n_0 \cos\theta_0)} \tag{A1.28}$$

A2.1 Photoresponse of thin NCG film (under a source-drain bias)

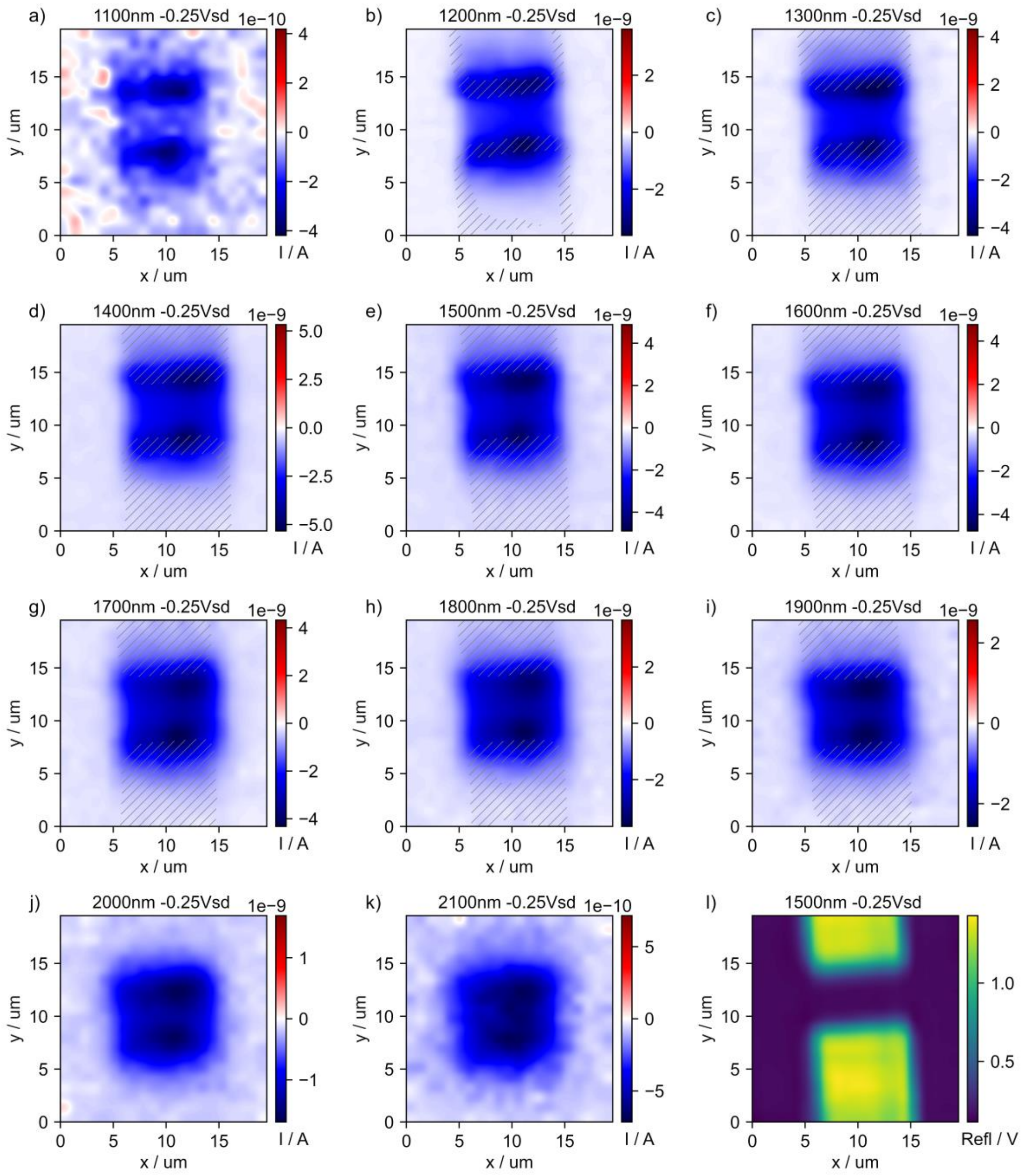

Figure A2.1: Scanning photocurrent imaging at -0.25 V source-drain bias. (a-k) Measurements taken between 1100 nm and 2100 nm wavelength with a device with 11 nm NCG layer thickness and 5 µm channel length. (l) Scanning reflectance images were recorded simultaneously, here shown at 1500 nm during the photocurrent scan. The reflectance data were superimposed on the photocurrent maps in (a-k) as grey shaded areas to indicate the position of the electrodes.

A2.2 Photoresponse of thin NCG film (short-circuit condition)

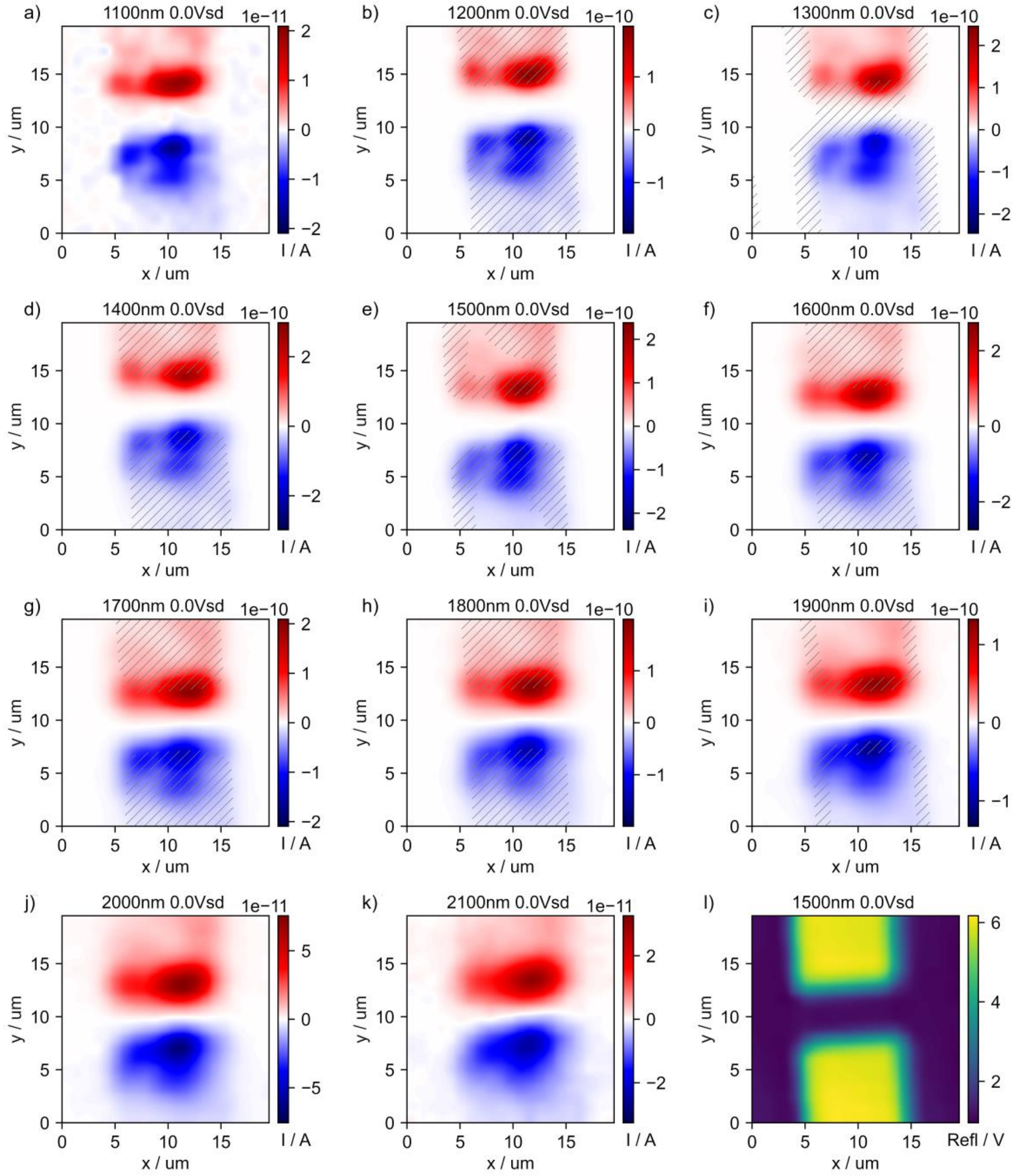

Figure A2.2: Scanning photocurrent imaging under short-circuit conditions. (a-k) Measurements taken between 1100 nm and 2100 nm wavelength with a device with 11 nm NCG layer thickness and 5 µm channel length. (l) Scanning reflectance images were recorded simultaneously, here shown at 1500 nm during the photocurrent scan. The reflectance data were superimposed onto the photocurrent maps in (a-k) as grey shaded areas to indicate the position of the electrodes.

A2.3 Spectroscopic analysis of thin NCG film)

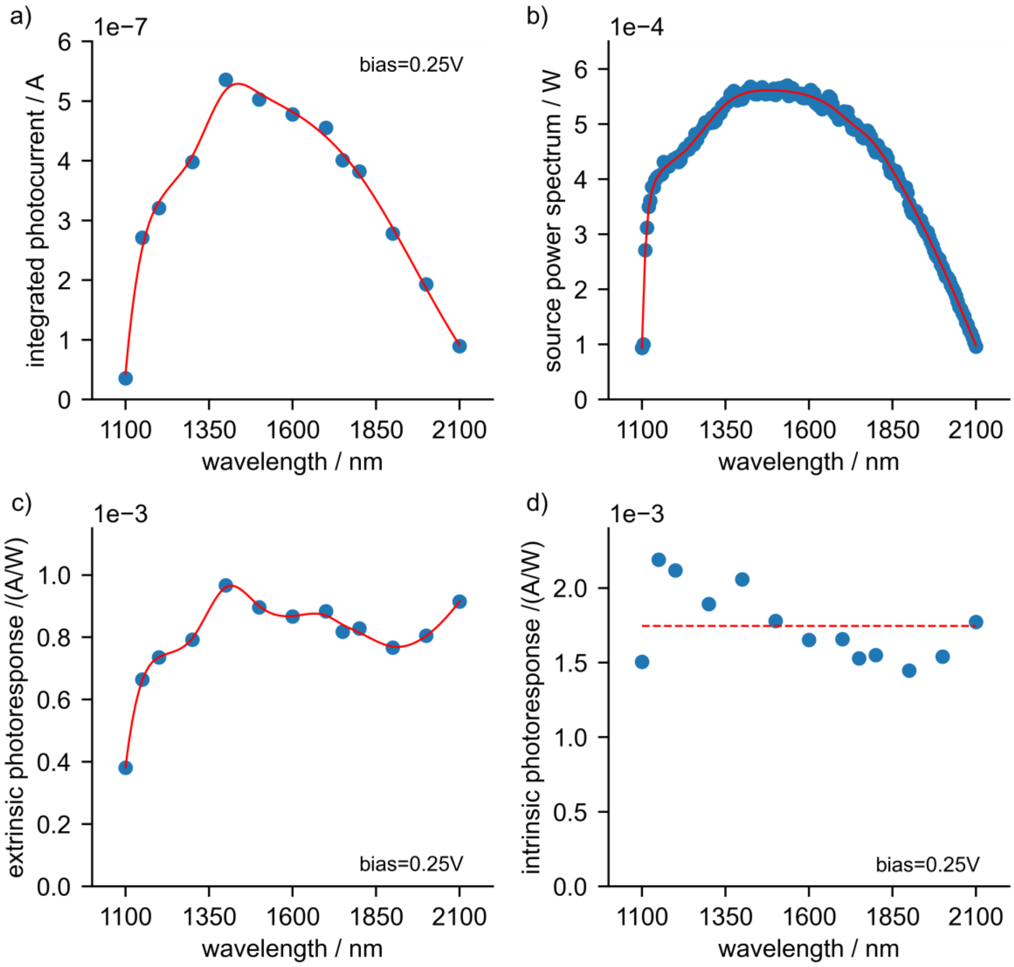

Figure A2.3: Spectroscopic analysis. (a) Integrated photocurrent obtained from the scanning photocurrent maps in Figure A2.1 of the 11 nm thick NCG device. (b) Calibrated power spectrum measured after wavelength-specific intensity adjustment of the supercontinuum light source by the AOTF. (c) Extrinsic photoresponse from the normalization of the integrated photocurrent with the power spectrum. (d) Intrinsic photoresponse from the normalization of the extrinsic photoresponse with the graphite absorptance.

A3 Simulation result from solving the continuity equation for the bolometric photocurrent

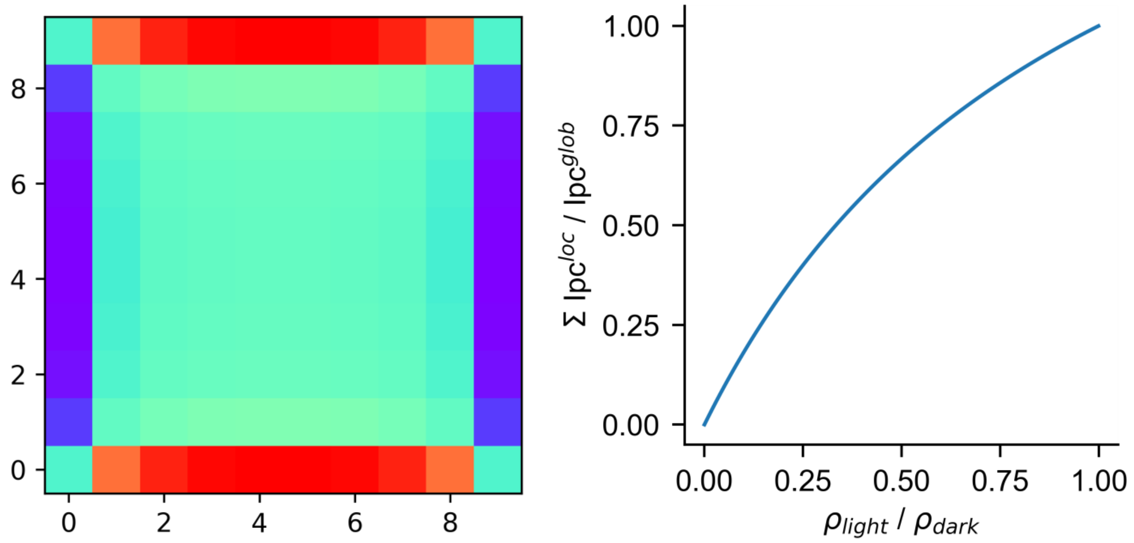

Figure A3: Simulation result from solving the stationary continuity equation of the bolometric photocurrent in 2 dimensions with a finite element method (FEM) solver shown here for a 10x10 lattice. The top/bottom and left/right boundaries fulfill Dirichlet and Neumann conditions, respectively. The observed enhancement and reduction of the photocurrent at the boundaries are similar to what has been observed by Darwish et al., Org. Electron. 2018, 62, 474–480. The graph to the right shows that summing up the photocurrents I_{PC}^{loc} calculated for raster scanning the illumination spot is equivalent to the photocurrent I_{PC}^{glob} for global illumination, if the difference between ρ_{light} and ρ_{dark}, the resistivity with and without illumination, respectively, is small.

A4 Raman spectroscopy of CNT networks

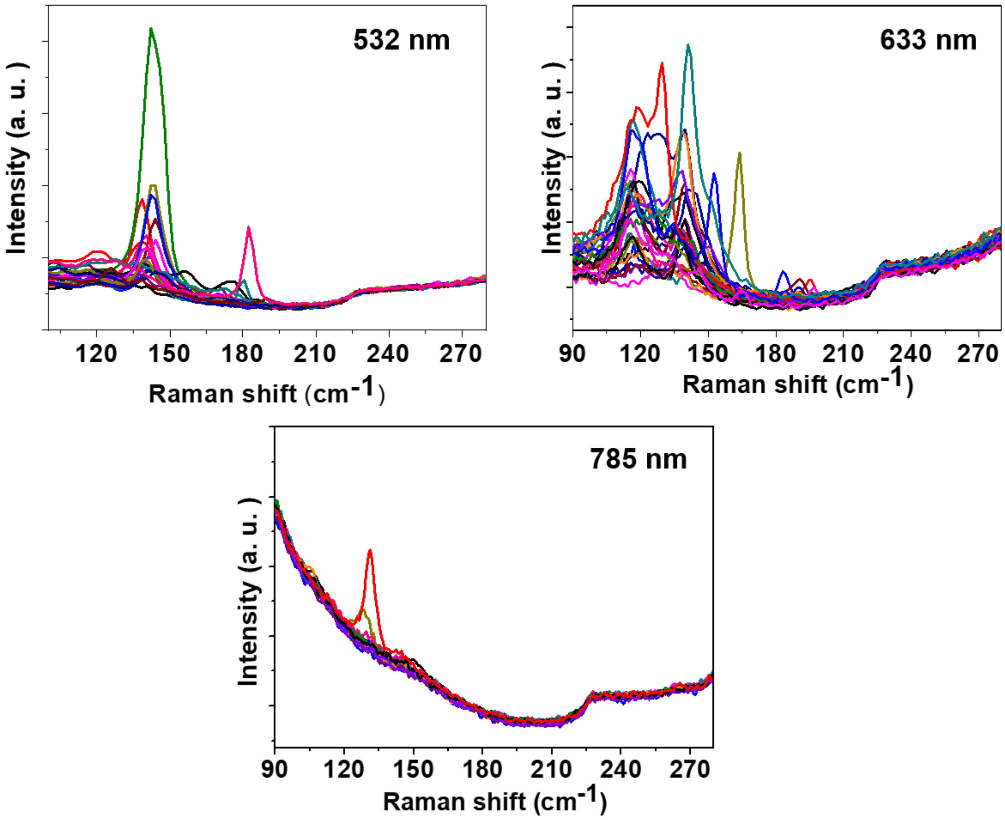

Figure A4: Multi-wavelength Raman spectra of the CNT networks. The measurements were performed by Dr. Feng Zhang in the group of Prof. Chang Liu at IMR, China.

A5 Scanning photocurrent maps of CNT device with 5 µm channel length

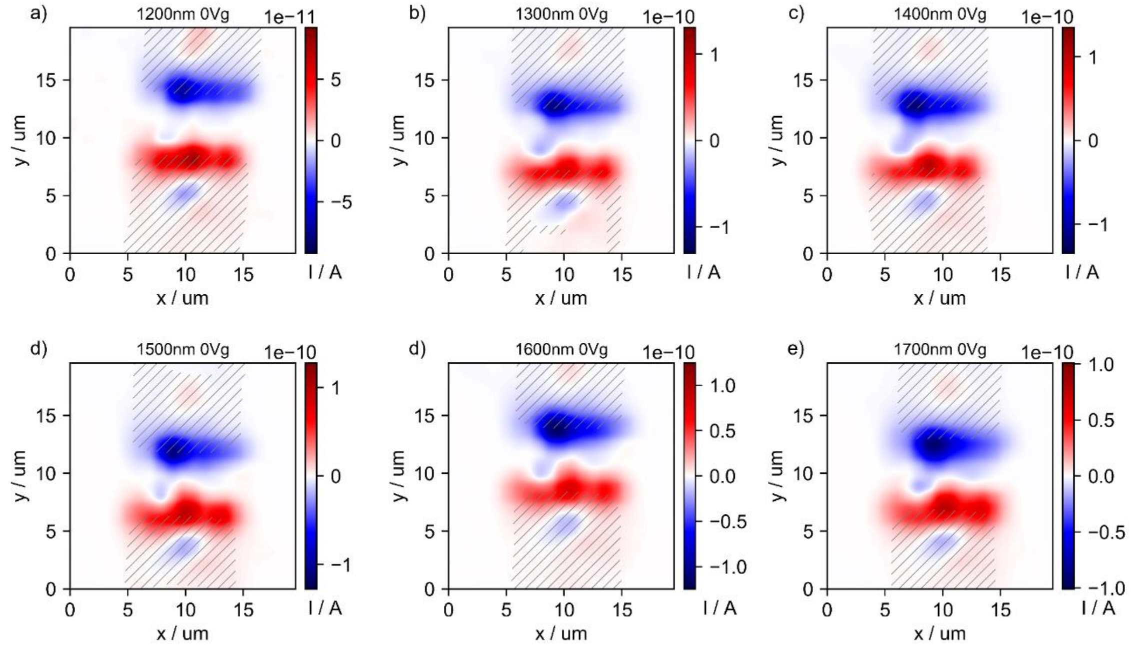

Figure A0.1: Scanning photocurrent imaging under short-circuit conditions. (a-e) Measurements taken between 1200 nm and 1700 nm wavelength with a device of 5 µm channel length. The reflectance data are superimposed onto the photocurrent maps in (a-e) as grey shaded areas to indicate the position of the electrodes.

A6 Near-field maps of PlasPhCs with different lattice parameters at laser, D, G and 2D excitation

a = 470 nm

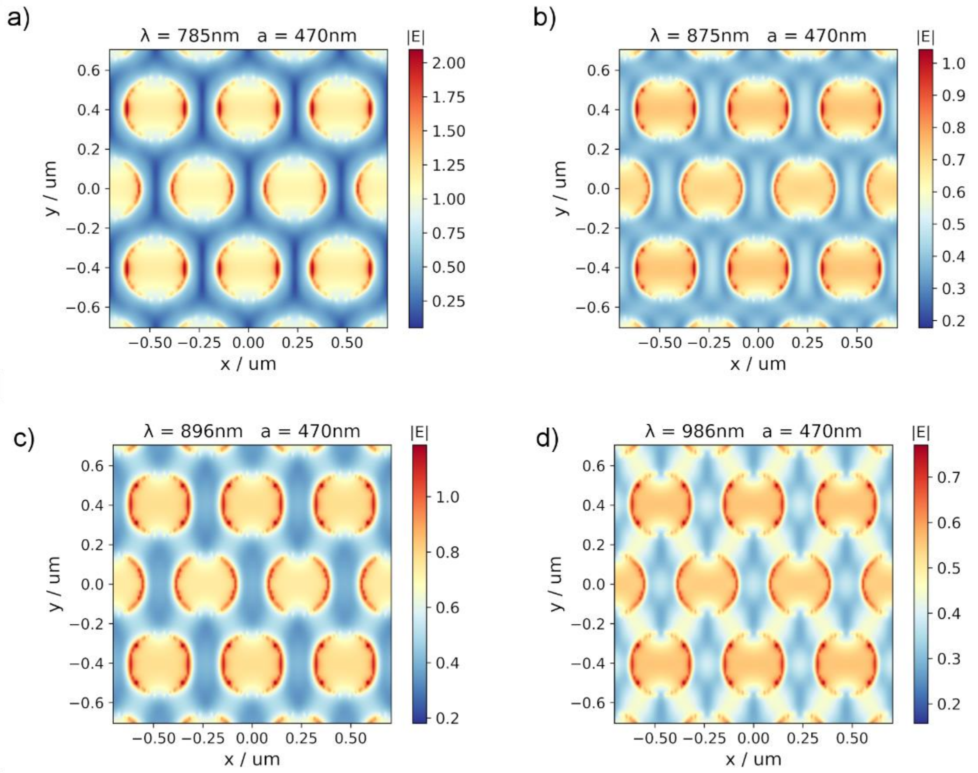

a = 500 nm

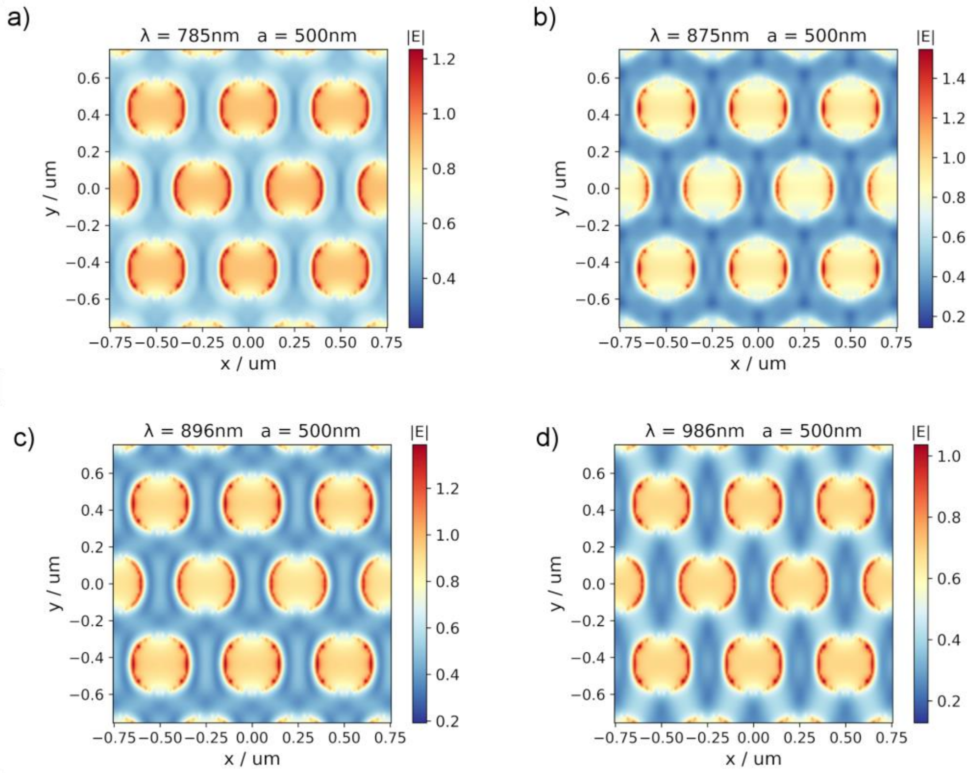

a = 560 nm

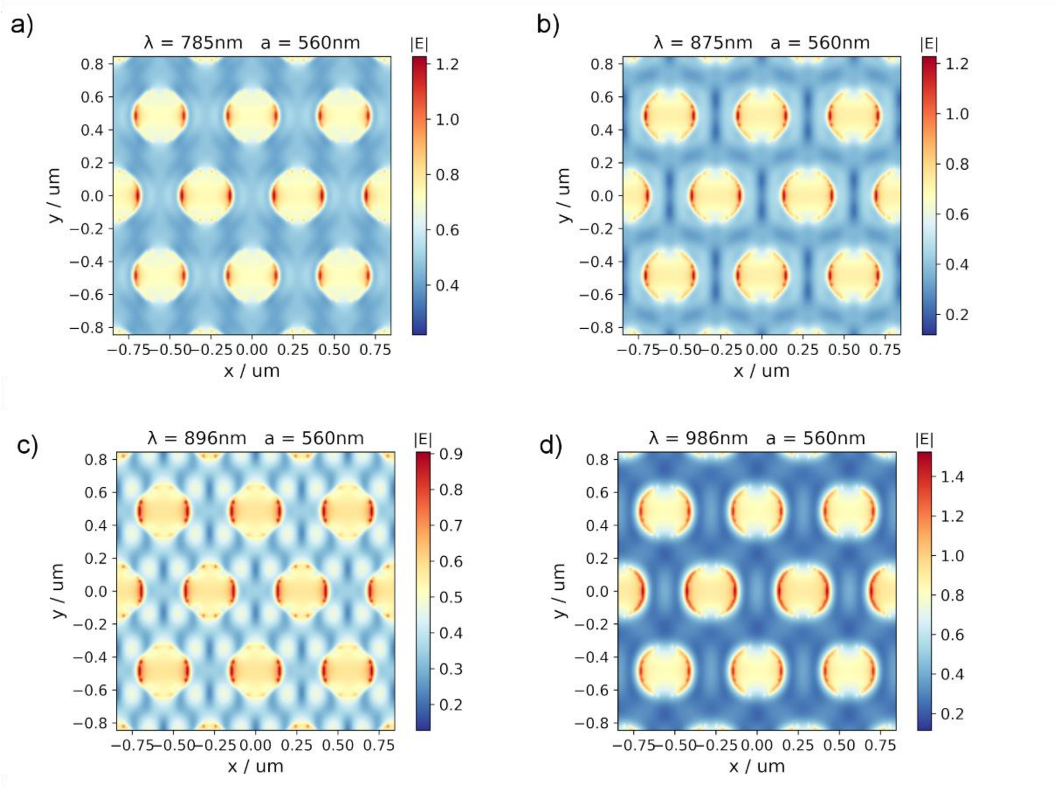

a = 590 nm

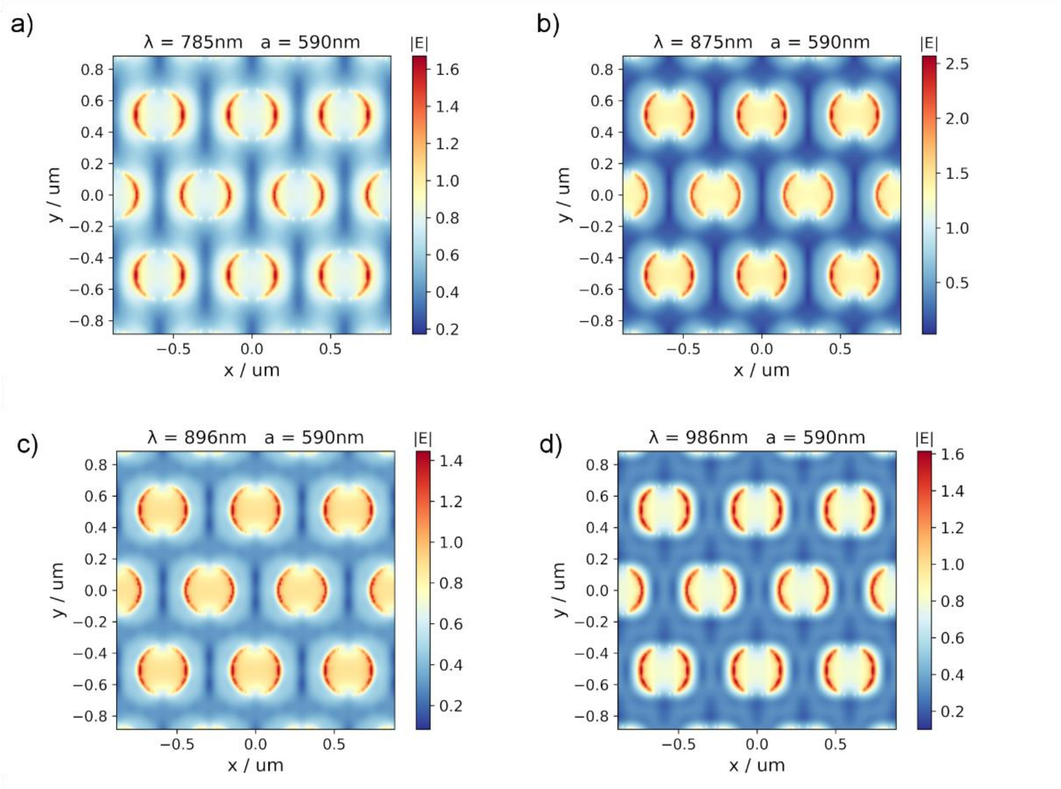

A7 Strategies for responsivity and detectivity improvement

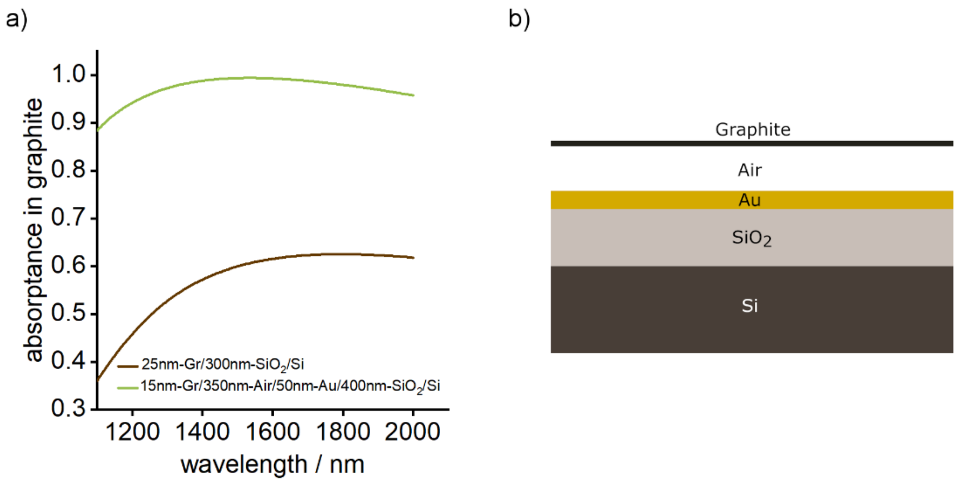

Figure A7: (a) calculated absorptance (in green) shown for the stack in (b).

Low light level detection

The strategies towards improving the detectivity are discussed in the following. The bolometric current density j expressed in terms of the temperature coefficient of resistance (α), resistivity (ρ) as described in eq. 4.1 (chapter 4) is given by,

$$j = -\frac{\alpha}{\rho} \cdot \Delta T \cdot E$$

ΔT is the light induced temperature change and can be expressed in terms of optical power P and channel area (length l x width w). Electric field E can be expressed in terms of voltage V and channel length. The bolometric current density j is related to the current I and the film thickness t,.

$$I = j \cdot w \cdot t$$

$$I = -\frac{\alpha}{\rho} \cdot \Delta T \cdot E \cdot w \cdot t$$

$$I = -\frac{\alpha}{\rho} \cdot \frac{P}{w \cdot l} \cdot \frac{V}{l} \cdot w \cdot t$$

Photoresponsivity R in terms of current (I) and incident power (P) can be expressed as,

$$R = \frac{I}{P} = -\frac{\alpha}{\rho} \cdot \frac{V}{l^2} \cdot t$$

$$A = l \cdot w$$

Dark current I_d in the device is given by,

$$I_d = \frac{V}{R_d} = \frac{V}{R_s \cdot \frac{l}{w}}$$

Now, making use of the above relations to express the detectivity D^* in terms of the device parameters and film properties.

$$D^* = R \cdot \sqrt{\frac{A}{2 \cdot q \cdot I_d}}$$

The sheet resistance is given by, $R_s = \frac{\rho}{t}$

$$D^* = -\frac{\alpha}{\rho} \cdot \frac{t}{l} \cdot \sqrt{\frac{R_s \cdot V}{2q}}$$

$$D^* = -\frac{\alpha \cdot t}{l} \sqrt{\frac{V}{2 \cdot q \cdot t \cdot \rho}}$$

List of Figures

Figure 1.1: Scientific publications from the year 2000 of different nanocarbon materials. The data was obtained by a keyword search using SCOPUS ---------- 3

Figure 2.1: (a) Real lattice representation of graphene with the lattice vectors a1 and a2 spanning the unit cell. The atoms from different sublattices are represented in different colors. (b) Reciprocal lattice notation with high symmetry points (Γ, K, and M). (c) Enlarged Brillouin zone near the K-point or the Dirac point. The full band structure is shown in Figure 2.2. ---------- 9

Figure 2.2:Full band structure of graphene. Adapted from [31] ---------- 10

Figure 2.3:(a) Measured transmittance of single layer graphene and the dashed red line represents the expected transmittance for the theoretical absorptance of πα. (b) Transmittance as a function of number of graphene layers. Adapted from reference [19] ---------- 11

Figure 2.4: (a) Calculated absorptance from the transfer matrix method as a function of layer number at three different wavelengths (532 nm, 785 nm and 1550 nm) and the plot in open circles represents the expected absorptance without taking reflectivity into account. (b) Reflectance R_N and transmittance T_N for 1550 nm as a function of layer number. Adapted from reference [32] ---------- 12

Figure 2.5: Dependence of sheet resistance as a function of grain size in polycrystalline graphene. The solid colored and open symbols correspond to the measured and the calculated values, and the solid line is according to the scaling law behavior described in the text. The parameters used in the scaling law are: $\boldsymbol{Rs0}$ = 300 Ohm/Sq. and $\boldsymbol{\rho gb = 0.3}$ kOhm µm. Reproduced from [38]. ---------- 14

Figure 2.6: Sheet of graphene with lattice vectors a_1 and a_2. The chiral vector and chiral angle for a nanotube are also indicated.---------- 15

Figure 2.7: Energy band scheme and density of states dependence for (a) (10, 10) metallic type (b) (20, 0) semiconducting type. The Fermi level E_F is located at zero energy. The sharp transition energies indicate the van Hove singularities. Reproduced from [46] ---------- 17

Figure 2.8: Single-particle and excitonic states. (a) Band structure of (19,0) semiconducting SWCNT for the single particle picture. (b) the corresponding density of states. (c) The simulated excitonic picture to describe the optical properties considering the many-body effects. Reproduced from [11]---------- 18

Figure 2.9: Multi-wavelength amorphization trajectory of carbon films for the variation of (a) I_D/I_G ratio and (b) G peak position. Adapted from reference [53] ---------- 20

Figure 2.10: Measured radial breathing mode frequency (ω_{RBM}) as a function of the nanotube diameter. Open circles represent the data and the solid line is the fit to the data. Fitting parameters shown in the equation 2.12. Reproduced from [59] --- 22

Figure 2.11: (a) Measured Raman spectrum (black bullets) at 644 nm laser line. The spectrum is fitted with individual Lorentizians (in color) and the global fit is shown in black solid line. (b) The dashed line on the Kataura plot indicates the laser excitation energy (1.925 eV) and the solid lines at (E_{laser} ± 0.06) eV indicate the resonance window. Reproduced from [59] -- 23

Figure 2.12: (a) Photothermoelectric (PTE) effect in single-layer graphene. Due to the regions with different chemical potentials (µ1 and µ2) there is a net PTE current. (b) Seebeck coefficient variation as a function of the chemical potential. (c) Graphene device with top and back gate configuration to result in a p-n junction in the channel. Region A is controlled by the back gate and the region B is controlled by both top and back gates. (d) Measured photovoltage as a function of different back and top gate voltages. (a), (b) and (c) adapted from [80]. (d) reproduced from [81]. ---------------------------- 30

Figure 2.13: (a) Back-gated graphene transistor device geometry for bolometric photodetection. (b) The conductivity decreases due to the light-induced heating in graphene. Adapted from [80]. -------------- 32

Figure 2.14: Experimentally measured photocurrent (in black) as function of $V_g - V_{Dirac}$. Red circles represent the modelled photovoltaic current Ipv contribution. Adapted and reproduced from [80,87]. --- 32

Figure 2.15: (a) suspended sc-SWCNT device (b) transconductance of the device (c) scanning photocurrent map of the device as a function of gate voltage (d) measured open-circuit voltage as a function of gate voltage at a position interior to the electrode away from the CNT-metal edge. Reproduced from [88] --- 34

Figure 2.16: Short-circuit photocurrent responsivity maps. (a) scanning photocurrent map with the laser polarization parallel to the nanotube axis. (b) resulting photocurrent map obtained after subtracting the perpendicular polarization map from the parallel polarization map. Reproduced from [88]. ------ 35

Figure 2.17: (a) SEM image of CNT network device with 2.5 µm channel length. (b) I-V characteristics of the devices with channel length 0.6 µm and 2.5 µm. Reproduced from [90]. ------------------------------------ 37

Figure 2.18: Scanning photovoltage profiles obtained with the laser being scanned across the length of the device for (a) Different thicknesses of the CNT film. (b) Different substrates. (c) Time-dependent behavior on different substrates. (d) Different contact metals. Reproduced from [91] ------------------- 38

Figure 2.19: Photoresponse of the aligned CNT film (a) Short-circuit photocurrent map with the strongest signal at the electrodes. Inset shows the cartoon of the device with the aligned tubes. (b) Open-circuit voltage (VOC) with different electrode metals. (c) measured open-circuit voltage at various NIR wavelengths as a function of laser power. (d) Polarization dependence of the photocurrent. Reproduced from [92] ---------- 39

Figure 2.20: Photocurrent maps under a source-drain bias of 1 V at 1064 nm (a) Square shaped device. (b) Photocurrent profile obtained from the line-cut in (a) at different bias voltages. (c) Photocurrent from a triangular shaped device. (d) Photocurrent profile obtained from the line-cut in (d) Reproduced from [37] ---------- 40

Figure 3.1: Process flow of NCG synthesis and device fabrication ---------- 43

Figure 3.2: Raman microscopy setup (Renishaw inVia) ---------- 44

Figure 3.3: Photocurrent setup components that include supercontinuum light source, acousto-optic tunable filter, beamsplitters. AOTF photograph by P. B. Selvasundaram. ---------- 48

Figure 3.4: Schematic of the photocurrent measurement setup ---------- 50

Figure 3.5: Photocurrent measurement setup ---------- 50

Figure 3.6: Output spectrum from AOTF when tuned to 640 nm (from SuperK SELECT manual, NKT) ------ 54

Figure 3.7: Output spectrum from AOTF when tuned to 640 nm (adapted from SuperK SELECT manual, NKT) (b) Visible (c) NIR1 (d) NIR2. Measurement data in (b), (c) and (d) are factory-calibrated. ------- 54

Figure 3.8: Converting the supercontinuum (SC) spectrum to a smooth power spectrum by a wavelength-specific intensity adjustment to the acousto-optic tunable filter (AOTF). (a) The raw SC spectrum is shown in black and targeted smooth spectrum is shown in red. (b) Obtained smooth spectrum after the intensity adjustment. ---------- 56

Figure 3.9: Optical beam path of the NIR beam after exiting the reflective collimator and into the microscope objective through the 90:10 beam splitter. ---------- 57

Figure 3.10: Measured axial chromatic shift of the 100x NIR objective. The data points in the open circles indicated are the extrapolated values. ---------- 58

Figure 4.1: Transfer matrix simulation of (a) the local absorption and (b) Poynting vector in a 25nm graphite/300nm-SiO2/Si multilayer. The z-axis points along the surface normal into the substrate; the origin is at the graphite-air interface. (c-f) Calculated total absorptance in the graphite layer for different graphite and SiO_2 layer thicknesses. Simulated with s-polarized light under normal incidence. ---------- 67

Figure 4.2: (a) and (c) AFM images of the 11 nm and 24 nm NCG films and their respective line-cuts in (b) and (d). ---------- 69

Figure 4.3: (a) Raman spectra of NCG/300 nm-SiO2/Si with 11 and 24 nm NCG thicknesses. (b) NCG Raman spectra fitted to Gaussian peaks for obtaining the D- and G- line widths. Shown is the overall fit. (c) Raman G-peak position and intensity ratio of D-peak and G-peak for NCG compared with data from Ferrari et al.[50] for graphite, nanocrystalline (nc) graphite, and two forms of DLC. The sp-hybridization is indicated. (d) Crystallite size La in NCG determined from the FWHM of the D- and G-peaks. The dashed lines are extrapolated correlations based on Cancado et al.[56,57] ---------- 70

Figure 4.4: Device overview. (top) on the left is the zoom-in optical micrograph of NCG devices on SiO2/Si substrate with different channel lengths. Scale bar equals 10 µm. Inset shows a cross-sectional view with Pd source (S) and drain (D) electrodes. Structure overview with electrode leads and pads is shown on the right. (bottom) Representative SEM image of a 5 µm channel length device. Scale bar equals 2 µm. ---------- 71

Figure 4.5: I-V curve of the 5 µm channel length device of 24 nm thick film (b) Device resistance vs channel length for the 11 and 24 nm NCG film thicknesses. ---------- 72

Figure 4.6: Sheet resistance RS of NCG as a function of temperature (77K-400K). Inset shows the resistivity as a function of temperature. The linear temperature coefficient α has been calculated as α = $R_S^{-1} \cdot dR_S/dT$. ---------- 73

Figure 4.7: Scanning photocurrent imaging at -0.25 V source-drain bias. (a-k) Measurements taken between 1100 nm and 2100 nm wavelength with a device with 24 nm NCG layer thickness and 5 µm channel length. (l) Scanning reflectance images were recorded simultaneously, here shown at 1500 nm during the photocurrent scan. The reflectance data were superimposed on the photocurrent maps in (a-k) as grey shaded areas to indicate the position of the electrodes. ---------- 74

Figure 4.8: Simulated absorptance in Pd (a) and reflectance from the Pd/Gr/SiO2/Si multilayer (b). ------- 76

Figure 4.9: Scanning photocurrent imaging under short-circuit conditions. (a-k) Measurements taken between 1100 nm and 2100 nm wavelength with a device with 24 nm NCG layer thickness and 5 µm channel length. (l) Scanning reflectance images were recorded simultaneously, here shown at 1500 nm during the photocurrent scan. The reflectance data were superimposed onto the photocurrent maps in (a-k) as grey shaded areas to indicate the position of the electrodes. ---------- 77

Figure 4.10: Spectroscopic analysis. (a) Integrated photocurrent obtained from the scanning photocurrent maps in Figure 3 of the 24 nm thick NCG device. (b) Calibrated power spectrum measured after wavelength-specific intensity adjustment of the supercontinuum light source by the AOTF. (c) Extrinsic photoresponse from the normalization of the integrated photocurrent with the power spectrum. (d) Intrinsic photoresponse from the normalization of the extrinsic photoresponse with the graphite absorptance. -- 78

Figure 4.11: (a) Local absorption, (b) Poynting vector, and (c) resulting absorptance in the graphite layer versus the graphite layer thickness at 1550 nm wavelength. (d) Bolometric photocurrent (I_{photo}) and dark current (I_{dark}) measured for 11nm-NCG and 24nm-NCG devices (dots) with extrapolations based on simulation data from (c) and the measured resistivities. -- 81

Figure 5.1: Fabrication and characterization of CNT devices. (a) SEM micrograph of CNT film on SiO_2/Si substrate. Scale bar equals 2 µm. (b) Optical micrograph of CNT devices on 300nm-SiO_2/Si substrates with different channel lengths. Scale bar equals 10 µm. Inset shows a cross-sectional view with the Pd source (S) and drain (D) electrodes. (c), (d) Raman spectra of CNT/300nm-SiO_2/Si. ----------------- 86

Figure 5.2: The calculated optical resonances $\Delta E = E_{ii}$ for SWCNTs in the 100 – 220 cm^{-1} frequency range. The E_{ii} versus ω_{RBM} (Kataura plot) was calculated using the equations presented in the work of Araujo et al.[134] The solid lines in color indicate the E_{laser} used in the Raman measurements and the narrow color strips correspond to the respective width of the resonance region ($E_{laser} \pm 0.06$) eV. The grey shaded region represents the laser excitation energies in the photocurrent experiment. The vertical dashed lines correspond to the measured radial breathing mode frequency region of the SWCNT network. --- 87

Figure 5.3: RBM data from Araujo et al. shown in open circles.[154] The RBM frequency range (105 - 200 cm^{-1}) of the SWCNT film (from Figure 5.2) is mapped here as the dashed horizontal lines, and the corresponding vertical lines indicate the diameter range in the film. -- 88

Figure 5.4: Electrical characterization of the SWCNT devices. (a)-(c) Transfer characteristics. (d) current - voltage (I_{sd}-V_{sd}) characteristics with no applied gate voltage. --- 90

Figure 5.5: Scanning photocurrent imaging under short-circuit conditions. (a-k) Measurements taken between 1200 nm and 1800 nm wavelength with a device of 10 µm channel length. (l) Scanning reflectance images were recorded simultaneously, here shown at 1550 nm during the photocurrent scan. The electrode with current amplifier and grounded electrode are indicated. The reflectance data are superimposed onto the photocurrent maps in (a-k) as grey shaded areas to indicate the position of the electrodes.-- 92

Figure 5.6: Scanning photocurrent and photovoltage imaging under short-circuit conditions at 1500 nm of the 10 µm device. (a-b) Photocurrent maps in linear and log scale, respectively. (c) Phase of the photocurrent signal. (d-e) Scanning photovoltage image in linear and log scale. (f) Phase of the photovoltage signal.-- 94

Figure 5.7: Spectroscopic analysis of the 10 µm device in short-circuit conditions. (a) Integrated photocurrent obtained from the scanning PC maps in Figure 5.5. The absolute quantity of the positive and negative real photocurrents is shown. (b) Calibrated source spectrum. (c,d) Extrinsic photocurrent obtained after the normalization of the integrated photocurrent with the source spectrum in (b).-- 96

Figure 5.8: Scanning photocurrent imaging under a source-drain bias at 1300 nm and 1500 nm with a device of 10 µm channel length. The reflectance data were superimposed onto the photocurrent maps as grey shaded areas to indicate the position of the electrodes. (a-c) at 1300 nm with V_{sd} = -0.3V, 0V and 0.3V. (d-f) at 1500 nm with V_{sd} = -0.3V, 0V and 0.3V. --- 97

Figure 5.9: (a) Gate voltage dependent line scans of the short-circuit photocurrent (I_{sc}) in the device On state (V_g = -1.5 V) and Off state (V_g = 0 V). Dashed vertical lines indicate the electrode edges. The device scheme is shown in the inset of (b) with the device center at x = 0. (b) Gate voltage map: I_{sc} as a function of the gate voltage along the device x-axis. (c) In red shows the open-circuit voltage (V_{OC}) as a fuction of gate voltage measured at x = 1.8 µm. Open circles in blue represent the Seebeck coefficient from sc-SWCNT measured by Small et al.[89] Reproduced from[88] --------------------------------- 98

Figure 5.10: Scanning photovoltage imaging under different gate polarities at 1500 nm with a device of 10 µm channel length. (a,b) photovoltage maps under gate voltage -6 V shown in the linear and symlog scale. (c) corresponding phase map at -6 V. (d,e) photovoltage maps under gate voltage 7 V shown in the linear and symlog scale. (f) corresponding phase map at 7 V.--------------------------------100

Figure 5.11: Scanning photocurrent imaging under different gate polarities at 1500 nm with a device of 10 µm channel length. (a,b) photocurrent maps under gate voltage -6 V shown in the linear and symlog scale. (c) corresponding phase map at -6 V. (d,e) photocurrent maps under gate voltage 7 V shown in the linear and symlog scale. (f) corresponding phase map at 7 V.--------------------------------101

Figure 5.12: Schematic side view of CNT device indicating the oxide and quantum capacitance ------------102

Figure 5.13: Band bending in p-type silicon substrate (a) without illumination (b) under illumination ----103

Figure 6.1: (a) Side view scheme of silicon-on-insulator (SOI) stack with 250 nm-Si/3000 nm-SiO_2/p-Si SOI. (b) Side view scheme of the PPhC structure obtained by etching air-holes into the top silicon layer of the SOI stack followed by gold layer deposition. (c) Optical micrograph of the fabricated PPhC field.

(d) SEM micrograph (top view) of the PPhC structure. The lattice distance is represented as a, and the air-hole diameter is represented as d. ---108

Figure 6.2: (a) Calculated reflectance under normal incidence of the (SOI) stack with 250 nm-Si/3 µm-SiO_2/p-Si. (b) Calculated reflectance under normal incidence of the plasmonic-photonic structure (Figure 6.1b) with air-hole diameter 310 nm and lattice distance 560 nm. (c) Side view scheme showing one air-hole and the corresponding side view near field maps showing the regions of E-field enhancement at 785 nm, 1525 nm, and 1690 nm. The dashed red lines indicate the top and the bottom surface in the PPhC structure. ---110

Figure 6.3: (a) Raman spectrum of graphene on a PPhC with a = 590 nm, and d = 310 nm. (#) indicates the signal at different sites on the PPhC. (b) SEM image of the PPhC structure from the Figure 6.1d. (c) Raman spectrum of graphene on suspended graphene over a 2.5 µm wide trench. (d) Side-view scheme of the trench. (e) Raman spectrum of graphene on supported graphene Au-SOI stack. (f) Schematic of the planar stack.---112

Figure 6.4: (a) Fill-factor (FF) normalized peak intensities of the D, G and 2D peaks as a function of lattice parameter for 532 nm laser excitation. The dashed lines indicate the corresponding peak intensities for the case of suspended graphene (Figure 6.3d). (b) Enhancement factor obtained after normalizing the FF-normalized peak intensities with that of the suspended graphene. (c), (d) for 785 nm excitation. ---113

Figure 6.5: (a)-(e) Simulated reflectance spectrum of PPhCs under normal incidence for different lattice parameters. The solid vertical dashed lines indicate the 532 nm and 758 nm laser excitation and the dashed lines indicate the respective D, G and 2D Raman scattered light (see Table 6.1) ---------------115

Figure 6.6: The near-field maps showing the electric-field distribution (E-field amplitude normalized w.r.t the incident E-field amplitude) at the top of the plasmonic-photonic structure in the x-y plane (See also Figure 6.3b for the corresponding top view SEM image) for the structure with the 530 nm lattice parameter and the air-hole diameter of 310 nm. The near-field maps under normal incidence in xz plane with p-polarization and incident electric field amplitude of 0.5 are shown for (a) laser excitation wavelength of 785 nm (b) at the D peak near 875 nm (c) at the G peak near 896 nm (d) at the 2D peak near 986 nm. (e) Reflectance of the plasmonic-photonic structure under normal incidence. The dashed lines indicate the laser excitation, D peak, G peak and the 2D peak, respectively. ---116

Figure 6.7: Averaged electric field intensity at the top of the plasmonic-photonic surface for 785 nm laser excitation obtained by integrating the local electric field amplitude in the near-field maps in Figure 6.6. The electric field is integrated over the entire area including the region between the air-holes.

The normalized electric-field intensity as a function of lattice parameter is plotted for the laser excitation, and the product of laser excitation and (D, G, and 2D) peaks (see the text).----------------117

List of Tables

Table 2.1: Linear fit parameters obtained from the experimental FWHM of G and D peaks.[52] 21

Table 3.1: Device fabrication parameters of NCG and CNT films. 46

Table 3.2: Broadband optical fiber characteristics. 52

Table 3.3: Calculated data for the axial chromatic shift of the 100x NIR objective used. The data from 1200 nm to 1800 nm with the reference wavelength as 587.5 nm was provided by Mitutoyo corp. The extrapolated values are indicated in bold. 58

Table 3.4: Frequency bandwidth and waiting time for different filter slopes (from SRS830 manual) 60

Table 4.1: Spin coating conditions and the resulting NCG thickness. 68

Table 4.2: Compilation of photodetector key performance figures. 82

Table 5.1: Predicted optical transitions of s-SWCNTs and m-SWCNTs in the CNT network. 89

Table 6.1: Plasmonic-photonic structure fabrication parameters. 109

Table 6.2: Stokes wavelengths corresponding to the Raman scattered light in graphene. 112

In the memory of my late grand father

Acknowledgements

The research work presented in this thesis has been carried out at the Institute of Nanotechnology at the Karlsruhe Institute of Technology, Germany and Department of Materials and Geosciences at Technische Universität Darmstadt, Germany.

First and foremost, I would like to express my sincere thanks to Prof. Stark, Prof. Hoffmann, Prof. Schneider, and Prof. Krupke for agreeing to be part of the examination committee and reviewing my thesis.

I owe my deep sense of gratitude to my advisor Prof. Ralph Krupke. Under his supervision over the past five years, I have had the privilege to develop my experimental skills and mature as a researcher. He has been an outstanding teacher in and outside the lab, and was incredibly generous with his time. I have always found his wise counsel on many things, scientific or otherwise, to be very thoughtful. He has always been genuinely interested in all of his students' well-being, and I am very grateful for that.

I extend my sincere thanks to the collaborators. The graphene transfer was done in the group of Prof. Kalbac, and the nanotube networks were synthesized in the group of Prof. Chang Liu. and Dr. Feng Zhang. Thanks to Dr. Aimi Abass and Juan Ramon for the support in the simulations.

Special thanks to Simone Dehm for all the technical help and support right from my internship period. She has been very patient in teaching me lithography and all the other device fabrication techniques.

I owe a big thanks to my former colleagues Pranauv Balaji, Adnan Riaz, and Feliks Pyatkov for their initial guidance and support in getting me started at the lab. Cheers to comrade Sandeep Kumar and my officemate Min-Ken Li and Devang Parmar who have kept me in high spirits all these years. In them, I have always had a reliable company. The banter and arguments over a coffee are something I will cherish.

Many thanks to colleagues and friends, especially Naveed Hussain, Nithin Suryadevara, Surya Abhishek, Praneeth Chilakalapudi, Mridula Prathapan, Behdad Sadeghian, Anna-Lena Eick, and Yukari Yamasaki, who made my stay and experience in Karlsruhe memorable.

Upon reflection, I am extremely thankful to my former mentors, Dr. Ponsinet and Dr. Barois, who have always been very kind to me. Through their support and motivation, I developed an interest in optics and photonics in the first place.

Lastly, I am thankful to my family, especially my mother, grandmother, and brother, who have been incredibly supportive right from the word go—special mention to the *Vadrevu* family for their steadfast support throughout. Finally, I am indebted to my wife, Sahana Sheshachala, for being there for me always, and I am immensely grateful for her support and unceasing forbearance at all times.

List of Publications

1. **N. A. Peyyety**, S. Kumar, M.-K. Li, S. Dehm, R. Krupke, *ACS Applied Materials & Interfaces* **2022**, *14*, 9525-9534.
2. M. Gaulke, A. Janissek, **N. A. Peyyety**, I. Alamgir, A. Riaz, S. Dehm, H. Li, U. Lemmer, B. S. Flavel, M. M. Kappes, F. Hennrich, L. Wei, Y. Chen, F. Pyatkov, R. Krupke, *ACS nano* **2020**, *14*, 2709-2717.
3. H. Li, G. Gordeev, O. Garrity, **N. A. Peyyety**, P. B. Selvasundaram, S. Dehm, R. Krupke, S. Cambré, W. Wenseleers, S. Reich, M. Zheng, J. A. Fagan, B. S. Flavel, *ACS nano* **2019**, 14, 948-963.